

Generic Radar Processing Methods for Monitoring Tasks on Bridge Infrastructure

Chris Eric Michel

Doctoral Thesis
Karlsruhe, 2023

Generic Radar Processing Methods for Monitoring Tasks on Bridge Infrastructure

Zur Erlangung des akademischen Grades eines

DOKTOR-INGENIEURS (Dr.-Ing.)

von der KIT-Fakultät für
Bauingenieur-, Geo- und Umweltwissenschaften
des Karlsruher Instituts für Technologie (KIT)

genehmigte

DISSERTATION

von

Chris Eric Michel

aus Korbach

Tag der mündlichen Prüfung: 16.02.2023

Referent: Prof. Dr.-Ing. Stefan Hinz
Institut für Photogrammetrie und Fernerkundung
Karlsruher Institut für Technologie

Korreferent: Prof. Dr.-Ing. Andreas Eichhorn
Institut für Geodäsie
Technische Universität Darmstadt

Karlsruhe (2023)

Chris Eric Michel

Generic Radar Processing Methods for Monitoring Tasks on Bridge Infrastructure

Doctoral Thesis

Date of examination: 16.02.2023

Referees:

Prof. Dr.-Ing. Stefan Hinz

Prof. Dr.-Ing. Andreas Eichhorn

Karlsruhe Institute of Technology

Department of Civil Engineering, Geo and Environmental Sciences

Institute of Photogrammetry and Remote Sensing

Kaiserstr. 12

76131 Karlsruhe



This document is licensed under a Creative Commons Attribution-ShareAlike 4.0 International License (CC BY-SA 4.0):

<https://creativecommons.org/licenses/by-sa/4.0/deed.en>

Abstract

Critical transport infrastructure, such as bridges, can only be operated safely if its condition is regularly assessed. In addition to visual inspections, the assessment includes measurements of the bridge's response to static or dynamic loads. These measurements are usually performed with a wide variety of directly contacting sensors. However, remote sensors, such as ground-based interferometric radar (GBR), are also increasingly applied. GBR can remotely measure displacements with precision in the sub-millimetre range by emitting an electromagnetic wave, which is reflected by features at the bridge underside.

Compared to contacting sensors, setup time is reduced and normal operation of the bridge is undisturbed. However, comparable measurement uncertainties are achieved only by addressing several challenges during the processing of the measurements. These challenges involve mainly the removal of external influences, such as signal disturbances or changes in the atmospheric properties. Measurements are further influenced by static clutter and projection errors, which result in systematic deviations. Static clutter is determined with an adapted circle estimation, while projection errors are addressed by applying multiple sensors to estimate separate displacement components. With these additional processing steps, GBR achieves a similar uncertainty as other remote sensors, which is validated by comparisons to reference sensors. Uncertainties in clutter estimation and limited range resolution can explain the remaining differences to these references.

The resulting displacement measurements are then used to estimate damage-sensitive features like natural frequencies and mode shapes. Frequencies are estimated by fitting a model of a damped sinusoid to the vibration after a vehicle crossing. With this approach, each vehicle crossing is evaluated separately, enabling a distinction between different classes of vehicle mass. Additionally, the large number of frequency estimations enables a more reliable determination of the temperature influence on natural frequencies. For the determination of mode shapes, an alternative measurement setup is proposed. This setup utilises the flat underside of a bridge to reflect the emitted signal towards a reflector on the ground opposite of the GBR. A permanent installation of reflectors is not required, which extends the application of GBR to a large number of bridges. In addition, the measurement cannot be influenced by other displacement components, which reduces

the occurrence of systematic deviations. Consequently, mode shapes are more sensitive to damage since the uncertainties are reduced. The underlying principle is again validated by comparisons with reference sensors.

Zusammenfassung

Kritische Verkehrsinfrastrukturen, wie z. B. Brücken, können nur dann sicher betrieben werden, wenn ihr Zustand regelmäßig bewertet wird. Neben visuellen Inspektionen umfasst die Bewertung auch Messungen des Brückenverhaltens auf statische oder dynamische Lasten. Diese Messungen werden in der Regel mit einer Vielzahl von Sensoren durchgeführt, die direkt an der Brücke befestigt sind. Zunehmend werden jedoch auch Fernerkundungssensoren eingesetzt, wie z.B. das bodenbasierte interferometrische Radar (engl.: ground-based interferometric radar - GBR). GBR können aus der Ferne Verschiebungen mit einer Genauigkeit im Submillimeterbereich messen, indem sie eine elektromagnetische Welle aussenden, die von Strukturen an der Unterseite der Brücke reflektiert wird.

Im Vergleich zu direkt befestigten Sensoren wird die Installationszeit verkürzt und der normale Betrieb der Brücke wird nicht beeinträchtigt. Vergleichbare Messunsicherheiten lassen sich jedoch nur erreichen, wenn bei der Prozessierung der Messungen bestimmte Herausforderungen berücksichtigt werden. Dabei geht es vor allem um die Entfernung externer Einflüsse wie Störungen des Signals oder Veränderungen atmosphärischer Parameter. Die Messungen werden außerdem durch statischen Clutter und Projektionsfehler beeinflusst, die zu systematischen Abweichungen führen. Statischer Clutter wird mit einer angepassten Kreisschätzung bestimmt, während Projektionsfehler durch die Verwendung mehrerer Sensoren zur Schätzung separater Verschiebungskomponenten vermindert werden. Mit diesen zusätzlichen Prozessierungsschritten erreicht GBR eine ähnliche Unsicherheit wie andere Fernerkundungssensoren, was durch Vergleiche mit Referenzsensoren validiert wird. Verbleibende Unterschiede zu diesen Referenzsensoren lassen sich durch Unsicherheiten bei der Schätzung von Clutter und durch die begrenzte Auflösung einzelner Reflexionen erklären.

Die resultierenden Verschiebungsmessungen werden dann zur Schätzung schadensempfindlicher Merkmale wie Eigenfrequenzen und Eigenformen verwendet. Eigenfrequenzen werden bestimmt, indem ein Modell einer gedämpften Sinuskurve für die Schwingung nach einer Fahrzeugüberfahrt geschätzt wird. Mit diesem Ansatz wird jede Fahrzeugüberfahrt separat analysiert, was eine Unterscheidung zwischen verschiedenen Fahrzeugmassen ermöglicht. Außerdem erlaubt die große Anzahl von Frequenzschätzungen eine zuverlässigere Bestimmung des Temperatureinflusses auf die Eigenfrequenzen. Für

die Bestimmung der Eigenformen wird ein alternativer Messaufbau erarbeitet. Dieser Aufbau nutzt die flache Unterseite einer Brücke, um das ausgesendete Signal auf einen Reflektor auf dem Boden zu spiegeln. Eine permanente Installation von Reflektoren an der Brückenunterseite ist daher nicht erforderlich, wodurch die Anwendung von GBR auf eine große Anzahl von Brücken erweitert wird. Darüber hinaus kann die Messung nicht durch andere Verschiebungskomponenten beeinflusst werden, was das Auftreten von systematischen Abweichungen verringert. Folglich sind die Eigenformen empfindlicher gegenüber Schäden, da die Unsicherheiten reduziert werden. Das zugrunde liegende Prinzip dieses alternativen Messaufbaus wird wiederum durch Vergleiche mit Referenzsensoren validiert.

Contents

1	Introduction	1
1.1	Main Objective and Research Goals	2
1.2	Thesis Outline and Contributions	3
2	Fundamentals of Ground-Based Interferometric Radar	7
2.1	Working Principle	7
2.2	Existing Research on GBR	13
2.3	Overview of Investigated Bridges	20
3	Processing of Displacement Measurements from Ground-Based Radar	25
3.1	Methodology	28
3.2	Results	38
3.3	Discussion	54
3.4	Conclusion	57
4	Estimating Natural Frequencies for Damage Detection	59
4.1	Natural Frequencies as Damage Sensitive Features	59
4.2	Least Squares for Estimation of a Damped Sinusoid	61
4.3	Results	66
4.4	Discussion	76
4.5	Conclusion	78
5	Indirect Displacement Measurements for Mode Shape Estimation	81
5.1	Methodology	82
5.2	Displacement Measurement and Validation With Reference Sensors	84
5.3	Determination of Mode Shapes	88
5.4	Conclusion	93
6	Conclusion and Outlook	95
	Bibliography	99
	List of Figures	107
	List of Tables	109
	List of Symbols	111
	List of Abbreviations	113

Introduction

The transport infrastructure ensures the mobility of goods and people through its extensive road and rail network and constitutes an important economic and societal element of every country. However, one of the most critical elements of this infrastructure has seen increasing utilisation through growing traffic loads at the same time as its average age is rising. There are approximately 40 000 bridges in the German road network and about 25 000 in the rail network [12, 63]. Most of the road bridges were constructed in the period between 1960 and 1985, whereas the average age of rail bridges is 72 years [63]. With the growing traffic load, a degradation of the structures is expected, requiring increased maintenance and new construction work. Detecting and assessing this degradation is an important task to ensure safe and reliable operation. The assessment mainly consists of a regularly scheduled visual inspection of the structures as, for example, regulated in the standards DIN 1076 [22] for German road bridges and 804.800x [83] for German rail bridges. Cracks, rust, or other degradation are detected and monitored throughout the bridges' service life. However, damages on the inside of the structure or at places difficult to access can be detected too late or even completely missed. To aid the visual inspection, bridges can also be assessed through experimental methods or through simulations. Experimental methods use sensors to determine properties that are relevant to a bridge's condition, whereas simulations use assumptions about these properties and the applied load. The models of these simulations are commonly calibrated by sensor measurements.

Sensors measure the bridge's response to static or dynamic loads. In the case of static tests, the load is known, whereas dynamic tests can be performed with both known and unknown loads. Unknown loads are, for example, ambient excitation through vehicles from normal bridge operation or through wind. Operational modal analysis (OMA) estimates features from these response measurements, allowing an assessment of the bridge's condition over time since feature changes can be correlated with damages. Most sensors require direct contact with the structure, although remote sensing technology has also been increasingly applied in recent years. Remote measurement of the bridge's response is advantageous in certain aspects compared to directly contacting sensors. Most importantly, the setup time is usually much shorter since the sensors are positioned on the ground near or under the observed bridge, and no directly contacting elements

have to be installed. In addition, the normal bridge operation is not disturbed by this setup process. Remote sensors are generally capable of measuring the bridge's response at several positions simultaneously with a similar accuracy compared to contacting sensors. However, favourable results are only achievable if all external influences are considered. For example, the remote sensing ground-based interferometric radar (GBR) is affected by atmospheric changes or systematic deviations specific to the setup, which can significantly reduce the measurement accuracy and consequently its ability to detect damage.

Additionally, external influences are often measured to identify their effect on the feature estimation. Damage usually causes a minimal change in the estimated features and can be easily obscured by external influences or measurement errors. For example, an increase in the structure's temperature is correlated with a decrease in the natural frequencies caused by the structure's expansion. As a result, natural frequencies are only suitable for damage detection if the temperature relationship is sufficiently determined. Mode shapes, on the other hand, are insensitive to temperature change but can be directly affected by measurement errors. In the case of GBR, errors can result from the specific measurement setup or at different steps in the subsequent processing. Therefore, mode shapes from displacement measurements can only be used as features for damage detection if these errors are removed or their influence on the measurements is estimated.

1.1 Main Objective and Research Goals

The field of infrastructure monitoring with GBR has seen increased development in recent years due to its inherent potential for highly accurate measurements. However, the expected accuracy is often only validated with comparisons to reference sensors in a laboratory context [93] or for inefficient measurement setups [66]. Studies involving realistic experiments at bridges show systematic differences between GBR and other reference sensors. These differences are much higher than the expected measurement precision specified for most GBRs and likely result from external influences and influences from the specific measurement setups. For example, long measurement durations amplify the atmospheric influence in static load tests [44]. Systematic deviations can also result from uncertain signal reflection due to the limited resolution of GBR [26]. While there has been development to address these influences, studies usually lack validation with reference sensors. Additionally, the influence of the introduced processing steps on the resulting measurement uncertainty is rarely considered. Consequently, the capabilities of GBR might be overestimated or unknown. If damage detection is performed on these

measurements, systematic deviations or other effects could not be differentiated from damage.

The main objective of this thesis is to determine and improve these influences and their effect on the measurement uncertainty to enable an accurate assessment of the GBR's capabilities in the context of damage detection for bridges. This objective is to be achieved by addressing the following research goals:

- (1) Improving the accuracy of GBR regarding external and sensor specific influences.
- (2) Developing a reliable assessment of the measurement uncertainty.
- (3) Analysing the potential of GBR in feature estimation for damage detection.

The output of the first two research goals is displacement measurements with corresponding uncertainty estimates, which support the analysis of the third research goal.

1.2 Thesis Outline and Contributions

In the following, the thesis structure and the corresponding contributions of each chapter are outlined. Figure 1.1 illustrates an overview of the structure. The relevant fundamentals are described in *Chapter 2*, starting with the working principle of modern GBR systems. Existing research on these systems and related technology is divided into three parts: processing of GBR measurements, validation with reference sensors, and estimation of features from displacements. The fundamentals chapter concludes with an overview of the bridges investigated in this thesis.

The processing of GBR measurements is described in *Chapter 3* and addresses the first two research goals. An accuracy improvement is achieved by proposing several additional processing steps, which focus on the determination and removal of external influences. At first, signal disturbances are automatically detected and removed to generate a clean displacement measurement. A clean measurement is especially relevant for the next step, which removes the influence of static clutter. The estimation approach, as proposed by several studies (e.g. [17, 86]), is modified with a weight matrix and achieves more reliable results. The next step evaluates changes in the atmospheric refractive index and its influence on the measurements. Since this thesis focuses on the measurement of displacements from dynamic loads, a simple post-processing approach is proposed to remove this influence. Lastly, a three-dimensional projection, as proposed by Li et al. [45], is applied to determine more than one displacement component. The variance propagation is extended to include an uncertainty of the coordinates

used in this projection. Measurement campaigns at two bridges show the relevance of these additional steps, but also highlight the remaining challenges in GBR processing. All processing steps are also evaluated regarding their influence on the measurement uncertainty to generate a conclusive assessment of the GBR's capabilities.

The capabilities are further evaluated in the context of damage detection with natural frequencies to address the third research goal. *Chapter 4* proposes a least squares approach for estimating frequencies from the damped vibration after a vehicle crossing. Frequency changes can indicate damage to the observed structure but are also highly dependent on temperature [33, 92]. Determining the temperature-frequency relationship enables damage detection from the estimated frequencies. The approach is applied to measurement campaigns at two bridges with GBR measurements and strain measurements for validation. Compared to an estimation approach based on the frequency domain decomposition (FDD), the least squares approach requires fewer measurements to reliably detect a simulated damage. It is also possible to determine the influence of vehicle mass on natural frequencies since every vehicle crossing is evaluated separately.

The third research goal is additionally addressed in *Chapter 5*, which discusses an alternative measurement approach for the determination of mode shapes. The approach utilises the smooth concrete surface of bridges to mirror the signal to a reflector on the ground. Therefore, a fixed installation on the structure is not necessary, which extends the measurement potential of GBR to a larger number of bridges. Most importantly, the approach directly determines the vertical displacement, and other components cannot influence the measurement. Consequently, the potential for systematic deviations is reduced, and the resulting mode shapes are more sensitive to damage.

The conclusions of the three research goals of this thesis are summarised in *Chapter 6* together with an outlook for future improvements in processing and sensor technology.

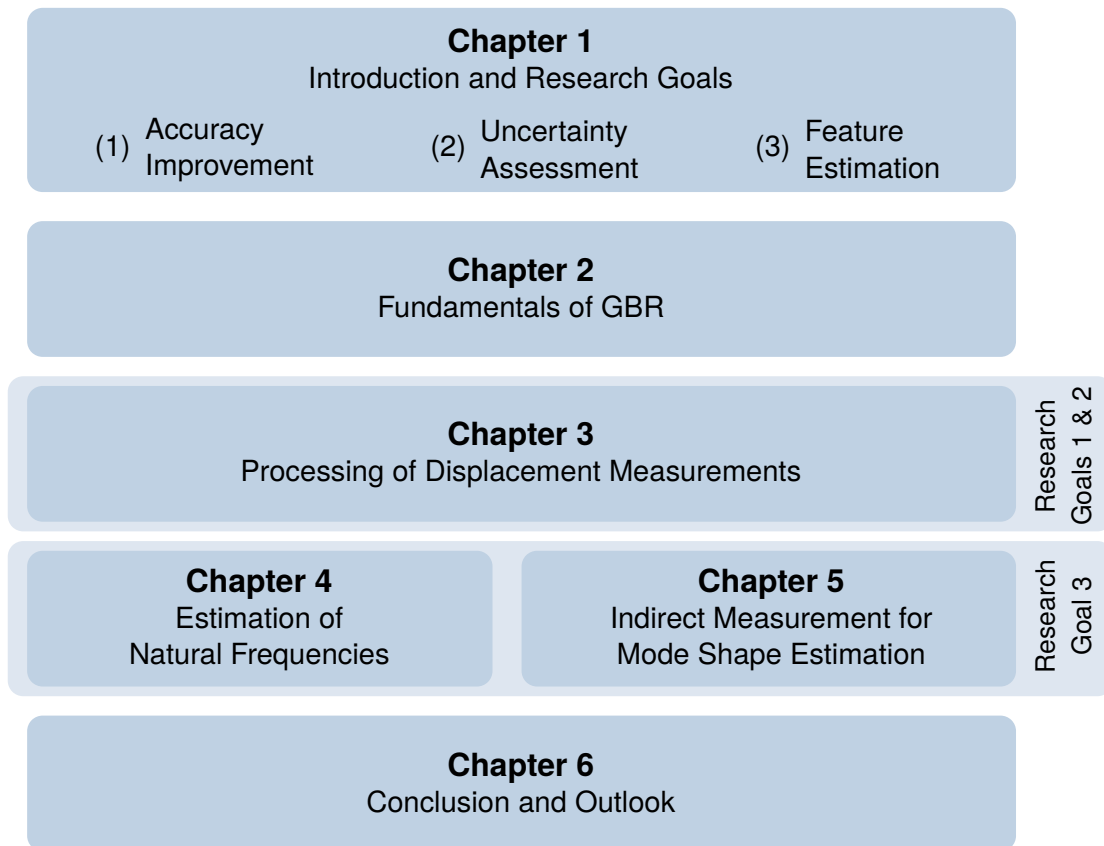


Figure 1.1: Structure of this thesis.

Fundamentals of Ground-Based Interferometric Radar

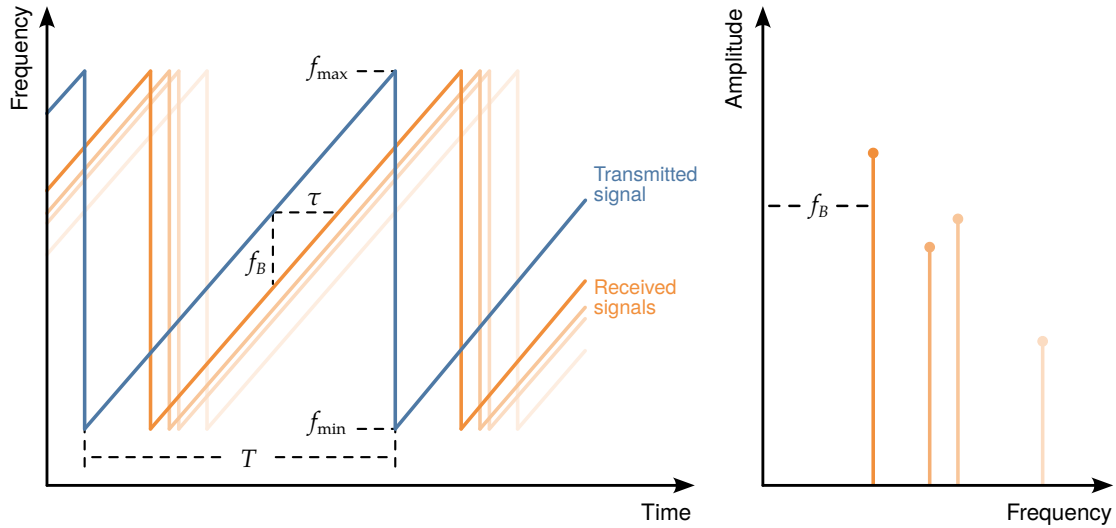
GBR enables measuring the dynamic displacement of multiple points remotely with high accuracy. The basic principle is based on the emission of modulated electromagnetic waves, which are reflected from features at the observed structure. Displacements are determined by measuring the phase differences of the received signal between consecutive time points. Modulation of the emitted signal allows the differentiation of multiple objects by their distance to the GBR. A few commercially available systems as well as prototypes from research institutions are used for displacement measurements of infrastructure objects. The most commonly applied system is Image by Interferometric Survey (IBIS) from IDS (Pisa, Italy). Fast Ground-Based Synthetic Aperture Radar (Fast-GBSAR) from Metasensing (Noordwijk, The Netherlands) constitutes a technologically very similar system.

In the following, the general working principle of GBR is explained, followed by a description of the aforementioned commercial systems, which are applied in this thesis. GBR is also put in context of existing research on infrastructure monitoring with contacting and remote sensors. The chapter concludes with an overview of the bridges investigated in this thesis, which provide the basis for subsequent measurements and analysis with GBR.

2.1 Working Principle

2.1.1 FMCW Radar for Bridge Monitoring

GBRs are usually based on the frequency-modulated continuous-wave (FMCW) principle, however, stepped-frequency continuous-wave (SFCW) was also used for earlier sensors. The principles differ with respect to the modulation of the emitted electromagnetic wave. SFCW increases the frequency stepwise, whereas FMCW uses a linear increase.



(a) Frequency modulation as a function of time with signal delay τ , beat frequency f_B , and sweep time T . (b) Amplitude spectrum of beat frequencies.

Figure 2.1: Linear frequency modulation of frequency-modulated continuous-wave (FMCW) systems with transmitted and received signals.

Figure 2.1a shows the frequency modulation of FMCW as a function of time. During the time of one sweep T , the frequency is linearly modulated from the minimum to the maximum frequency spanning the bandwidth B . The signal reflected from an object is received by the GBR with the time delay

$$\tau = \frac{2d}{c} \quad (2.1)$$

which depends on the distance d of the object from the sensor and the speed of light c . However, instead of measuring the time delay directly, the transmitted and received signals are mixed to determine the beat frequency f_B , which is proportional to the time delay. Reflections from multiple objects produce different beat frequencies, which form a frequency spectrum (see Figure 2.1b). By applying an inverse discrete Fourier transform (IDFT) to the spectrum, the signals of these objects can be differentiated by their distance to the GBR. Consequently, the minimum distance to distinguish two objects is determined by the resolution of the IDFT, which depends on the bandwidth B . This minimum distance is also called range resolution:

$$\delta_d = \frac{c}{2B} \quad (2.2)$$

The range resolution divides the emitted signal into spherical cone segments, also called range cells. Objects in the same range cell cannot be distinguished since the GBR's real aperture has no angular resolution. However, an additional modulation can enable

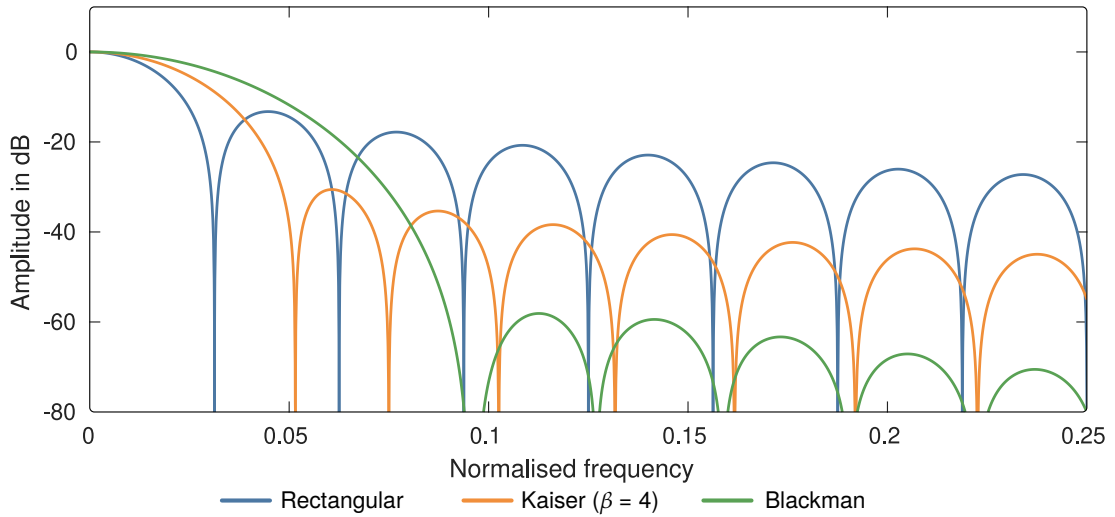


Figure 2.2: Amplitude spectrum of different window functions.

angular resolution by creating a synthetic aperture. This modulation is usually achieved by movement of the antenna, which significantly reduces the sampling frequency. Lastly, the frequency modulation also determines the sampling frequency and the maximum distance to a target. A higher maximum distance requires a longer receiving time of the signal, limiting the sampling frequency.

The default rectangular window of the IDFT produces significant side lobes since the sweep time is finite. Therefore, a window function is first applied to the frequency spectrum to reduce the influence of multiple reflections on each other. Window functions are characterised by their frequency response, which is shown for some examples in Figure 2.2. The functions differ mostly in regard to their main lobe width and side lobe attenuation. For example, the Kaiser window has greater side lobe attenuation at the expense of a wider main lobe compared to the rectangular window. Applied to range resolution, this means that the Kaiser window suppresses the influence of objects in different range cells on each other, while the resolution of each cell decreases. Even greater side lobe suppression is achieved with a Blackman window.

Besides mixing the received signals with the originally transmitted signal, they are additionally mixed with a phase-shifted version of the original signal. The phase-shift by 90° enables a reconstruction of the received signals' phase information since the resulting in-phase and quadrature (IQ) components are complex-valued. The wrapped phase ϕ_w and the amplitude A result from the argument and the absolute, respectively:

$$\phi_w = \arctan\left(\frac{Q}{I}\right) \quad (2.3)$$

$$A = \sqrt{I^2 + Q^2} \quad (2.4)$$

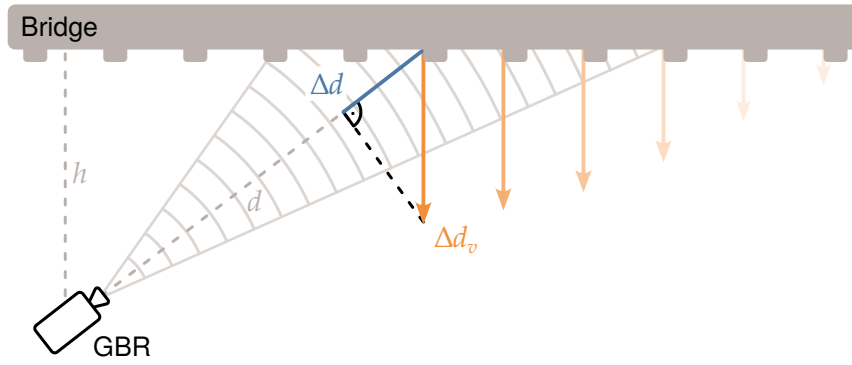


Figure 2.3: Measurement principle of ground-based interferometric radar (GBR) with vertical displacements Δd_v and displacements in line of sight (LOS) Δd .

Since the phase is wrapped to the interval $[-\pi, \pi)$ and the phase ambiguity is unknown, only relative displacement between two consecutive sample points can be determined. The phase is unwrapped by adding or subtracting 2π when the difference between consecutive sample points is greater than π . After unwrapping, the phase difference $\Delta\phi_{uw}$ relates to the displacement Δd by the signal wavelength:

$$\Delta\phi_{uw} = -\frac{4\pi}{\lambda}\Delta d \quad (2.5)$$

Bridge monitoring with GBR usually follows the same basic principles. The objective is to determine vertical displacements at several locations on the underside of the bridge. Since GBR can only distinguish objects by their distance, the sensor head has to be tilted, as shown in Figure 2.3. The signal lobe covers a large part of the bridge underside. At the same time, the reflective features of the bridge, subsequently called targets, are separated into different range cells. Reflective features can be, for example, orthogonal trusses or beams with sizes greater than the signal wavelength. Additional angular resolution can be achieved by moving the antennas, which creates a synthetic aperture. However, the antenna movement requires several seconds or minutes, preventing the measurement of dynamic displacements. Ground-based synthetic aperture radar (GBSAR) is therefore rarely used for infrastructure monitoring. Although, some use cases are given in Section 2.2. Under the assumption that bridges are primarily displaced in the vertical axis, a projection has to be applied since GBR always measures displacement in its line of sight (LOS). This projection depends on the respective slant distance d between sensor and target, and on the height h of the bridge relative to the sensor. The vertical displacement Δd_v results from

$$\Delta d_v = \Delta d \cdot \frac{d}{h} \quad (2.6)$$

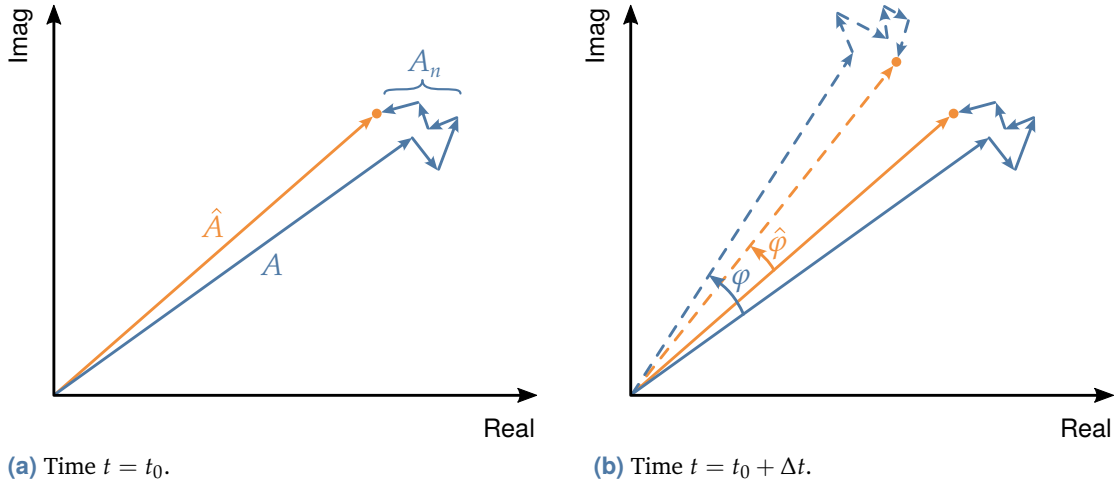


Figure 2.4: Phasor plots of a measurement \hat{A} consisting of a dominant reflection A and noise A_n for two consecutive sample points. The measured phase $\hat{\varphi}$ differs from the true phase φ .

2.1.2 Estimation of Measurement Uncertainty

The phase measurement contains multiple noise components, for example, the sensor's thermal noise, changes in atmospheric properties, or contributions from multiple individual scatterers. Most of these components can only be determined statistically. Hence, their influence on the phase measurement is estimated with an uncertainty value. The measurement of a single target is visualised with a phasor plot of the complex-valued IQ components in Figure 2.4a. The target's dominant reflection with the amplitude A is superimposed with multiple smaller components, which are summarised with A_n . After the time step Δt , the measured phase $\hat{\varphi}$ differs from the target's true phase φ , as shown in Figure 2.4b. The resulting uncertainty of the phase measurement is estimated from the signal-to-noise ratio (SNR), which is the relation of signal power to noise power.

By modelling the multiple components A_n as additive white Gaussian noise, their power is defined with the variance σ_n^2 of the two IQ components [17]:

$$A_n^2 = 2\sigma_n^2 \quad (2.7)$$

The power of the signal A^2 is the squared amplitude of the target reflection. In practical terms, these two values cannot be determined separately. Instead, they are estimated from the statistical properties of the amplitude. The signal power is derived from

the mean value m_A , whereas the noise power results from the standard deviation σ_A . Consequently, the SNR is determined with [17]:

$$\text{SNR} = \frac{m_A^2}{2\sigma_A^2} \quad (2.8)$$

The uncertainty of the phase measurement is inversely proportional to the SNR. However, the exact definition of this relationship differs slightly between authors. The following two definitions can be found:

$$\sigma_{\Delta\phi} = \frac{1}{\sqrt{2\text{SNR}}} \quad (2.9)$$

$$\sigma_{\Delta\phi} = \frac{1}{\sqrt{\text{SNR}}} \quad (2.10)$$

Rödelsperger et al. [86] and an unpublished technical report by IDS [39] give the definition of Equation 2.9, whereas Coppi et al. [17] use the definition of Equation 2.10. Coppi et al. [17] are also referenced by several other authors [50, 51, 97, 101]. Since the closely related research of laser speckle by Dainty [19] supports the first definition, this thesis relies on Equation 2.9 to estimate the phase uncertainty. Finally, the displacement uncertainty results from:

$$\sigma_{\Delta d} = \frac{4\pi}{\lambda} \cdot \frac{1}{\sqrt{2\text{SNR}}} \quad (2.11)$$

Typically, a displacement uncertainty in the sub-millimetre range can be achieved. An SNR of 20 dB results in a displacement uncertainty of 0.1 mm. The lowest possible uncertainty of 0.02 mm is reached at an SNR of 35 dB [39].

2.1.3 IBIS and FastGBSAR

The most commonly applied GBRs for bridge monitoring are IBIS [28] and FastGBSAR [85], which are used in this thesis. While an earlier version of IBIS used the SFCW principle, the current version and also FastGBSAR are FMCW radars in the K_u -band. Both systems reach a modulation bandwidth of 300 MHz at a centre frequency of 17.2 GHz resulting in a range resolution of 0.5 m. However, the usable bandwidth is restricted to 200 MHz in most countries due to regulatory requirements, which reduces the range resolution to 0.75 m. One of the main differences between the two systems is the maximum distance to an object and the maximum sampling frequency. IBIS achieves a maximum distance of 1 km, whereas FastGBSAR reaches 4 km. The maximum sampling frequency is 200 Hz and 4000 Hz, respectively. However, both extreme values cannot

be reached at the same time, since greater distances lead to longer durations for each sampling step, as discussed earlier. Lastly, the sensor's antennas determine the signal beam characteristics. IBIS has an antenna gain of 19 dBi. The beam width is 15° in the horizontal plane and 17° in the vertical plane at an attenuation of 3 dB. At a beam width of 34° horizontally and 45° vertically, the attenuation increases to 10 dB [39]. Similarly, FastGBSAR achieves an antenna gain of 15 dBi and a beam width of 32° [54]. The attenuation or orientation of this beam width is not specified.

This thesis measures displacements with two sensors at the same time to determine two components of the three-dimensional displacement vector (see Section 3.1.4). However, using two FMCW radars in direct proximity to each other can cause interference, since the same frequency band is used [4]. In the case of IBIS, the interference triggers an alarm that shuts down one of the sensors. While a specific measurement setup still enables simultaneous measurements without interference, a lot of flexibility is lost, as discussed in Section 3.2.1. Therefore, two FastGBSAR sensors are used in some of the measurements of this thesis. The two sensors receive a pulsed time signal from the global navigation satellite system (GNSS) to synchronise the internal clock. To prevent interference, the signal transmission is alternated between the sensors at each frequency sweep. Consequently, the sampling frequency is halved.

2.2 Existing Research on GBR

GBR has been used extensively for various monitoring tasks since the early 2000s. A common task is the measurement of bridge displacements for the purpose of condition assessment [76]. Besides, GBR is also applied to the monitoring of other structures such as buildings [3, 35, 65], wind turbine towers [7, 77], historic towers [8, 14], or other kind of slender structures [31, 50, 68, 94]. Additionally, GBR can be used to determine the modal properties of cables [27, 95]. Most of these monitoring tasks are accomplished with the real aperture mode since the synthetic aperture mode generally has a low sampling frequency, which is not sufficient for measuring dynamic displacements. In some cases, the synthetic aperture mode is used to determine the static displacement of bridges [20, 59, 75]. However, it is applied mainly to the monitoring of landslides [13, 49], dams [2], open mines [86, 89], or walls [79] since the displacement rates are low compared to the sampling frequency. In the following, existing research on infrastructure monitoring with GBR is structured into three categories: processing of measurements, comparison and validation with other sensors, and estimation of features from the processed measurements.

2.2.1 Processing of GBR Measurements

Most studies apply the conventional setup and processing approach discussed in Section 2.1. However, some studies propose additional processing steps or more complex setups to address specific challenges. For example, estimating the atmospheric influence on displacement measurements is an important element of GBSAR processing and can be adapted to GBR as well. A popular method uses persistent scatterers as a stable reference to remove the atmospheric influence on the entire measurement area [70]. Stable references are also applicable to dynamic displacement measurements [86]. Alternatively, the atmospheric parameters are measured to estimate the refractive index with empiric formulas [38, 48, 49]. Apart from the atmosphere, several studies identify static clutter as an important influence on displacement measurements [17, 35, 86, 99]. Static clutter results in a systematic deviation and can be estimated from a phasor plot of the IQ components. The estimation can be challenging for small displacements since the phasor plot forms a circular arc instead of a full circle. Guo et al. [32] divide the FMCW frequency modulation of a W-band radar into segments to extend the circular arc and improve the estimation results. In the case of multiple-input multiple-output (MIMO) radars, an adapted estimation approach can also improve the accuracy of clutter removal [104].

The conventional processing approach assumes that the vertical displacement is dominant, while horizontal displacements are negligible. However, this assumption may not be applicable, as shown by Dei et al. [20] or Firus et al. [26]. The displacements in LOS are composed of both the vertical and horizontal components, and a projection to the vertical axis leads to significant errors. It is possible to avoid this projection error by using a vertical measurement setup [66], but the number of measurement points is reduced and the signal footprint is comparatively large. Alternatively, multiple simultaneous measurements from different positions can be used to determine two or three displacement components. Mecatti et al. [53] show the basic projection principle in a laboratory environment with a MIMO GBR, which uses three channels to generate multiple measurements of the same target from different positions. With known geometric relations of the target and the antennas, the two-dimensional displacement vector of a movable target is determined. Li et al. [45] generalise the projection principle so that any number of measurements can be used to generate the best estimate of the displacement vector. Most studies concerning the three-dimensional projection subsequently apply this principle. However, the actual implementation differs regarding the applied sensors and setups. For example, Miccinesi et al. [57] use a MIMO GBR with two channels to determine three components by exploiting an additional bistatic measurement. This implementation does not allow for a great variety between the antenna positions since

the bistatic measurement requires a similar field of view between the antennas. More flexibility can be achieved with a multi-monostatic approach [56]. Miccinesi et al. [58] substitute antenna cables with wireless transmission to increase the distance between two antenna positions, improving the accuracy. Greater flexibility is also achieved with two separate sensors. For example, Talich et al. [94] position two GBRs perpendicular to each other to determine the two-dimensional horizontal displacement of a water tower. Furthermore, Olaszek et al. [71] demonstrate that the vertical displacement of a bridge, estimated from two independent GBRs, agrees well with a displacement transducer.

Determination of the three-dimensional displacement vector is also relevant for GBSAR measurements. Similarly to GBR, multiple sensors are applied to estimate the separate components. For example, Severin et al. [89] measure the displacements of a slope in an open pit mine. Michelini et al. [62] propose various measurement setups and show the advantages of multi-monostatic and bistatic approaches. An experimental verification of the projection principle is performed by Deng et al. [21]. In the experiment, three MIMO GBSAR measure the displacement of a reference target that can be moved in three dimensions. The achieved accuracy is compared to a theoretical value, which results from the geometric relations of the three sensors. Other studies perform similar accuracy evaluations [96, 102].

In the case of GBR, accuracy evaluations beyond comparisons to other sensors are uncommon. Usually, the measurement uncertainty is estimated from the SNR [17, 86]. The precision is additionally validated by measuring the displacement of a movable reflector in a laboratory environment [35, 45, 53, 80, 98]. In some cases, the influences of certain processing steps are considered. For example, Xiong et al. [99] discuss the uncertainty of clutter estimation. Most studies, which implement a three-dimensional projection, also propagate the measurement uncertainties in LOS with the respective projection principle. The uncertainties of the projected displacements are determined by the geometric relations of the sensors and targets [21, 45, 100]. However, the uncertainty of the geometry measurements itself is considered to be negligible if the targets are well known [57].

2.2.2 Comparison to Other Sensors

Infrastructure monitoring relies on a variety of sensors with different advantages and challenges during the measurement and subsequent processing. At first, the most common sensors and their characteristics are compared to GBR, followed by a summary of experimental studies for the purpose of validating the GBR's measurement principle.

Most conventional sensors are directly contacting and provide point-wise measurements. A commonly applied example are strain sensors, which measure the strain at their installation position. These sensors can range from small one-dimensional electrical types to long continuous runs of fibre optic sensors [43]. Strain is generally measured with an SNR similar to the displacement measurements of GBR. Other directly contacting sensors are accelerometers. Compared to GBR, accelerometers provide more sensitive measurements for modal analysis due to the proportionality of displacement and acceleration with the squared frequency. However, the measurement range is usually restricted to frequencies above 0.5 Hz to 1 Hz depending on the accelerometer. In general, installing directly contacting sensors can be complex and requires considerable setup time.

Remote sensing technology provides a valid alternative to contacting sensors. For example, vision-based systems measure two- or three-dimensional displacements of multiple points with similar precision as GBR [11, 36]. Usually, identifiable targets have to be installed at the observed structures, especially for longer distances, thus preventing contactless measurements. Total stations can accurately determine the absolute three-dimensional displacement of single points. The precision is about one or two orders of magnitude lower than GBR, although the accuracy can generally be equal or higher, especially for static measurements [44]. Dynamic measurements are restricted to low-frequency displacements, since the sampling frequency is limited. However, higher sampling frequencies are possible with a combination of a vision-based approach in an image-assisted total station [106]. The maximum achievable ranges are comparable to GBR in practical applications. Higher precision than total stations is achieved with laser Doppler vibrometers, which measure one-dimensional displacement and velocity of single points [15, 64]. While scanning vibrometers can also measure displacements of multiple points, the evaluable area is comparatively small and the sampling frequency decreases.

Lastly, terrestrial laser scanners (TLS) provide a compromise between precision, measurement area, and sampling frequency. A TLS can either operate in a three-dimensional scanning mode to determine static displacements [82] or in a two-dimensional mode to determine dynamic displacements along a profile [55, 87]. In profile mode, a rotating mirror generates two-dimensional point clouds with a repetition rate of about 50 Hz to 200 Hz. Singular measurements of angle and distance have low accuracy and are not reproducible. Thus, spatial clustering averages multiple points to determine one representative point. The displacement of this point is determined by repeating the clustering for each profile scan, resulting in a displacement uncertainty of about 0.1 mm to 0.2 mm. Typically, the cluster size is in the range of 0.5 m to 1 m, which is similar to the GBR's range resolution. Contrary to GBR, TLS requires smooth surfaces for optimal

Table 2.1: Existing research for comparison and validation of GBR with other sensor technology depending on the compared features. Laser sensors include terrestrial laser scanners, total stations, and displacement laser sensors.

Sensors	Features	References
Laser sensor	Displacement	[44, 66, 93]
	Natural frequencies	[7, 66]
Displacement transducer	Displacement	[26, 71, 88, 93]
	Natural frequencies	[26, 72]
Hydrostatic level	Displacement	[37]
Velocity sensors	Velocity	[29]
	Natural frequencies	[29, 30, 65]
	Mode shapes	[29, 65]
Accelerometer	Displacement	[56, 57, 66, 88]
	Acceleration	[27]
	Natural frequencies	[3, 24, 26, 27, 37, 66, 91]
Finite element method	Natural frequencies	[14, 41, 65, 68]
	Mode shapes	[34, 65]

signal reflection and clustering. Vertical or horizontal displacement is measured directly, and systematic deviations are comparatively minor. Although the precision is generally an order of magnitude lower than the precision of GBR, TLS can still provide appropriate reference measurements for the validation of GBR.

A comparison to other sensor technology is an important step in validating the GBR's measurement principle and for an accurate assessment of its uncertainty. Several different sensors are used for comparison, as summarised in Table 2.1. The validation is addressed either by directly evaluating displacements or by comparing different features estimated from the measurements. For example, Su et al. [93] perform a comparison between a laser displacement sensor and a GBR in a laboratory setting. The displacements measured by both sensors agree well, and differences can be explained by the sensors' measurement setup. A comparison to TLS at a bridge shows good agreement as well [66]. However, the displacement of only a single point is measured since the GBR is positioned vertically under the bridge. Possible systematic deviations or scenarios with low signal reflection cannot be evaluated from this study. An example of a possible error source is highlighted by Kuras et al. [44] in a static load test. The differences between a GBR and a total station increase over time due to changes in the atmospheric properties affecting the GBR's measurements. Differences are also found by Firus et al. [26] in a comparison to displacement transducers, which result from an error in the projection of the measurements in LOS to the vertical axis. This error is likely caused by the

wide signal beam preventing a successful identification of the target's coordinates. A horizontal displacement component could also influence the measurements in LOS. This horizontal component can be determined by applying two GBRs, which results in good agreement between the GBRs and a displacement transducer [71]. Large differences are also observed by Huang et al. [37] in a comparison to a hydrostatic level. However, the cause of these differences cannot be accurately determined since the hydrostatic level has a sampling frequency of 1 Hz and is therefore not a suitable reference sensor for dynamic displacement measurements.

Besides direct comparisons of displacements, the GBR's measurement principle can also be validated indirectly by comparing features estimated from the measurements. Especially features that are invariant to the measurement type allow for a greater variety of sensors. For example, natural frequencies or mode shapes derived from velocity sensors or accelerometers can be directly compared to the same features derived from displacements of a GBR. Natural frequencies show good agreement for velocity sensors [29, 65] and for accelerometers [3, 26, 27, 37]. However, these comparisons do not support a comprehensive evaluation of the GBR's measurement principle since systematic deviations or external influences have no effect on the natural frequencies. Mode shapes, on the other hand, are sensitive to these influences if the effect is not systematic. The calculation of mode shapes from displacement measurements is shown by Gentile et al. [29] for a bridge. The results of GBR correspond well with the results of the velocity sensors. However, the measurements cover a much smaller area of the bridge since corner reflectors have to be used for sufficient signal reflection. At a different bridge, the comparison of GBR and velocimeter is also successful, even though the ordinary measurements experience a scaling error [30]. Since this error is systematic for all measurement points of the GBR, it is not reproduced in the unscaled mode shapes.

Besides comparisons with other sensors, the GBR can also be evaluated by comparisons with a model from the finite element method (FEM), which estimates the dynamic behaviour of a structure from known or assumed properties. For uncalibrated models, the differences in the estimated natural frequencies are usually larger compared to differences between GBR and other sensor technology. However, it is still possible to characterise the GBR's capability to identify and distinguish separate frequencies [14, 41] and their corresponding mode shapes [34, 65].

2.2.3 Feature Estimation with GBR

The features estimated from the displacement measurements are not only used for comparisons with other sensors but also form the basis for damage detection approaches. Natural frequencies and mode shapes are the most common features determined from GBR measurements. The estimation of these features is achieved through several different methods, as summarised in Table 2.2. Most studies apply frequency-domain methods to determine natural frequencies. An easy and straightforward method is the calculation of the amplitude spectrum with a discrete Fourier transform (DFT). For example, Miccinesi et al. [56] estimate four dominant frequencies of a bridge. A MIMO GBR enables the determination of two displacement components and their respective amplitude spectra. The frequencies mainly differ in regard to their amplitude between the two components. However, one frequency is only visible in the spectrum of the vertical component. Owerko et al. [72] determine eight dominant frequencies in the amplitude spectrum of a bridge from GBR measurements, whereas 15 frequencies are identifiable from the spectra of acceleration sensors and displacement transducers.

A higher SNR is often achieved by calculating the power spectral density (PSD) matrix from overlapping segments of the measurements. The PSD matrix is either calculated from the autocorrelation function [27] or the cross-correlation function of different measurement points [3, 14]. Besides frequency-domain methods, the natural frequencies are also estimated in the time domain. For example, Neitzel et al. [66] estimate the parameters of a damped vibration after a vehicle crossing with least squares. The resulting frequency and uncertainty values are compared between different sensors. Liu et al. [47] implement a variant of the stochastic subspace identification (SSI) to estimate frequencies and damping ratios of bridge displacements.

Table 2.2: Existing research for feature estimation from GBR measurements. Methods depending on the power spectral density vary slightly between studies, but are aggregated under this term.

Features	Methods	References
Natural frequencies	Discrete Fourier transform	[31, 56, 68, 72, 91]
	Power spectral density	[3, 14, 24, 27, 37]
	Frequency domain decomposition	[41]
	Stochastic subspace identification	[47]
	Least squares	[66]
Natural frequencies and mode shapes	Frequency domain decomposition	[8, 29, 34, 35, 50]
	Other or unknown method	[26, 65, 86]

Mode shapes are generally estimated with the FDD, which applies a singular value decomposition (SVD) to the PSD matrix. The natural frequencies and mode shapes result from the singular values and vectors, respectively. Multiple modes are retrieved from the displacement measurements with the FDD. For example, Gentile et al. [29] estimate four mode shapes for a concrete bridge, whereas Luzi et al. [50] determine six mode shapes for a cable-suspended bridge.

2.3 Overview of Investigated Bridges

A comprehensive investigation of GBR requires several experimental campaigns to evaluate the measurement principle and the subsequent processing of the acquired data. Ideally, the observed structures vary considerably in size, construction type, reflective features, or other properties relevant to the GBR's measurement principle. Table 2.3 gives an overview of the bridges utilised for measurements in this thesis. Most importantly, the bridge length and the type of signal reflection are varied. For example, the bridge in Schneckelohe is a small concrete bridge that requires corner reflectors, whereas the much longer bridge at Maxau has orthogonal trusses, which can be used for signal reflection. Both bridges are investigated in Chapter 3 regarding the processing of GBR measurements and the validation of its measurement principle with a reference sensor.

Additionally, Schneckelohe is used in Chapter 4 together with the bridge in Seßlach to analyse the temperature influence on natural frequencies with displacement measurements. Lastly, the smooth concrete surface of the bridge at the Pulverhausstraße provides a suitable test site for an alternative measurement setup in Chapter 5. In the following, the bridges are introduced in more detail, whereas the specific measurement setups are discussed together with their respective results in each chapter.

Table 2.3: Overview of the investigated bridges and their properties.

Name	Type	Length in m	Number of fields	Signal reflection	Referenced in section
Schneckelohe	concrete	26 m	1	Reflectors	3.2.1 and 4.3.1
Maxau	steel truss	292 m	2	Trusses	3.2.1
Seßlach	concrete	56 m	2	Reflectors	4.3.1
Pulverhausstraße	concrete	114 m	4	Beams	5.2.1 and 5.3.1

2.3.1 Schneckenlohe

The bridge in Schneckenlohe (near Coburg, Germany) is a prestressed concrete structure with two longitudinal T-beams constructed in 2005. With a length of 26 m and a width of 11 m, the bridge is representative for a large number of small bridges in the German road network. As part of the federal road B 303, the bridge has one lane for each traffic direction and crosses the district road KC 29 (see Figures 2.5a and 2.5b). Installing corner reflectors in the middle of each beam provides additional signal reflection and allows for more flexible measurement setups. The measurements in Schneckenlohe are used to investigate the performance of the proposed processing steps in Chapter 3. Additionally, the results of multiple measurement campaigns over two years are analysed in the context of natural frequency estimation in Chapter 4. Strain sensors in direct proximity to the reflectors are used for the validation of this analysis.

2.3.2 Maxau

The railway bridge at Maxau (near Karlsruhe, Germany) consists of two independent steel truss structures spanning the river Rhine. Initially, the bridge was constructed as a single-track railway in 1991 and upgraded with a second track in 2000. Although both parts of the bridge have a common central pillar, they are otherwise completely independent. The bridge has a total length of 292 m and two fields with a continuous truss (see Figures 2.5c and 2.5d). Since the orthogonal trusses on the underside of the bridge provide sufficient signal reflection, no additional installation of reflectors is required. In combination with Schneckenlohe, the measurements at Maxau provide further opportunities for investigating the processing's performance in Chapter 3. Validation of the processing is achieved with a direct comparison with TLS measurements, which also highlights the challenges and ongoing effort in remote monitoring with GBR.

2.3.3 Seßlach

The bridge in Seßlach (near Coburg, Germany) is a prestressed concrete structure with two spans. Each span is 28 m long and consists of five longitudinal T-beams (see Figures 2.5e and 2.5f). The bridge is part of the federal road B 303 and has one lane for each traffic direction. Additional reflectors provide sufficient signal reflection for more flexible measurement setups similar to Schneckenlohe. In Chapter 4, the results of multiple measurement campaigns over two years are used to investigate the estimation of natural frequencies in the context of damage detection. An additional temperature sensor

allows for the analysis of temperature changes on natural frequencies. This investigation is also supported by a comparison with the measurements from strain sensors installed in the middle of each beam.

2.3.4 Pulverhausstraße

The bridge over the Pulverhausstraße in Karlsruhe (Germany) is a prestressed concrete structure with four spans and two continuous T-beams, as shown in Figures 2.5g and 2.5h. The two inner spans have a length of 34 m, whereas the two outer spans are shorter at 23 m. As part of the state road L605, the three unidirectional lanes lead traffic from the motorway A5 to the federal road B10 and the city centre. Hence, the traffic volume is much higher than it is for the other two road bridges in Schneckenlohe and Seßlach. Chapter 5 proposes an indirect measurement principle, which is applied at the Pulverhausstraße and validated with two reference sensors. The principle is also used for the determination of mode shapes.



(a) Side view of Schneckenlohe.



(b) Installed reflectors in Schneckenlohe.



(c) Side view of Maxau.



(d) Bridge underside of the eastern field at Maxau.



(e) Side view of Seßlach.



(f) Installed reflectors in Seßlach.



(g) Side view of the Pulverhausstraße.



(h) Measurement setup at the Pulverhausstraße.

Figure 2.5: Overview of the investigated bridges.

Processing of Displacement Measurements from Ground-Based Radar

This chapter includes material from

C. Michel and S. Keller. “Advancing Ground-Based Radar Processing for Bridge Infrastructure Monitoring”. In: *Sensors* 21.6 (Mar. 2021), p. 2172. DOI: [10.3390/s21062172](https://doi.org/10.3390/s21062172).

It is cited as [60] and marked with a [blue line](#).

Conventional GBR processing generates one-dimensional displacement measurements and an estimate of the corresponding uncertainty. For simple measurement setups, the processing results sufficiently reproduce the actual behaviour of the observed structure. However, most setups are complex and entail several challenges that are not considered by the conventional approach. This chapter addresses these challenges to generate accurate displacement measurements and a more reliable estimate of their uncertainty. At first, however, the conventional processing is summarised to motivate the adapted methodology.

Figure 3.1 shows the workflow of conventional processing in blue. The complex-valued IQ components are initially in the time-frequency domain, since GBR determines the beat frequency of reflected signals (see Section 2.1.1). An IDFT transforms the IQ components to the time-range domain enabling a distinction between different reflective targets. The wrapped interferometric phase and the amplitude result from the argument and the absolute of the IQ components. Displacements are calculated by unwrapping the phase. Since displacements are always measured in LOS of the GBR, a projection factor is applied to determine displacements in the vertical axis. An estimation of the measurement uncertainty results from the SNR of the amplitude.

The conventional processing is extended in several ways to account for external influences and challenging measurement setups, which is shown in the orange part of Figure 3.1. At

first, disturbances to the displacement measurements, which are caused by objects passing through the signal, are detected and removed. Afterwards, the influence of static reflections is estimated. The estimation approach, proposed by e.g. Rödelsperger et al. [86] or Coppi et al. [17], is adapted to achieve a more reliable estimation even for long measurement durations. Changes in the atmospheric refractive index are evaluated in the next processing step since their influence on the propagation of microwaves is significant. Two approaches from GBSAR processing are evaluated in the context of bridge monitoring [49, 86]. Additionally, a post-processing approach for the removal of the atmospheric influence is proposed. Lastly, the projection of displacements in LOS is expanded from a one-dimensional to a three-dimensional approach, which determines displacements in a Cartesian coordinate system, as proposed by Li et al. [45]. All additional processing steps have an influence on the measurement uncertainty. Therefore, this influence is evaluated after each step to generate a reliable assessment of the resulting displacement uncertainty.

Measurement campaigns at two bridges provide the basis of a comprehensive evaluation of these additional steps. The advantages and challenges are illustrated by a comparison to a reference sensor.

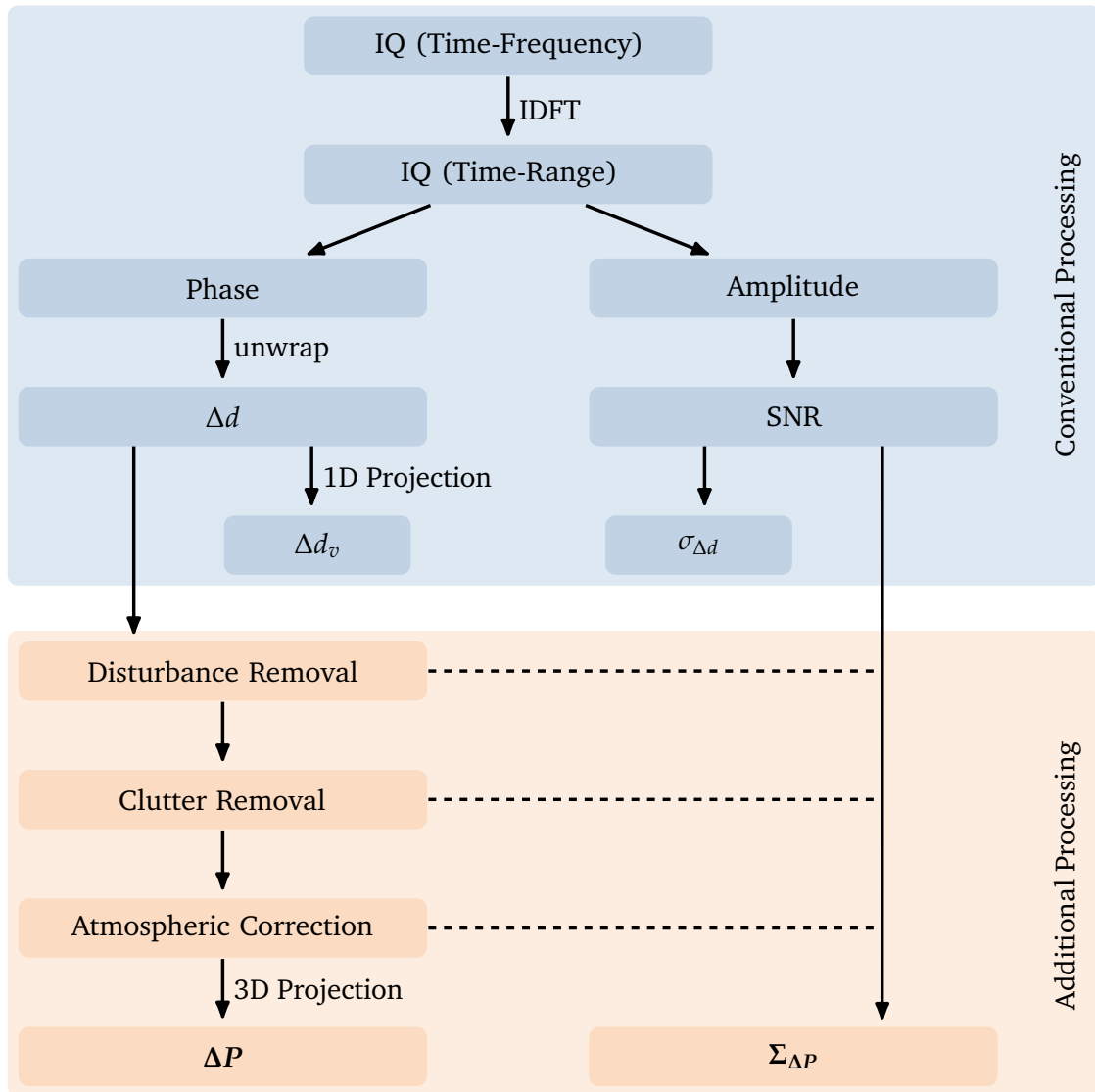


Figure 3.1: GBR processing of complex-valued raw measurements to one-dimensional displacements Δd_v and the corresponding uncertainty $\sigma_{\Delta d}$ in blue. Additional processing of displacements in LOS to a three-dimensional displacement vector ΔP with the corresponding uncertainty $\Sigma_{\Delta P}$ in orange.

3.1 Methodology

3.1.1 Removal of Disturbances

Most of the following GBR processing steps are based on the assumption that the measurements only contain undisturbed bridge displacements. Any disturbances in the GBR signal have to be removed beforehand, in order not to influence subsequent processing steps. The most common cause of a disturbance is a person, vehicle, or other object passing through the signal at the same range as the target. The GBR cannot distinguish this passing object from the actual measurement target if they are in the same range cell, since the GBR does not have cross-range resolution. The passing object is usually moving quickly and non-deterministic, which leads to broadband noise being superimposed on the phase and amplitude time series. Additionally, a jump in the unwrapped phase time series can occur. The removal of disturbances changes the variance of the amplitude time series. Therefore, the SNR and measurement uncertainty have to be estimated again after the removal.

Phase Jumps

In the detection and removal steps, we separate disturbances with phase jumps from disturbances without jumps. Phase jumps are usually caused by a phase unwrapping error. As mentioned in Section 2.1.1, the unwrapping process removes jumps caused by exceeding the phase interval. A value of 2π is added or subtracted if the phase difference between consecutive samples is greater than π . A disturbance can also cause a difference greater than π without exceeding the phase interval. This is then falsely corrected with 2π during unwrapping, resulting in a jump. The jumps are detected by looking for rapid changes in the unwrapped phase, applying a median filter window, and differencing the resulting values once. Jumps are easily identified by a threshold calculated as a multiple of the standard deviation of the differenced median values. It is important to choose a suitable window length for the median filter. The window length should not be greater than the time between two jumps, as this could mask the individual jumps. Simultaneously, a shorter window can introduce too much noise to the median values. False positives occur if the window length approaches the duration of a vehicle crossing.

Broadband Noise

Disturbances without phase jumps can generally be characterised as broadband noise. Typically, the frequency range for displacements of bridges or other large structures is very low. Therefore, a high-pass filter with a cut-off frequency of around 15 Hz eliminates the mostly deterministic components in the low-frequency range. Thus, only sensor noise and broadband disturbances remain. As sensor noise can usually be characterised as white noise and is smaller than the noise caused by disturbances, a threshold is used to detect the disturbances. Ideally, the threshold would be determined as a multiple of the sensor noise standard deviation. However, since the calculation of the standard deviation includes the disturbances, the threshold value is likely too high and false negatives occur. Therefore, the removal of disturbances is implemented as an iterative process. Every iteration recalculates the standard deviation, thus reducing the threshold until it converges. The final threshold value determines the smallest detectable disturbance for a given standard deviation.

3.1.2 Clutter Removal

The measurement can be influenced by unwanted targets in the same range cell as the measurement target, as GBR always measures the sum of the complex-valued IQ components. This clutter can be removed if it results from static targets that have a systematic influence on the measurement [17, 86]. The effect is best shown in a phasor plot of the complex signal (see Figure 3.2a). A moving target's phasor plot shows a circular arc with a radius R corresponding to the signal amplitude and a central angle φ corresponding to the signal phase. Static clutter increases the signal amplitude but has no effect on the phase. Therefore, it adds a systematic deviation to the origin of the arc, and the phase and amplitude of the moving target are over- or underestimated with $\hat{\varphi}$ and \hat{R} . Since the measurement uncertainty is dependent on the mean value of the amplitude, it is over- or underestimated as well. In the following, we propose a combination of two circle fit algorithms already used in various other disciplines to estimate the true origin (x_m, y_m) of the arc. The combination of two algorithms is necessary because bridge displacements usually do not produce a full circle, only a circular arc with a small central angle. The proposed combined approach estimates the origin more reliably. Further challenges in circle estimation are addressed as well.

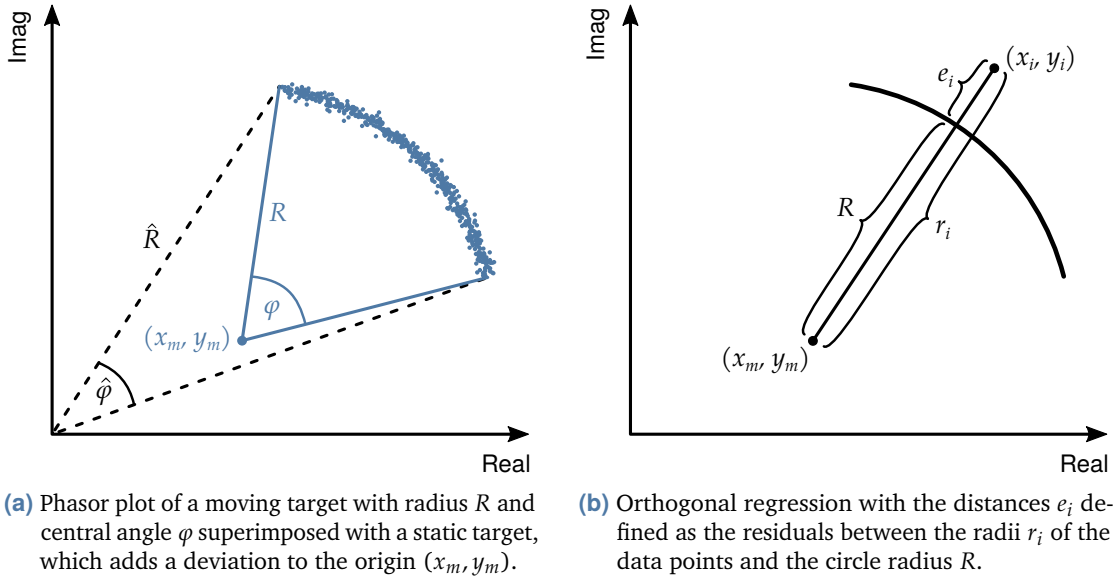


Figure 3.2: Simulation of the influence of static clutter. Adapted from [60].

Circle Fit Algorithms

Most of the commonly applied circle fitting algorithms use least squares approaches to determine the circle parameters. The non-linear circle equation

$$F(L, X) = (x - x_m)^2 + (y - y_m)^2 - R^2 = 0 \quad (3.1)$$

is a function of the measured values $L = (x, y)$ and the model parameters $X = (x_m, y_m, R)$ of the circle. Least squares minimises the error distances between the measured values and the parameters. The approaches differ with respect to the type of error distances that are minimised. In an algebraic fit, the error distances are derived from an implicit equation [16]. As this equation is linear, the fit is easy to compute but only delivers an approximation of the circle parameters. Alternatively, a geometric fit defines the error distances as the orthogonal distances from the measured values to the model [1]. The circle parameters are updated iteratively with a linearisation of the non-linear equations. Since the linearisation depends on approximate values for the first iteration, we combine both approaches.

First, the algebraic fit determines approximate values for the circle parameters. We introduce a substitution in Equation 3.1

$$x^2 + y^2 = 2x x_m + 2y y_m - x_m^2 - y_m^2 + R^2 \quad (3.2)$$

$$z = a x + b y + c \quad (3.3)$$

In this substitution, the measured values x and y are treated as constants, so that the function is linear and only depends on the substitute parameters a , b , and c , which are estimated in linear least squares. The origin and radius of the circle result from a resubstitution of these parameters.

In a second step, the geometric fit uses these approximate values to iteratively calculate the final circle parameters. The orthogonal distances are defined as the residuals ε between the radii r of the measured values and the circle radius R (see Figure 3.2b):

$$\varepsilon = R - r \quad (3.4)$$

As proposed by Niemeier [69], the radii of the points

$$r = \sqrt{(x - x_m)^2 + (y - y_m)^2} \quad (3.5)$$

are treated as measured values in Equation 3.4. This means that the function to be minimised is only dependent on the parameters. As the function is non-linear, the equations have to be linearised at the approximate values $\mathbf{X}^0 = (x_m^0, y_m^0, r^0)$ of the parameters

$$\left. \frac{\partial \varepsilon}{\partial x_m} \right|_{\mathbf{X}^0} = \frac{x - x_m^0}{r^0} \quad (3.6)$$

$$\left. \frac{\partial \varepsilon}{\partial y_m} \right|_{\mathbf{X}^0} = \frac{y - y_m^0}{r^0} \quad (3.7)$$

$$\left. \frac{\partial \varepsilon}{\partial R} \right|_{\mathbf{X}^0} = 1 \quad (3.8)$$

The measured values are reduced by the approximate circle radius R^0

$$l = r - R^0 \quad (3.9)$$

With the Jacobian matrix J containing the partial derivatives from Equations 3.6 to 3.8, the least squares is set up

$$l + \varepsilon = J \cdot \Delta \mathbf{X} \quad (3.10)$$

The solution $\Delta \mathbf{X}$ is updated iteratively with the approximate parameters \mathbf{X}^0 , until it converges.

Challenges in Circle Estimation

Successfully estimating the true origin of a circle or circular arc depends on several factors. The estimation is mainly influenced by

- the central angle of the circular arc,
- undetected disturbances,
- an unequal distribution of data points,
- and an inconsistent radius.

Most commonly, the size of the *central angle* negatively impacts the estimation. With a decreasing angle, the approximate radius from the algebraic fit is underestimated, which can cause the geometric fit to converge to a local minimum. The size of the angle depends on the displacement range measured in LOS. Usually, the displacement range scales with the bridge size, hence small bridges are more susceptible to estimation errors from this influence.

Although most *disturbances* should be detected by the algorithms proposed in Section 3.1.1, the influence of remaining disturbances can still be relevant. The disturbances act as outliers to the circle estimation, since not only the phase but also the amplitude varies during a disturbance. While an outlier detection or a robust modification of the circle estimation is possible, a reduction of their occurrence or an improvement of the removal process is an easier approach to address outliers.

In the case of low traffic volume, the *distribution of the data points* is skewed within the circular arc. A high concentration of data points forms around the (arbitrarily defined) zero phase, leading to a poor fit at the outer points of the arc. Usually, the radius is underestimated. This effect can be reduced by introducing a weight matrix W in Equation 3.10 of the geometric fit

$$l + \varepsilon = J \cdot W \cdot \Delta X \quad (3.11)$$

The diagonal of the weight matrix contains the absolute phase value for every data point, leading to a higher weight for the outer points of the arc than the points near zero phase.

Lastly, varying reflection of the targets causes a change in the received amplitude, which consequently leads to an *inconsistent radius* of the circle. For example, reflectors or reflective features may experience a significant rotation or deformation due to the displacement of a vehicle crossing. In the best case, the relationship between radius and

phase is still a function with a well-defined origin. However, this function is usually not apparent and cannot be easily estimated.

All influences to the circle estimation share the same result. If the estimated origin deviates from the true origin, a systematic deviation in the resulting displacement measurement is introduced. This deviation often has the form of a scaling error.

3.1.3 Atmospheric Influence

Changes in the atmospheric refractive index can have severe effects on microwave measurements. The propagation delay in microwaves leads to an additive term in the interferometric phase measurement [49]. This additive term is the atmospheric phase

$$\phi_{\text{atmo}} = \frac{4\pi}{\lambda} \cdot d \cdot \Delta n \quad (3.12)$$

which depends on the distance d to the target and the change in the refractive index Δn . A correction of the atmospheric phase is especially important for longer measurement durations and can be achieved with different methods. One approach is to calculate the refractive index with empiric formulas and measured atmospheric properties; most importantly, humidity and temperature [90]. For this, the atmospheric properties need to be mostly homogeneous on the whole measurement path, which can only be reasonably assumed for distances less than a couple of hundred metres.

A second approach uses a stable measurement target for the correction of the atmospheric phase. If the displacement of this target is zero, the measured phase can be wholly attributed to changes in the atmospheric properties (and sensor noise) [86]. The phase of this stable target then reduces the other target's phase. To keep the influence of noise and the inhomogeneity of the atmosphere low, the stable target should have an SNR that is equal to or higher than the other targets and should be in close proximity to them.

We propose a third approach, which relies on post-processing of the displacement measurements. This can be applied if certain conditions are met: the traffic intensity is low, so that, in a given time frame, the duration of vehicle crossings is shorter than the duration of no crossings. Additionally, the duration of a vehicle crossing should only be a few seconds. Assuming that the atmospheric properties are only changing slowly, the atmospheric phase can be removed by subtracting a moving median of the displacement measurements. With a window length of 15 s to 60 s, the long-wave atmospheric phase is removed without influencing the measurements of the vehicle crossings.

3.1.4 Three-Dimensional Projection

Since the GBR always measures displacements in LOS, a projection to a Cartesian coordinate system is needed to generate comparable results between different measurement setups. Additionally, the measurements in LOS may contain displacement components from more than one bridge axis. In general, bridges have the highest displacement amplitude in the vertical axis. Displacements in the direction of the transversal or longitudinal axis are smaller, but can still influence the measurement in the vertical axis depending on the setup [20]. By using more than one GBR simultaneously, it is possible to separate the displacement components for different axes. The projection is based on a principle first described by Mecatti et al. [53] and generalised by Li et al. [45], who define a transformation of displacements measured in LOS to a three-dimensional displacement vector in a Cartesian coordinate system. At first, the principle is defined in generic terms with an arbitrary number of GBRs, followed by a practise-orientated simplification to two or three GBRs.

The geometry of a measurement setup is characterised by the GBR coordinates $\mathbf{P}_i = [x_i, y_i, z_i]$ and the initial target coordinates $\mathbf{P}^0 = [x_T^0, y_T^0, z_T^0]$ (see Figure 3.3). While the target is displaced by a three-dimensional vector $\Delta\mathbf{P} = [\Delta x_T, \Delta y_T, \Delta z_T]$ to the new coordinates $\mathbf{P} = [x_T, y_T, z_T]$, the GBRs indirectly measure the displacement vector in their respective LOS with Δd . To derive a projection from Δd to $\Delta\mathbf{P}$, the distance

$$d_i = \sqrt{(x_i - x_T^0)^2 + (y_i - y_T^0)^2 + (z_i - z_T^0)^2} \quad (3.13)$$

between the i -th GBR and the target is linearised since the target's displacements can be considered differential. The distances d at the new target coordinates \mathbf{P} are approximated with the linearisation of the distances at the initial target coordinates \mathbf{P}^0 :

$$d(\mathbf{P}) \approx d(\mathbf{P}^0) + \left. \frac{\partial d}{\partial \mathbf{P}} \right|_{\mathbf{P}=\mathbf{P}^0} \cdot (\mathbf{P} - \mathbf{P}^0) \quad (3.14)$$

$$d(\mathbf{P}) - d(\mathbf{P}^0) = \left. \frac{\partial d}{\partial \mathbf{P}} \right|_{\mathbf{P}=\mathbf{P}^0} \cdot (\mathbf{P} - \mathbf{P}^0) \quad (3.15)$$

Subtracting $d(\mathbf{P}^0)$ from $d(\mathbf{P})$ results in the displacements in LOS Δd . Similarly, the difference between the new target coordinates \mathbf{P} and the initial target coordinates \mathbf{P}^0 results in the three-dimensional displacement vector $\Delta\mathbf{P}$. By combining the partial derivatives with the Jacobian matrix \mathbf{J} , the projection is written as

$$\Delta d = \mathbf{J} \cdot \Delta\mathbf{P} \quad (3.16)$$

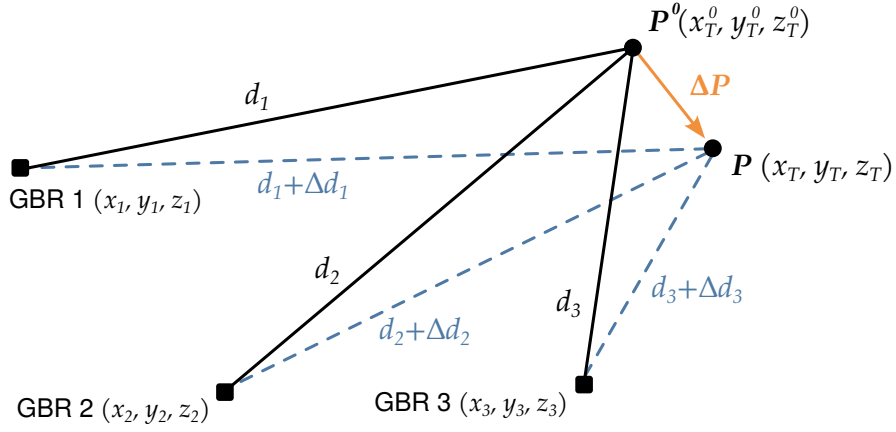


Figure 3.3: Schema of GBR and target geometry for the transformation of displacements in LOS Δd to displacements in a Cartesian coordinate system ΔP . Adapted from [60].

The target displacements in the Cartesian coordinate system result from the weighted least squares solution

$$\Delta P = (J^T W J)^{-1} \cdot J^T W \Delta d \quad (3.17)$$

which additionally considers the measurement uncertainties in the weight matrix W . If only three GBRs are used, the projection can be simplified to the inversion of the Jacobian matrix:

$$\Delta P = J^{-1} \cdot \Delta d \quad (3.18)$$

Although it is not possible to determine all three components of the displacement vector with less than three GBRs, the projection can still be used in this case. However, it has to be assumed that the displacement in one (or two) coordinate axes is zero. The Jacobian matrix is then modified to exclude the corresponding lines and columns to these axes, which enables the inversion.

3.1.5 Influence of the Processing on Measurement Uncertainty

A first estimate of the measurement uncertainty results from the SNR of the amplitude, as discussed in Section 2.1.2. This estimate includes all disturbances, clutter, and other influences on the displacement measurement. Thus, the uncertainty has to be assessed during processing to account for the removal of these influences. Most processing steps directly change the amplitude and consequently the SNR, which necessitates a recalculation of the uncertainty. Other steps also incorporate external uncertainties, such

as the measurement geometry of the projection, which requires a propagation of the uncertainty.

The disturbance removal leads to the first recalculation since the variance of the amplitude is decreased. A decreasing variance results in a higher SNR because the mean value is constant. Therefore, removing disturbances always decreases the uncertainty. In contrast, clutter removal can positively or negatively affect the mean value of the amplitude, depending on the phase value of static clutter in relation to the phase values of actual displacements. Besides, clutter removal also introduces additional uncertainties. For example, unreliable approximate values for the parameters can lead to the circle estimation converging to a local minimum instead of the global minimum. While these cases could be detected by a test for goodness of fit, an assessment of the estimation's accuracy is not possible. Therefore, estimation results with a bad fit would have to be discarded, and the influence on the uncertainty could not be evaluated.

The influence of the atmospheric correction depends on the applied approach and is generally challenging to estimate. If measurements of the atmospheric properties are used to calculate changes in the refractive index, the uncertainty of these measurements can be propagated to the displacements [84]. However, systematic deviations in the measurements or local disturbances of the atmospheric properties are not considered and the resulting uncertainty could be significantly underestimated. Similarly, the propagated uncertainty of a stable reference target may not be representative of the actual atmospheric influence at each target. In the case of the post-processing approach, an uncertainty propagation is unnecessary for measurements of dynamic loads since only the slowly changing influence is removed.

Lastly, the measurement geometry has a significant influence on the projection and the uncertainty of the resulting displacements. This influence can be separated into two components: the propagation of measurement uncertainty depending on the GBR and target geometry and the uncertainty of the geometry itself.

First, the propagation is considered in the generic case with an arbitrary number of GBRs. The weight matrix W contains the measurement uncertainties $\sigma_{\Delta d}$:

$$\Sigma_{\Delta d} = \sigma_{\Delta d} \cdot I \quad (3.19)$$

$$W = \Sigma_{\Delta d}^{-1} \quad (3.20)$$

With the a posteriori variance factor $\hat{\sigma}_0^2$ and the Jacobian matrix, the uncertainties are propagated

$$\Sigma_{\Delta P} = \hat{\sigma}_0^2 \cdot (J^T W J)^{-1} \quad (3.21)$$

resulting in the projected uncertainties $\Sigma_{\Delta P}$. The variance factor is determined with the residuals ε and the degree of freedom ν :

$$\hat{\sigma}_0^2 = \frac{\varepsilon^T W \varepsilon}{\nu} \quad (3.22)$$

In the simplified projection with three GBRs, the uncertainties are directly propagated with the Jacobian matrix.

$$\Sigma_{\Delta P} = J^{-1} \Sigma_{\Delta d} J^{-1T} \quad (3.23)$$

Similarly to the projection itself, the Jacobian matrix has to be modified to enable the inversion if less than three GBRs are used.

Besides the measurement uncertainty, a Monte Carlo simulation can additionally consider the influence of the uncertainty in the measurement geometry. For well-known targets, this influence is small compared to the measurement uncertainty. However, it can become significant if the target cannot be clearly identified or localised. A Monte Carlo simulation determines the probabilistic output of a function by repeated random sampling of its inputs. These inputs are usually modelled with normal distributions, which are defined by the inputs' mean and standard deviation. In the case of the three-dimensional projection, the input variables are the measurement uncertainty $\sigma_{\Delta d}$ and the coordinate uncertainty σ_{coord} . Therefore, the distributions are defined with standard deviations corresponding to the uncertainty values and means corresponding to known coordinates and displacements. The simulation repeatedly calculates the projection to determine an output distribution. Consequently, the uncertainty of the projected displacements results from the standard deviation of this distribution.

While the propagation of the measurement uncertainty can be fully replaced by the Monte Carlo simulation, it can still be used if the coordinate uncertainty is negligible. The Monte Carlo simulation requires repeated calculations with thousands of samples, and thus has a large computational disadvantage compared to a simple propagation.

3.2 Results

Measurement campaigns at two bridges are required for a comprehensive evaluation of the proposed GBR processing steps, since not all steps are applicable for all bridges. For example, the disturbance detection is only necessary if the GBR signal crosses another road or foot path, where disturbances are expected. Additionally, there are varying challenges in processing for different measurement situations. The bridges in Schneckenlohe and Maxau cover these situations and allow a generalised discussion of the proposed methodology.

3.2.1 Measurement Setup

Schneckenlohe

Several measurement campaigns were carried out at the bridge in Schneckenlohe. In the following, the proposed processing is exemplarily applied to one measurement campaign on 22 October 2019. As discussed in Section 2.3.1, the bridge is a prestressed concrete structure with two T-beams. It is part of the federal road B 303 and crosses the district road KC 29. In addition to the primary displacement in the vertical axis, it is expected that a horizontal displacement component also exists. Therefore, the measurement setup shown in Figure 3.4 is chosen to determine the vertical component and the horizontal component orthogonal to the longitudinal bridge axis. This setup is a compromise to enable interference-free measurement between the two IBIS sensors, as discussed in Section 2.1.3. Ideally, GBR 1 would be placed orthogonally to the longitudinal axis opposite GBR 2. The influence of the third displacement component parallel to the longitudinal axis would be minimised, and the bridge beams could be used as reflectors for the GBR signal. For the proposed setup, additional reflectors for GBR 1 are necessary to ensure sufficient signal reflection. The reflectors, subsequently referred to as Target 1 and 2, are installed at the centre of each beam, where the longitudinal displacement component is assumed to be insignificant. Both GBRs achieve an average SNR of 26 dB to 30 dB for both targets, resulting in a displacement uncertainty of 0.04 mm to 0.07 mm.

Maxau

Measurements at the railway bridge at Maxau (near Karlsruhe, Germany) were carried out on 6 July 2022 and 9 August 2022. While both campaigns use the same measurement setup for the GBRs, the second campaign additionally applies two TLS to provide

reference measurements. The bridge at Maxau consists of two independent steel truss structures with two fields, as discussed in Section 2.3.2. Figure 3.5 shows the measurement setup at the eastern field, which has a length of 117 m. Since the railway track is centred on the bridge deck and completely straight, no significant orthogonal displacement component is expected. Therefore, the GBRs are both positioned in line with the longitudinal axis to determine the vertical and longitudinal displacement components. Interference between the GBRs is not an issue because the two FastGBSAR sensors are synchronised by a GNSS time signal, as discussed in Section 2.1.3. The orthogonal trusses on the underside of the bridge are ideal features for signal reflection. In addition, their distance from each other is approximately 3 m. Thus, they can be clearly identified with the typical range resolution of 0.75 m. In the case of GBR 1, sufficient signal reflection is achieved for 12 trusses, whereas GBR 2 receives signals for 11 trusses. Sufficient signal reflection is defined as an SNR greater than 20 dB, which results in a displacement uncertainty of 0.1 mm. Since the signal footprint is not exactly equal, 9 trusses are observed by both sensors, covering approximately 20 % of the total bridge length.

Two TLS in profile mode provide reference measurements for the validation of the GBRs and the proposed processing steps. The first TLS (Z+F 9012) is positioned near GBR 1 measuring the vertical displacement of the southern longitudinal truss. A second TLS (Z+F 5016) is positioned near GBR 2 measuring the horizontal displacement of several orthogonal trusses. Both laser profiles cover a large part of the bridge field, as shown in Figure 3.5. While it would be possible to determine horizontal and vertical displacements from a single TLS, the described setup achieves higher accuracy because of favourable incidence angles in a larger area. The following analysis mainly focuses on one of the orthogonal trusses, which is called Target 1. It is located at 34 m from the eastern bridge pillar, which is approximately a third of the total length of the bridge field. However, the results are representative for most other trusses as well.

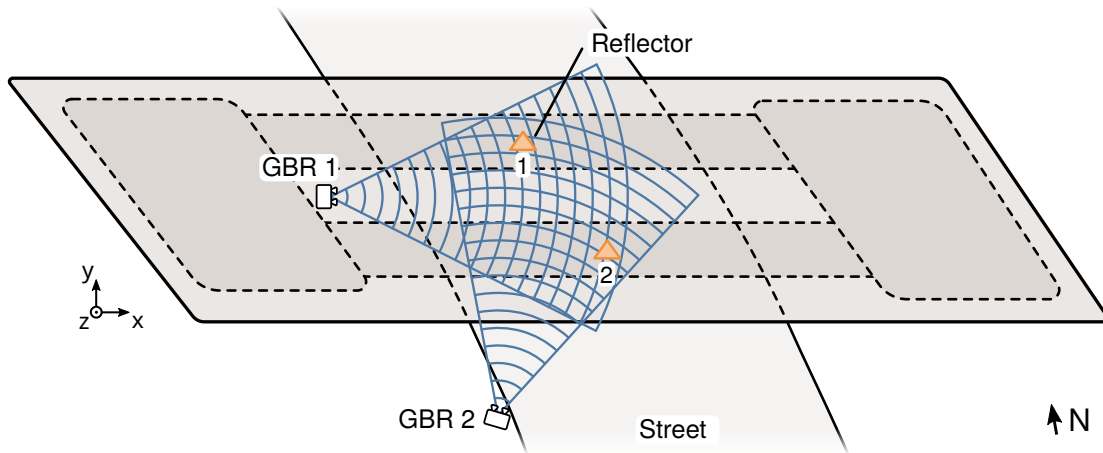
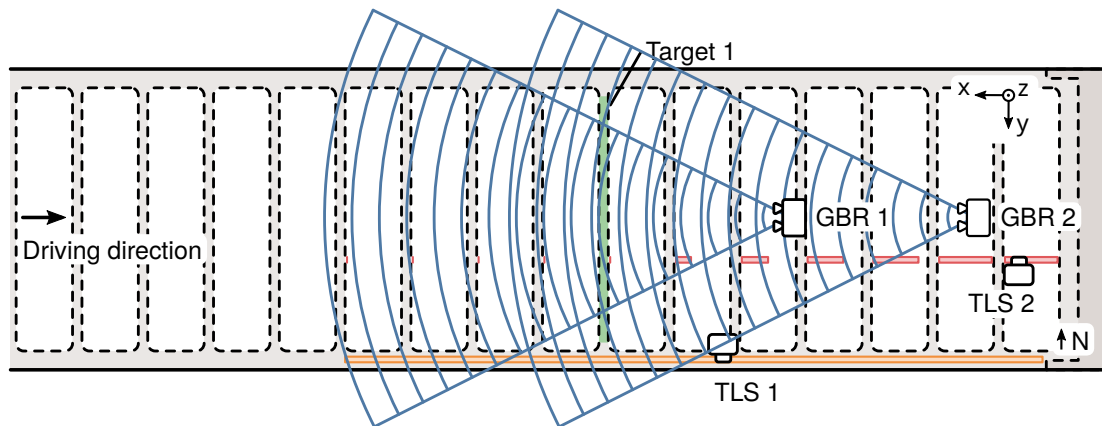
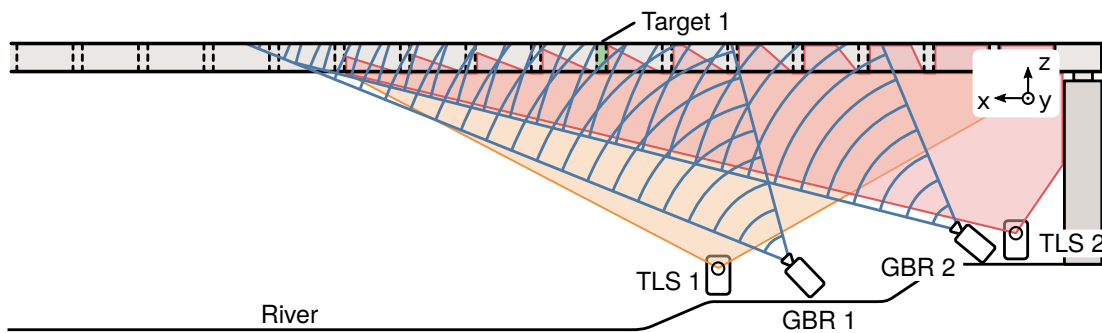


Figure 3.4: Measurement setup at the road bridge in Schneckenlohe.



(a) Top view.



(b) Side view.

Figure 3.5: Measurement setup with the field of view for two GBR and two TLS at the railway bridge over the river Rhine at Maxau. The illustration is not to scale. Target 1 is located at 34 m from the eastern bridge pillar, which is approximately a third of the bridge field's total length.

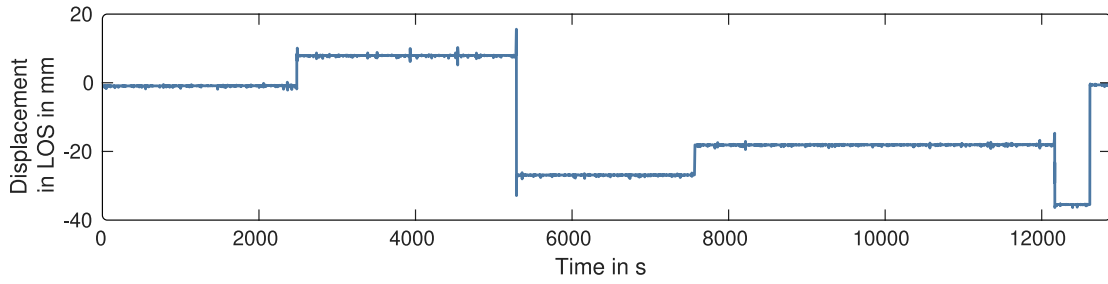
3.2.2 Removal of Disturbances

The detection of disturbances is irrelevant for the measurements at Maxau since the signal paths are directed away from vehicles and people. In Schneckenlohe, however, there is no possible measurement setup to avoid disturbances from vehicles on the district road. Most of the vehicles passing through the GBR signal cause broadband noise. However, large vehicles like trucks additionally lead to phase jumps because of unwrapping errors. Therefore, the following results focus on the measurements in Schneckenlohe.

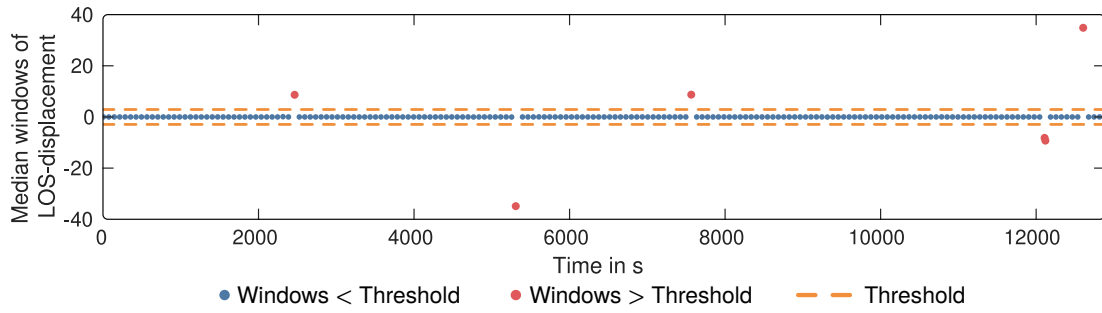
Figure 3.6a exemplarily shows these jumps for the displacements of Target 1 measured by GBR 1. During the 3.5 h long measurement, five jumps are identified by the significant shift in the mean displacement. Median windows with a window size of 10 s are calculated from the displacements and differenced ones. A threshold determined by the standard deviation of the resulting values correctly detects all jumps, as shown in Figure 3.6b.

Broadband noise is shown exemplarily in Figure 3.7a for a segment of the displacements at Target 1 measured by GBR 1. Four disturbances are visible between 40 s and 55 s. The segment also contains displacements from several vehicle crossings, one of which is interrupted by the last disturbance. Since the displacements from vehicles consist mainly of low-frequency components below 10 Hz, the broadband noise disturbances are easily separated by a high-pass filter with a corresponding cut-off frequency. Figure 3.7b shows the filtered displacements only containing disturbances. A threshold calculated from the standard deviation of the filtered displacements correctly detects all disturbances.

Besides this small segment, the detection accuracy of the proposed algorithm is evaluated for the entire measurement campaign. An accurate ground truth is generated by manually labelling all disturbances. The resulting precision and recall values are shown in Table 3.1 for both GBRs and targets. In each case, approximately 240 disturbances are detected during the 3.5 h long measurement since the primary source of disturbances, the district road, is equal for all measurements. The high recall values above 99 % indicate that almost all disturbances are identified by the proposed algorithm. Precision values ranging from 94 % to 98 % suggest that some additional disturbances are detected, which are not present in the manually labelled ground truth.

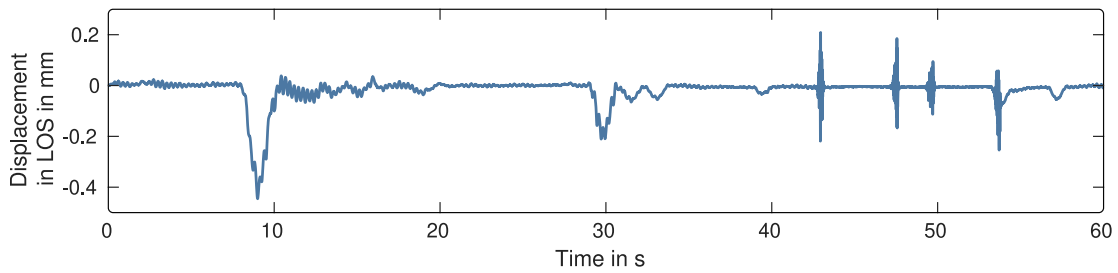


(a) Raw displacements in LOS.

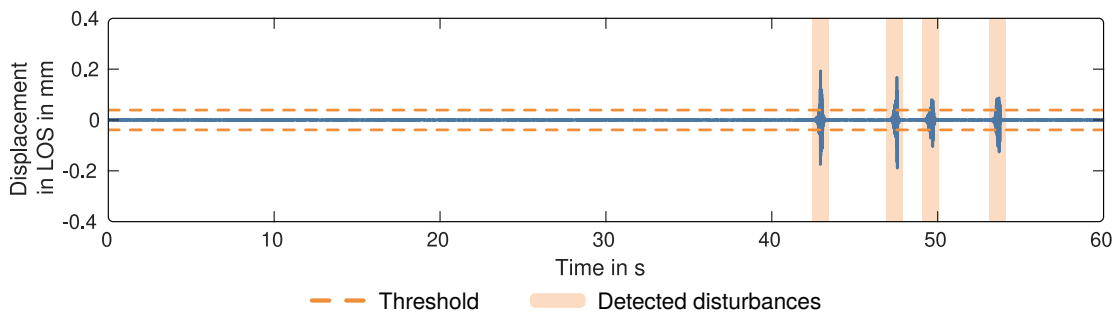


(b) Differenced median windows calculated from the raw displacements in LOS.

Figure 3.6: Detection of phase jumps in the raw displacements measured by GBR 1 at Target 1 in Schneckenlohe. Reprinted from [60].



(a) Segment of the raw displacements in LOS.



(b) High pass filtered segment of the raw displacements in LOS.

Figure 3.7: Detection of broadband noise for a segment of the raw displacements measured by GBR 1 at Target 1 in Schneckenlohe.

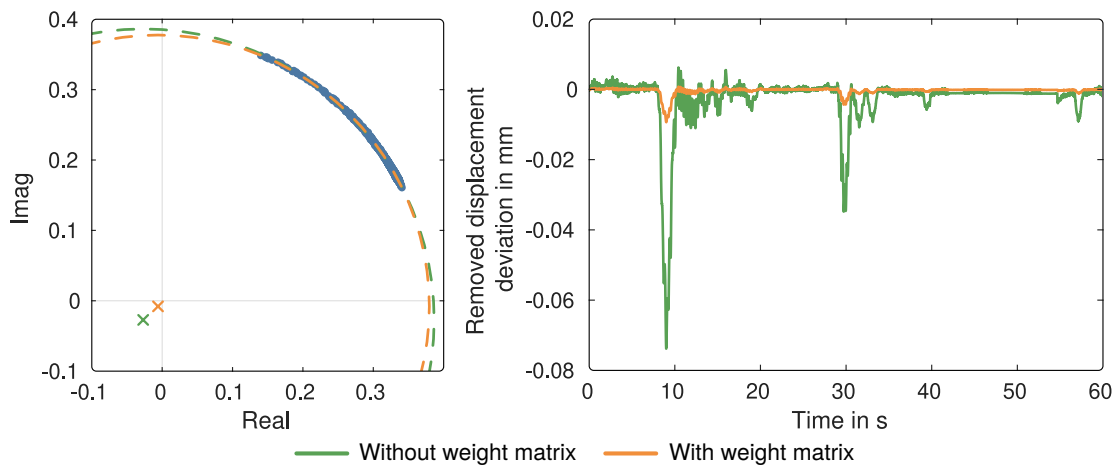
Table 3.1: Accuracy of the disturbance detection in Schneckelohe. Adapted from [60]

GBR	Target	Number of disturbances	Precision	Recall
GBR 1	Target 1	239	94.0 %	99.2 %
GBR 1	Target 2	235	97.8 %	99.6 %
GBR 2	Target 1	232	96.5 %	99.1 %
GBR 2	Target 2	249	97.6 %	100.0 %

3.2.3 Clutter Removal

Successfully removing static clutter highly depends on the measurement setup and the observed structure. The following results show different aspects and challenges of the clutter estimation for the two bridges in Schneckelohe and Maxau.

For Schneckelohe, the phasor plot of the complex-valued IQ components exhibits a small circular arc, as shown in Figure 3.8a. The least squares algorithm estimates the circle's radius and centre with and without the proposed weight matrix. Both results show a small deviation of the circle centre from the origin. Subtracting the estimated centre from the IQ components removes the static clutter. Figure 3.8b shows the deviation caused by static clutter for a segment of the measurements. The removed deviation is proportional to the displacements in LOS for both the results with and without a weight matrix. However, there is about an order of magnitude difference between the two results.



(a) Phasor plot of IQ components and estimated circles. (b) Displacement deviation caused by static clutter.

Figure 3.8: Clutter removal for a segment of the displacements measured by GBR 1 at Target 1 in Schneckelohe.

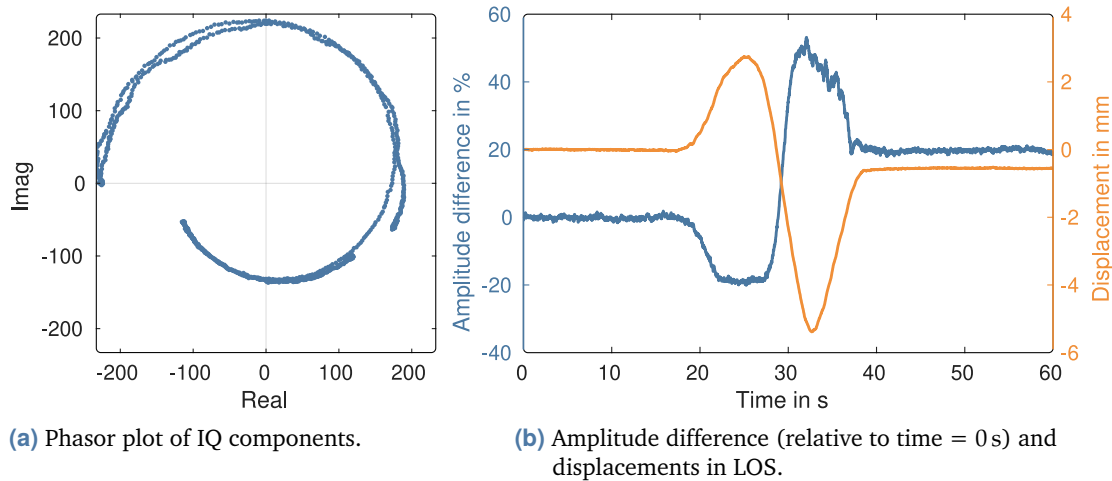


Figure 3.9: Relationship between displacement and amplitude, and their impact on clutter estimation at Maxau.

The measurements at Maxau exhibit different challenges to the circle estimation. Figure 3.9a exemplarily shows the phasor plot of Target 1 during a train crossing. While the circular arc almost forms a full circle, the radius increases with the central angle. The increase can also be indirectly observed by the difference in amplitude in Figure 3.9b. Relative to the beginning of the measurement, the amplitude decreases and increases inversely proportional to the displacement. A difference of up to 50 % occurs during the maximum negative displacement. Furthermore, a residual difference of 20 % permanently remains after the train crossing. The varying amplitude likely results from changing reflective properties of the bridge truss, which could be caused by small rotations or deformations. Estimating the centre is not possible for this particular measurement.

The example shown for Maxau is an uncommon but not unlikely case. For example, Section 3.2.5 shows a systematic deviation of the vertical displacements to a reference sensor, which is likely caused by an imperfect clutter estimation. In general, other train crossings and other targets exhibit a more typical behaviour, where the circle estimation is successful. Further analysis estimates circles for all 25 train crossings and 9 targets separately. The resulting circle centres are evaluated with regard to their Euclidean distance to the origin. Figure 3.10 shows the ratio of this distance to the estimated circle radius as a function of the radius. Generally speaking, the radius is equal to the amplitude of the received signal, hence a greater radius corresponds to a higher SNR. In other words, the analysis shows the ratio of static clutter in each measurement as a function of the received signal amplitude. The clutter ratio increases with smaller radii (and lower SNR). Additionally, the variation of the clutter ratio increases with smaller radii because of the influence of increased noise and other disturbances on the circle estimation.

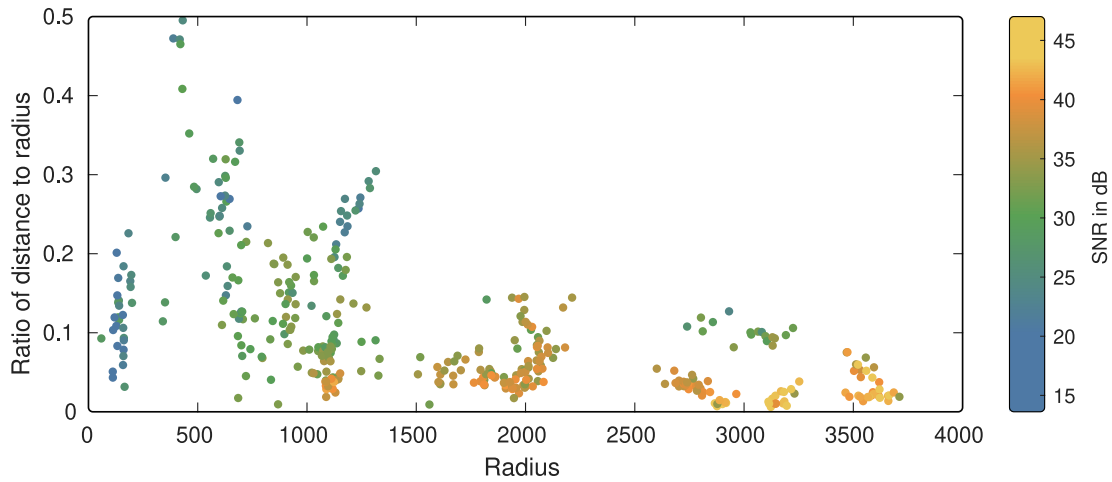


Figure 3.10: Ratio of the circle centre’s distance from the origin to the circle’s radius. The ratio is shown as a function of the circle’s radius and coloured according to the SNR of the corresponding displacement segments measured at Maxau.

The cause of an increasing clutter ratio is most likely an insufficient side lobe suppression of the applied window, which could allow significant interference between different range cells. To further analyse this interference and its influence on the resulting displacements, the clutter estimation is performed for measurements obtained with a different window function. In addition to the default Kaiser window ($\beta = 4$), the measurements are processed with a Blackman window, which has higher side lobe suppression (see also Figure 2.2). Similar to the previous analysis, the Euclidean distances of the circle centres to the origin are calculated as a function of the radius. However, instead of the ordinary distance, Figure 3.11 shows the difference between the distances obtained from the two window functions. The distances of the Blackman window are subtracted from the distances obtained with the Kaiser window. For large radii, the difference is approximately zero. Smaller radii and lower SNR lead to an increasing absolute difference. Since positive as well as negative values are shown, it cannot generally be concluded that the Blackman window suppresses static clutter. However, the large influence of the window function is apparent, which is further discussed in Section 3.3.

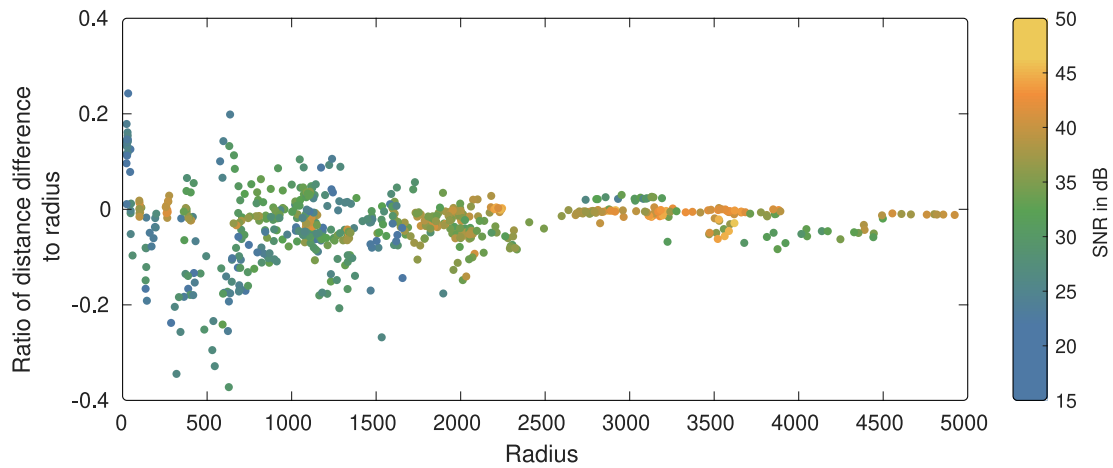


Figure 3.11: Ratio of the difference between the circle centre’s distances from the origin to the circle’s radius. The difference is the results of the Blackman window subtracted from the results of the Kaiser window. The ratio is shown as a function of the circle’s radius and coloured according to the SNR of the corresponding displacement segments measured at Maxau.

3.2.4 Atmospheric Influence

After removing disturbances and clutter, the displacements still contain a long-term non-linear drift caused by changes in the atmospheric refractive index. Two sensors measure the atmospheric properties to model the refractive index and remove the drift for the measurements in Schneckenlohe. The first sensor is placed near the GBR and measures temperature and humidity. The second sensor is installed at the bridge and measures temperature. Figure 3.12a shows an increase in humidity by approximately 7 percentage points. The temperature differs considerably between the two sensors. While only a slight variation is measured at the sensor near the GBR, the bridge’s sensor shows an increase by about 3°C followed with a slow decrease by 2°C . Using a mean of these measurements to model the atmospheric phase only partially corrects the drift. The displacements shown in Figure 3.12b are filtered by a moving median with a window size of 60 s to better compare the results. The drift is successfully removed in the first hour of the measurements but is not correctly modelled for the remaining measurement time. Removing the remaining drift is possible by the proposed post-processing approach. In the case of Schneckenlohe, a moving median with a window size of 30 s is used, while for the measurements at Maxau a window size of 1 min to 2 min is required because of the longer crossing durations of the train.

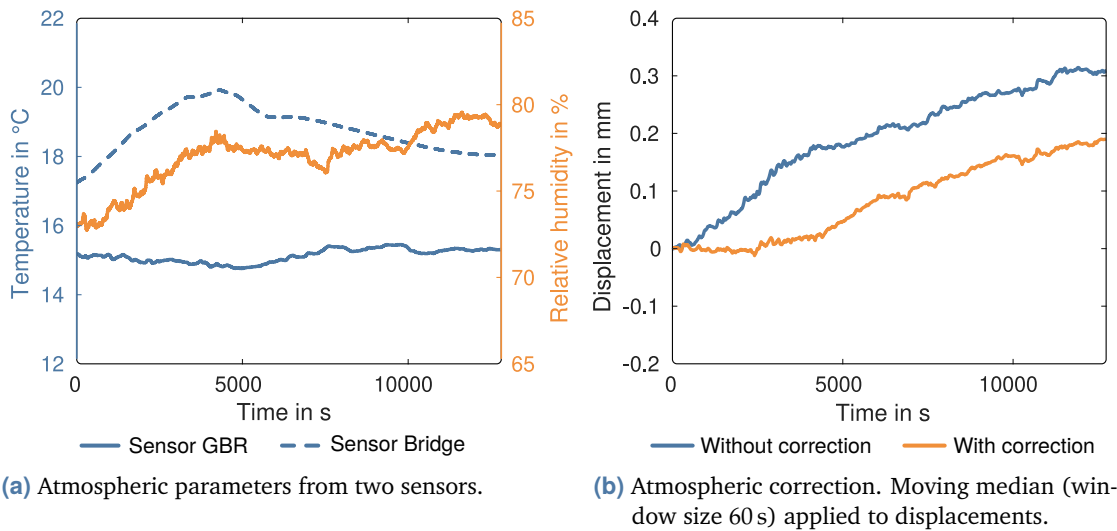
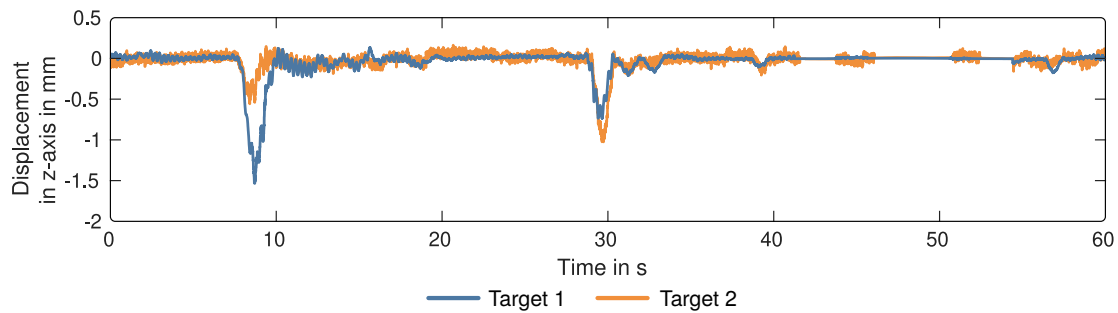


Figure 3.12: Atmospheric correction of the displacements measured by GBR 1 at Target 1 in Schneckenlohe.

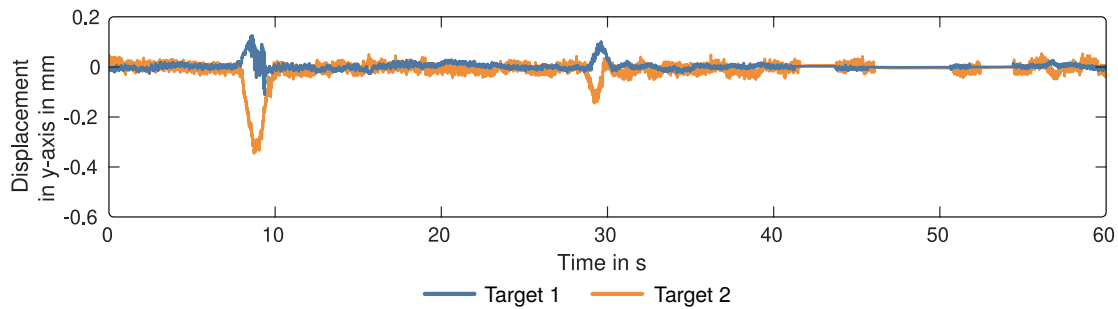
3.2.5 Two-Dimensional Projection

For most bridges and also the studied bridge in Schneckenlohe, it is reasonable to expect the highest displacement amplitude in the vertical axis. Figure 3.13a shows a segment of the vertical displacement for both targets in Schneckenlohe. For the first truck crossing at 9 s, the displacement of Target 1 is higher than the displacement of Target 2, suggesting a crossing in the northern lane. The second truck crossing at 30 s shows an inverted ratio, suggesting a crossing on the southern lane. However, the difference between the maximum displacement is less pronounced. Crossings of smaller vehicles are visible for Target 1, but mostly disappear in the noise of Target 2. Besides the vertical displacement, the measurement setup in Schneckenlohe also allows determining the horizontal displacement component orthogonal to the driving direction. Figure 3.13b shows significant displacements for the two truck crossings, although with smaller maximum values compared to the vertical axis. The displacements are positive for Target 1 and negative for Target 2, irrespective of the trucks' driving directions. Smaller vehicles show no discernible displacements in the horizontal axis.

The measurement campaign at Maxau allows determining displacements in the vertical axis and the horizontal axis parallel to the driving direction. Figure 3.14 shows the displacements caused by the crossing of a regional train (line RE6 of type BR642 with two carriages). The displacements in the vertical axis exhibit a characteristic behaviour for this type of crossing. At first, the displacement of the neighbouring bridge field lifts the observed field. When the train crosses the observed field, a maximum negative displacement of about 8 mm is measured, followed by a damped vibration with



(a) Displacement in z-axis.



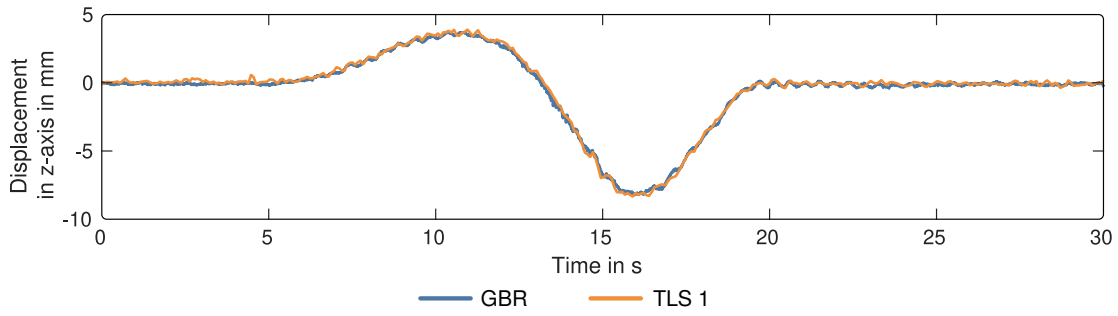
(b) Displacement in y-axis.

Figure 3.13: Segment of the projected displacements for both targets in Schneckenohe.

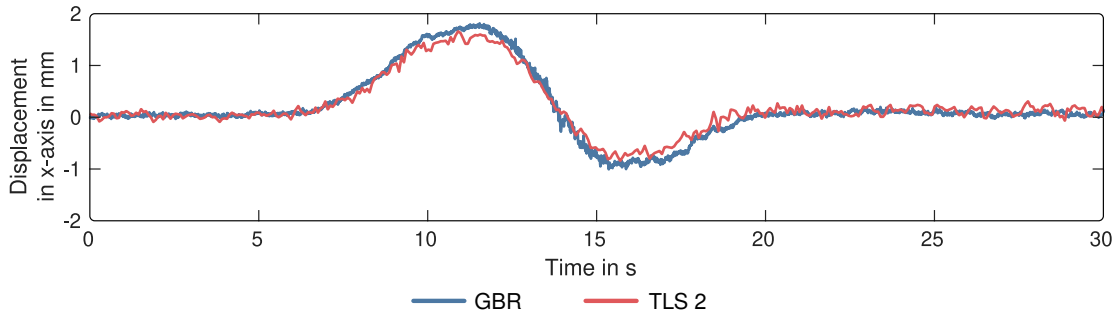
the bridge's eigenfrequency. The horizontal component shows a similar characteristic, although with smaller absolute values. Generally, the projected displacements of the GBR agree with the TLS measurements, as also shown by the displacement differences in Figure 3.15. In addition to a small deterministic component in the horizontal axis, the displacement differences mostly contain noise with standard deviations of about 0.15 mm. If the conventional one-dimensional projection is used instead, the differences are much higher. At the maximum horizontal displacement, the vertical displacement measured by GBR 1 is 78 % higher than the vertical displacement measured by TLS. For GBR 2, the difference is even higher with a systematic deviation of 173 % of the TLS displacement.

A second train crossing of the same regional train exhibits greater differences between the two sensor types. Figure 3.16 shows the projected displacements of GBR compared to the TLS measurements. While the vertical displacements are still highly correlated between the sensors, a scaling difference with its highest value during the crossing of the neighbouring bridge field can be observed. The horizontal displacements experience a proportionally higher difference and a lower correlation between the sensors. Since the measurement setup and the type of train have not changed between the two crossings, the difference likely originates from a processing step of the GBR measurements. Therefore, the two GBRs are separately evaluated to determine the cause of the difference. It

is not possible to apply a one-dimensional projection for this evaluation, since the horizontal component would lead to a significant systematic deviation, as discussed earlier. However, the TLS measurements can be used in a two-dimensional projection together with the individual GBRs. To determine vertical displacements, the horizontal displacement of TLS 2 is used together with the displacements in LOS of the GBRs. Horizontal displacements result from the vertical displacements of TLS 1 together with the displacements in LOS of the GBRs. Since the TLS does not measure displacements in LOS, a virtual position has to be modelled. This position assumes the z- and y-coordinates of the target and an arbitrary x-coordinate in the case of TLS 2. For TLS 1, the x- and y-coordinates of the target are used, while the z-coordinate is arbitrary. The results are shown in Figure 3.17. In the vertical axis, GBR 1 matches the TLS, whereas GBR 2 has a systematic deviation during the crossing of the neighbouring bridge field. The horizontal axis also sees small differences for both GBRs, although they are in the same order of magnitude as the noise of the displacements. Therefore, these differences likely result from a processing step specific to GBR 2. Further discussion on the cause is provided in Section 3.3.

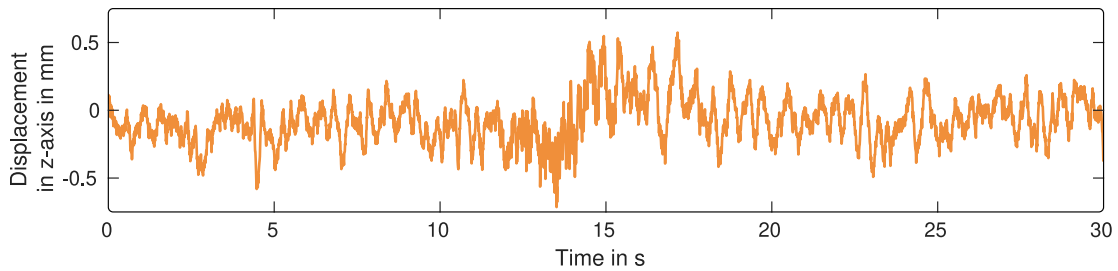


(a) Displacement in z-axis.

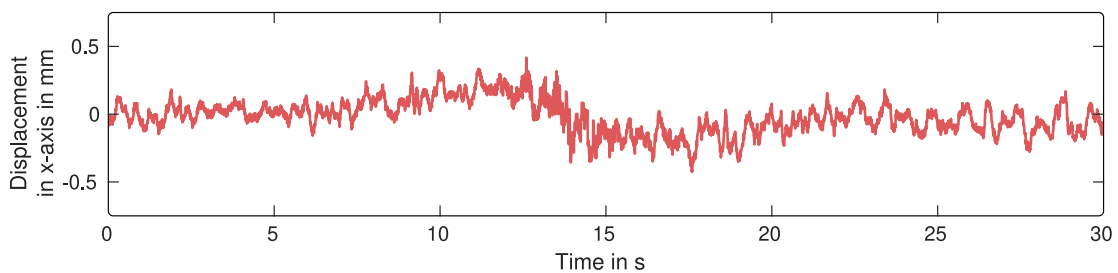


(b) Displacement in x-axis.

Figure 3.14: Projected displacements during the first train crossing at Maxau. Crossing of the RE 6 at 10:46.

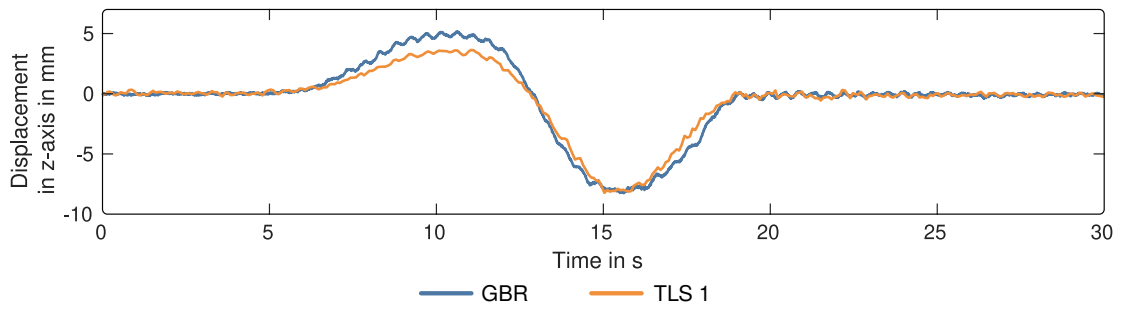


(a) Displacement difference to TLS 1 in z-axis.

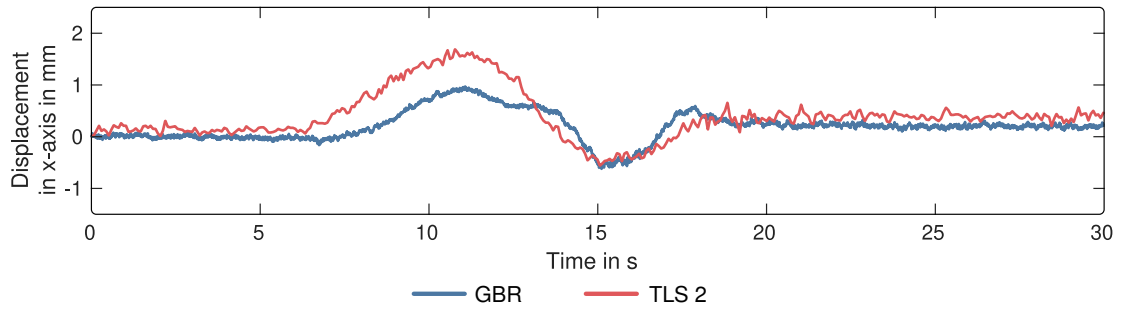


(b) Displacement difference to TLS 2 in x-axis.

Figure 3.15: Difference of the displacement measured by GBR to the displacement measured by TLS during the first train crossing at Maxau. Crossing of the RE 6 at 10:46.

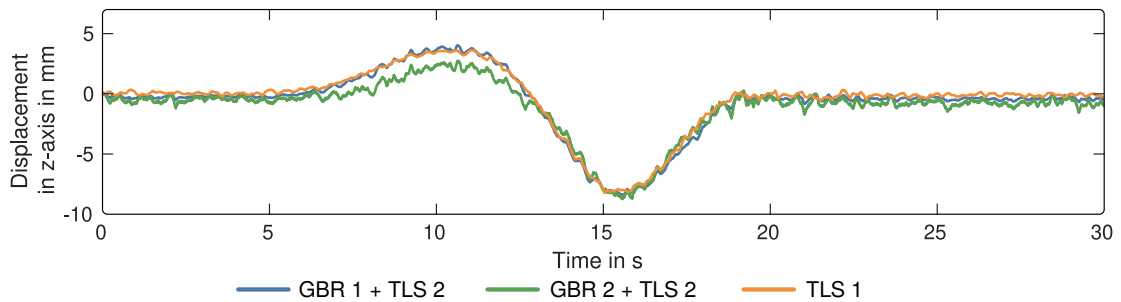


(a) Displacement in z-axis.

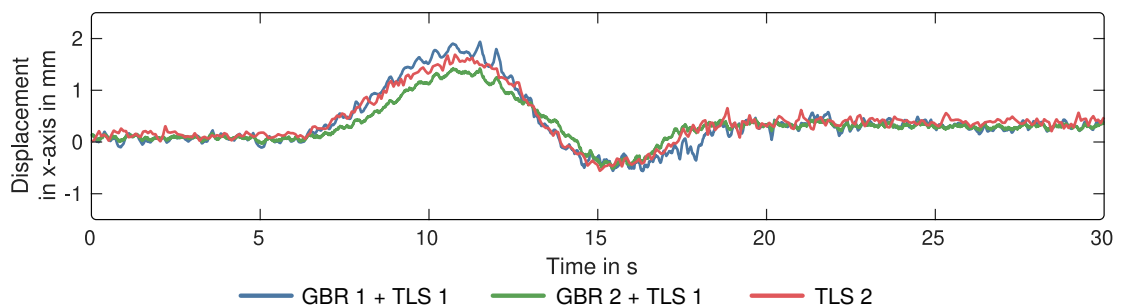


(b) Displacement in x-axis.

Figure 3.16: Projected displacements during the second train crossing at Maxau. Crossing of the RE 6 at 11:46.



(a) Displacement in z-axis.



(b) Displacement in x-axis.

Figure 3.17: Displacements in LOS projected with TLS measurements during the second train crossing at Maxau. Crossing of the RE 6 at 11:46.

3.2.6 Measurement Uncertainty

Every processing step influences the measurement uncertainty, either by directly changing the SNR or through propagation. Table 3.2 shows uncertainty estimates of the measurements in Schneckenlohe throughout the processing. The uncertainty of the displacements in LOS is estimated in a range of 0.02 mm to 0.14 mm for the two GBRs. After removal of the disturbances, the uncertainty estimates are decreased due to the reduced amplitude variance. Static clutter influences the amplitude mean, resulting in an uncertainty increase or decrease after its removal. In the case of Schneckenlohe, the uncertainty ranges between 0.02 mm and 0.03 mm after clutter removal, except for Target 1 measured by GBR 1, which has a significantly lower value. These values are propagated as discussed in Section 3.1.4, resulting in uncertainties of lower than 0.1 mm for the projected displacements in the y- and z-axis. An additionally applied coordinate uncertainty of 0.05 m only minimally influences these results and is not shown separately for this example.

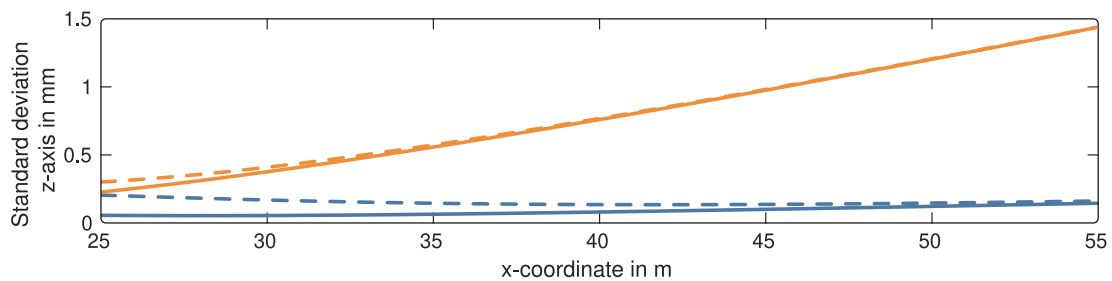
For the measurements at Maxau, the influence of the coordinate uncertainty is much more important, since larger trusses are used for signal reflection compared to the compact corner reflectors in Schneckenlohe. The influence is evaluated with Monte Carlo simulations with varying input distributions. The measurement uncertainty $\sigma_{\Delta d}$ as one input variable is modelled by a normal distribution with standard deviations of 0.01 mm and 0.1 mm. As a second input variable, the target coordinate uncertainty σ_{coord} is initially modelled with fixed values. In a second simulation, the uncertainty of the x-coordinate is modelled by a normal distribution with a standard deviation of 0.3 m, whereas the y- and z-coordinates are modelled with standard deviations of 0.5 m. The standard deviations for the measurement uncertainty represent typical values achievable in this measurement setup, while the standard deviations of the coordinate uncertainty cover the extreme values of no uncertainty and an uncertainty with the assumed size of the signal footprint of one range cell. Figure 3.18 shows the results of these four simulations for a longitudinal profile of the signal footprint on the bridge underside. Both axes exhibit a similar characteristic of the displacement uncertainty. However, the z-axis reaches higher values than the x-axis. In both cases, a higher measurement uncertainty directly leads to higher values after the projection. Overall, the uncertainty increases with the x-coordinate, whereas the influence of the additional coordinate uncertainty decreases.

Besides this simulation, the uncertainty can be estimated for the measurements shown in Section 3.2.5. For Target 1, both GBRs achieve a measurement uncertainty after clutter removal of about 0.04 mm. This value results in an uncertainty of the projected

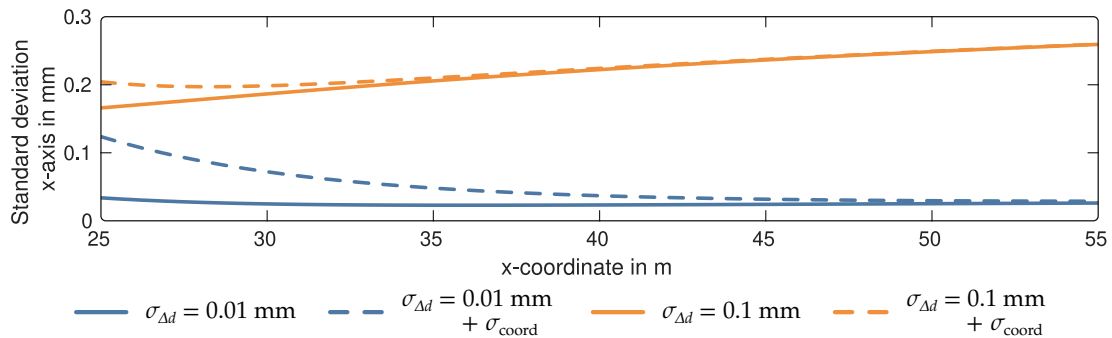
displacements of 0.22 mm for the z-axis and 0.08 mm for the x-axis. If the previously assumed coordinate uncertainty is added, the displacement uncertainty increases to 0.31 mm and 0.15 mm, respectively. The other 8 trusses achieve values in the same order of magnitude due to the preselection of targets based on a minimum SNR of 20 dB.

Table 3.2: Measurement uncertainty after each processing step for both targets in Schneckelohe. All values are in millimetre. Reprinted from [60].

Target	GBR	LOS	Disturbance removal	Clutter removal	Projection to y-axis	Projection to z-axis
Target 1	GBR 1	0.019	0.007	0.002	0.045	0.036
	GBR 2	0.034	0.005	0.033		
Target 2	GBR 1	0.142	0.027	0.027	0.036	0.095
	GBR 2	0.029	0.008	0.019		



(a) Uncertainty in z-axis.



(b) Uncertainty in x-axis.

Figure 3.18: Simulated uncertainty for the displacements in the z- and x-axis as a function of the bridge's x-coordinate at Maxau. The simulation has the measurement uncertainty $\sigma_{\Delta d}$ and the coordinate uncertainty σ_{coord} as input variables.

3.3 Discussion

This section discusses the results of the proposed processing steps for the measurement campaigns in Schneckelohe and Maxau, starting with the detection and removal of disturbances.

Disturbances In Schneckelohe, disturbances are mainly caused by vehicle traffic on the district road that crosses the GBR signal. In the case of large vehicles, such as trucks or buses, the disturbances lead to phase unwrapping errors, and consequently to phase jumps. The measurements in Schneckelohe show a small number of jumps, since only a few large vehicles cross the district road. Therefore, all jumps are correctly detected by the median windows. In the case of higher traffic volumes, the window length has to be reduced. The window length should generally be twice as long as a typical vehicle crossing over the observed bridge in order to limit the occurrence of false positives.

Smaller vehicles or people crossing the GBR signal cause disturbances in the form of broadband noise. These kind of disturbances are detected by applying a threshold to the high-pass filtered displacements. Even though the threshold is calculated iteratively from the displacement's standard deviation, a minimum detection level depending on the noise is still present. This level is adjusted to ensure high precision and recall values, with a favour to the recall values. It is preferred to have a higher number of false positives than false negatives since the subsequent processing steps, such as clutter removal and uncertainty estimation, rely on measurements without disturbances or other kind of outliers.

Clutter Removal Static clutter is removed from the complex-valued IQ components by a circle estimation. The two measurement campaigns in Schneckelohe and Maxau provide different challenges for this estimation. In the case of Schneckelohe, the main challenge is the unequal distribution of data points, which is addressed with the proposed weight matrix. The unequal distribution is caused by a relatively low traffic volume, especially for heavy vehicles. In addition, the displacements and consequently the circular arc are small, leading to a significant uncertainty in the estimation. The measurements at Maxau show two challenges. First, the amplitude is sometimes correlated with the displacement, preventing a successful estimation of the circle centre. The correlation is likely caused by the significant horizontal displacement, which may lead to small rotations of the bridge truss. Alternatively, small deformations of the truss are also possible. Both effects would lead to changes in the reflective properties and consequently in the received signal

amplitude. It could still be possible to estimate the centre with an adapted mathematical model. However, the model would have to be changed based on the measured horizontal displacement specific to the evaluated target and train crossing.

The second challenge at Maxau is the increasing influence of clutter for targets with lower SNR. It is unlikely that other objects are located in the same range cells as the observed targets, especially for GBR1 with an unobstructed signal path over the river. Static clutter is probably caused by large objects, e.g. the bridge's pillar, for all range cells. Before transforming the IQ components from the frequency-time domain to the range-time domain, a window is applied (see Section 2.1.1). With limited damping by the window's side lobes, the signal amplitude of a large object is insufficiently focused to one range cell. Thus, the influence of clutter depends on the proximity to this cell, the damping of the window's side lobes, and most importantly the signal amplitude. Range cells with lower signal amplitudes see an increased clutter influence. However, it cannot generally be assumed that a window function with higher side lobe attenuation decreases static clutter. Applying a Blackman window has increased as well as decreased the occurrence of clutter for low signal amplitudes. At the same time, the Blackman window also decreases the signal amplitude of the observed range cell, which could mask the effect of static clutter. From this analysis, it can only be concluded that the window function has a large influence on measurements with low signal amplitude, especially if the clutter estimation is omitted.

To summarise, clutter removal becomes more important for range cells with lower signal amplitude because the ratio of clutter to actual displacement increases. Additionally, range cells with low signal amplitude have higher noise levels, resulting in higher uncertainties for the circle estimation. Clutter can significantly influence the measurement, and the benefit of its removal must be weighed against the uncertainty introduced by the circle estimation. This uncertainty generally increases with the importance of clutter removal.

Atmospheric Influence Estimating the atmospheric influence by measuring temperature and humidity is only partially successful for the measurements in Schneckelohe. The difference between the two temperature sensors demonstrates the difficulty of estimating a refractive index for the entire signal path. Selective measurements of the inhomogeneous properties cannot accurately determine the atmospheric phase even for such a short range of 15 m. Additionally, the accuracy of the applied atmospheric sensors might not be sufficient, further increasing the uncertainty in the estimation of the refractive index. A stable reference target would experience the same problem since it may not be representative for all other targets due to the inhomogeneity of the atmosphere. However,

dynamic displacements caused by vehicle crossings usually have a short duration of 2 s to 10 s. In comparison, atmospheric properties generally change slowly. Thus, the post-processing approach is a valid alternative for these kind of measurements.

Projection The application of the proposed two-dimensional projection has different primary objectives for the bridges in Schneckelohe and Maxau. In Schneckelohe, the primary objective is the determination of a second displacement component, while the measurements at Maxau most importantly show the eliminated influence of this component on the vertical displacement. This influence will result in significant systematic deviations if a one-dimensional projection is applied to the displacements in LOS. However, scaling differences to the TLS reference still exist even with the two-dimensional projection. In the case of the first train crossing, the differences are within the range of the estimated uncertainties for both sensor types. The second train crossing shows differences beyond this range even though the measurement setup was not changed. With the combined GBR and TLS approach, the cause of these differences is identified as GBR 2. There is most likely a scaling error introduced in the clutter removal step, which does not correctly estimate the circle centre for this particular train crossing. Incorrect or uncertain target coordinates can be another source of systematic deviations. The observed bridge truss provides a large area for potential signal reflection, which complicates the determination of a single value for the coordinates, especially for the application of multiple sensors. Additionally, multipath effects could blur the individual resolution cells. However, this is likely not the case for this particular example since the first train crossing sees good agreement using the same coordinates. Without reference measurements, systematic deviations are generally difficult or impossible to recognise or quantify. Hence, estimating the processing's uncertainty becomes even more important.

Measurement Uncertainty Evaluation of the measurement uncertainty shows significant influences of the applied processing steps. Changes in the amplitude time series directly affect the uncertainty estimation since the underlying value is always estimated from the amplitude's SNR. Therefore, the removal of disturbances leads to an equal or lower uncertainty, whereas clutter removal can both increase or decrease the uncertainty by changing the amplitude's mean value. On one side, the calculation of the uncertainty from the amplitude simplifies the estimation of the processing steps' influence. Then again, it also carries the risk of misrepresenting the uncertainty if the amplitude is not constant, as shown for the measurements at Maxau. A time-dependent amplitude leads to varying uncertainty estimates depending on the evaluated measurement duration. It could be beneficial to determine two values: during a train crossing and during an idle

state. The atmospheric correction is also difficult to evaluate with regard to its influence on the measurement uncertainty. While it is possible to propagate the variances of the atmospheric parameters and sensors, the example for Schneckenlohe has shown that selective measurements do not correctly represent the atmospheric inhomogeneities on the signal path. The resulting uncertainty estimates would be similarly unrepresentative. In the case of the post-processing approach, an uncertainty estimate is not necessary since individual vehicle crossings are not affected.

The displacement projection is an important factor in the uncertainty estimation. Its influence highly depends on the geometric relationship of the GBRs to each other and the targets. The coordinate uncertainty can be omitted if corner reflectors precisely define the target coordinates. However, this precise localisation is usually not possible for naturally reflective features, leading to a significant influence by the coordinate uncertainty. The resulting values for Target 1 at Maxau are similar to the typical TLS measurement uncertainty of 0.1 mm to 0.2 mm. Furthermore, the standard deviations of the displacement differences between GBR and TLS are in the same order of magnitude, suggesting that the uncertainty estimation provides plausible results. Systematic deviations, as seen in the second train crossing, are however not covered by these estimations.

Generally, the two-dimensional projection increases the SNR requirements to achieve reasonable uncertainty values. However, an SNR greater than 20 dB is only achieved for 9 trusses, covering roughly a quarter of the length of the bridge field. This coverage is sufficient for an evaluation of the measurement principle, but generally too small for the determination of damage-sensitive features. Mode shapes are ideally determined for the entire structure with sufficient spatial resolution. Better results could be achieved with a different measurement setup or a wider signal beam to extend the coverage. An alternative to this challenge is also provided by the indirect measurement approach proposed in Chapter 5.

3.4 Conclusion

The processing of GBR measurements entails several challenges, especially for long measurement durations or complex setups. Based on the conventional processing approach, the proposed additional steps focus on three main aspects: removing external influences, determining more than one component of the three-dimensional displacement vector, and assessing the uncertainty of the measurements and the processing steps.

The first aspect is the removal of external influences. Broadband noise and phase jumps affect not only the measurement results but also the subsequent processing steps. Their removal relies on basic signal processing that accurately detects these disturbances in most measurement situations. Similarly, the atmospheric propagation delay is removed more reliably by a post-processing approach instead of in situ measurements of the atmospheric parameters. Influences from static reflections and insufficient focusing are removed by estimating a circular arc from the complex-valued IQ components. The estimation is necessary for most measurements since static clutter can introduce significant deviations. For certain measurement setups, the reliability of the estimation can be improved by introducing a weight matrix, which models the unequal distribution of data points. Other measurement setups show dynamic amplitude values, which considerably influence the estimation results. Although it is not possible to determine the estimation's accuracy from the data itself, an assessment of its precision might be beneficial to flag any gross errors.

Besides external influences, the three-dimensional displacement vector can have a significant impact on the measurements since GBRs generally determine a combination of two or three components. The generalised three-dimensional projection successfully separates these components and reduces systematic deviations in the resulting displacements. For most measurement setups, it is sufficient to apply only two GBRs since the displacement vector is two-dimensional. The combination of TLS and GBR has shown an additional flexibility of the projection and could be used to determine three components with only two sensors.

The third aspect of the proposed processing steps is the assessment of uncertainties. A first evaluation of the measurement uncertainty is achieved by estimating the SNR of the amplitude. To account for the uncertainties of the processing steps, the measurement uncertainty is recalculated in the case of disturbance and clutter removal. The projection propagates the uncertainty depending on the measurement geometry. Additionally, Monte Carlo simulations model the uncertainty of this geometry. While the resulting values are plausible, they do not completely characterise all possible uncertainties, as seen with the second train crossing at Maxau. The clutter removal requires an additional assessment of its accuracy to better evaluate the influence on the displacements. An improvement of the overall uncertainty could also be achieved by a more precise localisation of the target coordinates. However, this challenge is primarily dependent on the sensor specifications since the signal footprint would have to be decreased, either through a reduction of the range cells or with additional angular resolution. For the existing sensors, the proposed uncertainty estimation already leads to a more reliable assessment of the resulting displacement measurements.

Estimating Natural Frequencies for Damage Detection

This chapter includes material from

C. Michel and S. Keller. “Determining and Investigating the Variability of Bridges’ Natural Frequencies with Ground-Based Radar”. In: *Applied Sciences* 12.11 (May 2022), p. 5354. DOI: [10.3390/app12115354](https://doi.org/10.3390/app12115354).

It is cited as [61] and marked with an [orange line](#).

Condition assessment of bridge infrastructure includes the analysis of a bridge’s behaviour to static or dynamic loads over time since changes in the response can indicate deterioration or damage to the structure. Most commonly, acceleration, strain, or other directly contacting sensors measure the bridge’s vibration response to ambient excitation from wind or vehicle traffic. In OMA, the vibration response is then used to generate features such as natural frequencies, which form the basis of damage detection approaches. However, changes in temperature or vehicle traffic can significantly influence these features. Estimation methods should therefore also consider these influences and the underlying measurements to ensure sufficient accuracy in the context of damage detection. In the following, an adapted estimation approach considers GBR specific aspects to achieve a more reliable estimation of natural frequencies and their relationship to external influences.

4.1 Natural Frequencies as Damage Sensitive Features

Natural frequencies are commonly used as damage sensitive features since changes over time can indicate deterioration or damage to the structure. It is possible to reliably estimate frequencies from a few or even singular measurement points at the bridge. However, varying temperature of the observed structure leads to significant frequency changes, which may be higher than changes induced by damage [33, 92]. Most studies

suggest a linear relationship between temperature and frequency in the case of temperatures above freezing [5, 46]. For a wider temperature range, the relationship is modelled by a piecewise linear function with a discontinuity at 0°C [40, 74]. Some studies use more complex models to describe a non-linear relationship [23, 67]. While the temperature generally has the most significant influence, a frequency change can also be observed for varying traffic loads. The added mass of vehicles can significantly affect the frequency of short-span bridges. Long-span bridges, however, do not show a significant frequency change since the ratio between vehicle mass and bridge mass is negligible [42]. Besides natural frequencies, other modal parameters also constitute suitable features for damage detection [25]. For example, mode shapes are insensitive to temperature or mass changes and can additionally localise damage [5, 103]. However, the determination of mode shapes is more complex compared to natural frequencies since multiple measurement points throughout the structure are required. Systematic deviations can also significantly influence the results, which is especially relevant for GBR measurements. A more detailed investigation regarding the estimation of mode shapes from GBR measurements is given in Section 5.3, while this chapter focuses on natural frequencies.

Natural frequencies can be estimated with parametric and non-parametric methods, which are applied in the time domain or frequency domain [81]. For example, Natural Excitation Techniques or SSI are popular methods in the time domain. However, the most common methods are based on the frequency domain since the domain change is easy to compute and identification of the natural frequencies is straightforward. For example, a good approximation can be achieved by calculating the PSD matrix. Natural frequencies are easily identified by their spectral peaks if the modes are well separated. As an advancement on this principle, the FDD applies an SVD to the PSD matrix [10]. This decomposition generates spectra which correspond to single degree of freedom (SDOF) systems for each mode. The natural frequencies then result from the singular values, which represent the auto spectral density functions of the SDOF systems. Mode shapes are additionally estimated from the singular vectors at the corresponding peaks of the auto spectral density functions.

While frequency estimation with FDD or other frequency domain methods is very reliable, there are also some disadvantages. For example, the PSD matrix is calculated from a time window of the measurements. This time window usually has a length in the range of minutes, which ideally ensures broadband excitation of all modes and also determines the available frequency resolution. However, individual vehicle crossings can no longer be distinguished, which complicates the analysis of vehicle mass and its contribution to the natural frequencies, as mentioned above. Small frequency changes may also be

obscured by the rough frequency resolution, necessitating an overall longer measurement duration to detect these changes. For GBR in particular, the aggregation of all available measurement targets into one PSD matrix might not be beneficial since the individual uncertainties of each target can differ substantially. Therefore, the following section proposes an approach that allows a separate assessment of each vehicle crossing while accounting for the individual uncertainties.

4.2 Least Squares for Estimation of a Damped Sinusoid

The approach focuses on the damped vibration following most vehicle crossings on smaller and less frequented bridges. Each vibration is separately evaluated by estimating the model of a damped sinusoid in the time domain. The advantage of this separate evaluation is that different measurement uncertainties of the individual GBR targets can be considered in the estimation process. Additionally, different vehicle types can be distinguished to analyse the influence of vehicle mass on the estimated frequencies. Since the approach is applied in the time domain, the frequency resolution is not dependent on a time window, as is the case for frequency domain methods. However, the approach requires an uninterrupted vibration after a vehicle crossing and is therefore more applicable for smaller bridges with less traffic. Then again, smaller bridges see a greater influence on natural frequencies by the added vehicle mass [42].

Figure 4.1 shows an overview of the approach. Various types of measurements can generally be used as input data for the approach; however, this study focuses on GBR and strain measurements. At first, a preprocessing step filters the measurements and detects the damped vibrations after a vehicle crossing. The model of a damped sinusoid is then fitted to each vibration by least squares, while evaluating the goodness of fit relative to the underlying measurement uncertainty. The least squares estimates several parameters, for example, the natural frequency, which can be used for damage detection after analysing and removing external influences. Other parameters, such as the damping ratio or the amplitude, are generally not damage sensitive, and their estimation results are much more uncertain than the frequency results. Therefore, the following analysis focuses on natural frequencies.

It should be noted that analysing each vibration separately disregards an essential assumption of output-only analysis. The excitation force of a particular vibration is not broadband and introduces a bias to the frequency estimation. Therefore, the following analysis always considers a large number of vibrations and cannot draw conclusions from individual estimates.

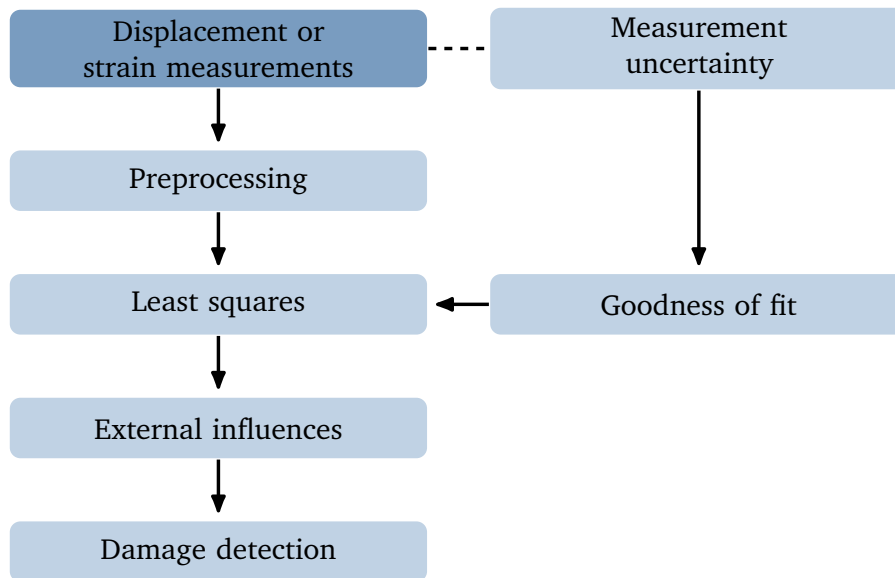
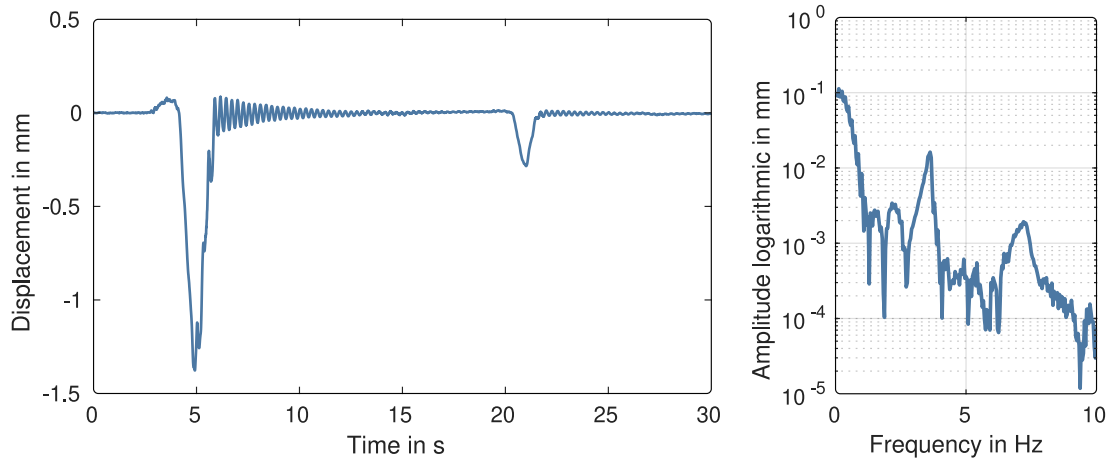


Figure 4.1: Overview of the approach for natural frequency estimation.

4.2.1 Preprocessing

Figure 4.2a shows an example of typical bridge displacements measured with a GBR for two vehicle crossings. A free damped vibration follows the initial displacement caused by a vehicle. This vibration can be primarily observed in crossings of heavy vehicles, such as trucks. However, it also occurs after crossings of lighter vehicles, such as cars, although the amplitude of the vibration is much smaller. Figure 4.2b shows the amplitude spectrum of the displacement. The first and second natural frequencies are visible at approximately 3.6 Hz and 7.2 Hz, respectively. Generally, the amplitude of the second natural frequency is about an order of magnitude smaller than the amplitude of the first natural frequency. Higher frequencies may still be detectable by GBR if they are sufficiently excited at the respective measurement points, and the SNR of the measurements is high enough. Other studies have determined multiple dominant frequencies with GBR [56, 72]. However, this thesis focuses on the first natural frequency to show the application of the proposed methodology.

Since the damped vibrations have recognisable characteristics in the frequency domain, their startpoints and endpoints can be detected relatively easily. A common signal processing method for detection is a bandpass filter with a passband of the first natural frequency. The vehicle crossing is then determined by applying a threshold. Alternatively, machine learning methods constitute a more complex but also more flexible approach. Combining two methods makes it possible to detect vehicle convoys, which interrupt the damped vibration [6].



(a) Bridge displacement in the time domain.

(b) Amplitude spectrum.

Figure 4.2: Example of vehicle crossings in the time and frequency domain in Seßlach. Adapted from [61].

After detection, a high-pass filter with a cut-off frequency below the first natural frequency is applied to mitigate the influence of low-frequency components on the least squares. These components can originate from multiple sources. Most commonly, a residual lifting of the observed bridge field can occur due to the vehicle crossing over a neighbouring field. In the case of GBR, short-term atmospheric effects can cause low-frequency components since these effects may not be fully removed by the atmospheric correction (see Section 3.1.3). Multiple scatterers in the same range cell can also influence the displacement measurement depending on their amplitude in relation to the primary reflection.

If multiple targets or sensors are used, their measurements can be combined or selected depending on multiple approaches to maximise SNR. For example, strain sensors of the same type generally have similar noise levels and their noise is uncorrelated. Therefore, averaging the measurements reduces the noise power by a factor of N , where N is the number of sensors. In the case of GBR, the targets usually have different signal reflection. Combining multiple displacement measurements may result in worse SNR than the measurement with the highest SNR. Using only one measurement might benefit the frequency estimation since the natural frequency is equal throughout the entire structure.

4.2.2 Least Squares Approach

The bridge's response to a vehicle crossing can be modelled by a sinusoidal function with an additional damping term:

$$y(t) = a \cdot e^{-\Lambda t} \cdot \sin(2\pi f t + \theta) \quad (4.1)$$

The sinusoid is defined with the natural frequency f and the phase θ . An enveloping exponential function determines the damping with the initial amplitude a and the decay rate Λ . From the decay rate, the damping ratio ζ can be determined:

$$\zeta = \frac{\Lambda}{\sqrt{\Lambda^2 + 4\pi^2 f^2}} \quad (4.2)$$

A least squares approach minimises the error distances between this model and the measured displacements. Since the model is non-linear, it has to be linearised at the approximate values of the parameters. The approximate values of natural frequency and phase are easiest to determine with a DFT. Although the frequency resolution is limited with the typical time window of a few seconds, the quality of the approximate values is generally high enough for the convergence of the least squares. An approximate value for the decay rate is calculated from the logarithmic decrement, which is defined as the ratio of adjoining peaks x_i of the sinusoid:

$$\Lambda^0 = f \cdot \ln\left(\frac{x_i}{x_{i+1}}\right) \quad (4.3)$$

The amplitude a can be approximated from the highest peak of the sinusoid. The approximate parameters are iteratively improved until the least squares converges.

4.2.3 Evaluation of the Least Squares Estimation

The test for goodness of fit evaluates the quality of the estimated parameters. The test is necessary because additional vehicle crossings or other noise content may interrupt the damped vibration. Poor approximate values for the parameters might also cause the least squares to converge to a local minimum instead of the global minimum. The goodness of fit can be evaluated with different methods. For example, the standard error of the estimate

$$s_{\text{est}} = \sqrt{\frac{\sum \varepsilon_i^2}{\nu}} \quad (4.4)$$

is calculated from the sum of squared residuals ε divided by the degree of freedom ν . If the model fits the measurement well, the standard error of the estimate should only contain broadband measurement noise. Therefore, a small difference between s_{est} and the previously estimated measurement uncertainty (see Section 2.1.2) indicates a good fit. Alternatively, the coefficient of determination

$$R^2 = 1 - \frac{\sum \varepsilon_i^2}{\sum (y_i - \bar{y})^2} \quad (4.5)$$

is defined with the sum of squared residuals divided by the sum of the squared difference between measurements y_i and their mean value \bar{y} . Both approaches require a threshold to indicate a good model fit.

4.2.4 Damage Detection Based on a Hypothesis Test

Changes in the natural frequencies are primarily caused by varying temperatures but can also result from damage to the structure. Therefore, the results of the least squares approach can also be used to test for damage, provided that temperatures are measured, and an undamaged reference state of the bridge was previously observed. The reference measurements correct the relationship between temperature and frequency, ideally resulting in normally distributed frequencies. This correction is also applied to the test measurements to test for equality of the two distributions' means. A significantly different mean can indicate damage to the structure. Usually, the number of reference measurements will be much higher than the number of test measurements, resulting in unequal sample sizes. It can also not be assumed that the variances of the distributions are equal because damage might influence the variance of the natural frequencies. Therefore, Welch's t -test can be used to test for equal means. Welch's t -test defines the test statistic γ with the distributions' means \bar{x}_i and the standard deviation s :

$$\gamma = \frac{\bar{x}_1 - \bar{x}_2}{s} \quad (4.6)$$

The standard deviation s results from the distributions' standard deviations s_i and sample sizes n_i :

$$s = \sqrt{\frac{s_1^2}{n_1} + \frac{s_2^2}{n_2}} \quad (4.7)$$

The test statistic is approximately t -distributed with the degree of freedom ν :

$$\nu = \frac{s^4}{\frac{\left(\frac{s_1^2}{n_1}\right)^2}{n_1-1} + \frac{\left(\frac{s_2^2}{n_2}\right)^2}{n_2-1}} \quad (4.8)$$

With a significance level α , the null hypothesis of equal means is rejected under the following condition:

$$|\gamma| > t_{1-\alpha/2, \nu} \quad (4.9)$$

4.3 Results

The least squares approach is applied to measurements at two bridges in Schneckelohe and Seßlach. For a comprehensive evaluation, the measurements took place during different times of the year and cover a wide temperature range. The estimated natural frequencies are analysed in relation to the measured temperatures, and a simulation shows their potential in the context of damage detection. Each analysis is supported by a comparison to results obtained by FDD from GBR and strain measurements.

4.3.1 Measurement Setup

Seßlach

The bridge in Seßlach (near Coburg, Germany) is a prestressed concrete structure with two spans, as discussed in Section 2.3.3. The measurement setup at the eastern span is shown in Figure 4.3. Similarly to the measurements in Schneckelohe (see also Section 3.2.1), the two GBR (IBIS) have to be setup orthogonally to each other to avoid interference. Therefore, GBR 1 requires corner reflectors on the underside of the bridge to ensure sufficient signal reflection, subsequently referred to as Target 1 to 5. With these reflectors, both GBRs achieve an average SNR during all measurement days of 34 dB to 40 dB for Targets 2, 3, and 4. In the case of Targets 1 and 5, the average SNR is significantly lower at 22 dB to 26 dB due to the increasing attenuation of the signal beam. Reference measurements are provided by one-dimensional strain sensors from HBM (Darmstadt, Germany), which are installed in the middle of the T-beams. The positions

of the reflectors do not strictly coincide with the positions of the strain sensors, since the reflectors have to occupy different range cells for GBR1. However, their positions are irrelevant for the determination of natural frequencies because the frequencies are equal throughout the structure. Lastly, the temperature is measured by a temperature sensor directly on the concrete surface. The sensor is installed at the bridge's pillar on the shaded north side.

An overview of the measurement campaigns is shown in Table 4.1a. The measurements took place during different times of the year to cover a wide temperature range. In total, 16 h of measurements during seven days span a temperature range of 3 °C to 24 °C.

Schneckenlohe

The prestressed concrete bridge in Schneckenlohe (near Coburg, Germany) has one span and two T-beams, as discussed in Section 2.3.1. With the measurement setup shown in Section 3.2.1, the vertical displacement component is determined. Both GBRs achieve an average SNR of 26 dB to 30 dB for the targets at the two T-beams. Some additional sensors provide measurements for the subsequent analysis of the temperature-frequency relationship. The temperature is measured by a sensor on the shaded north side of the bridge pillar, and two strain sensors from HBM are installed in the middle of the beams in direct proximity to the reflectors, as shown in Figure 4.4.

Section 3.2.1 only discusses one measurement campaign, whereas the following analysis covers multiple campaigns over two years. Table 4.1b shows an overview of the campaigns. A temperature range of 7 °C to 27 °C is covered with 16 h of measurements over six days.

Table 4.1: Measurement campaigns with durations and temperature ranges.

(a) Seßlach, Germany. Reprinted from [61].

(b) Schneckenlohe, Germany.

Day	Duration in h	Temperature range in °C	Day	Duration in h	Temperature range in °C
29 Aug 2019	0.6	22 to 24	27 Aug 2019	1.6	24 to 26
30 Aug 2019	1.2	20 to 23	28 Aug 2019	5.6	19 to 27
23 Oct 2019	4.1	10 to 15	22 Oct 2019	2.6	12 to 14
24 Oct 2019	1.8	8 to 10	25 Feb 2020	2.1	7 to 8
27 Feb 2020	3.2	3 to 6	28 Jul 2020	4.0	22 to 25
29 Jul 2020	3.1	17 to 21	10 Jun 2021	0.3	18 to 19
9 Jun 2021	2.0	19 to 22			

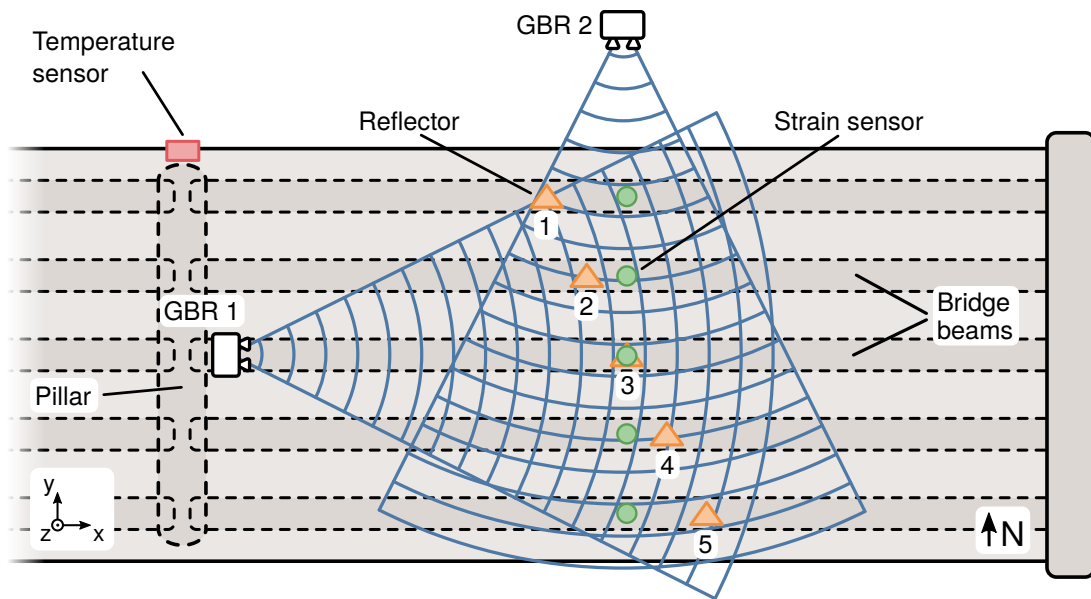


Figure 4.3: Measurement setup at the bridge in Seßlach.

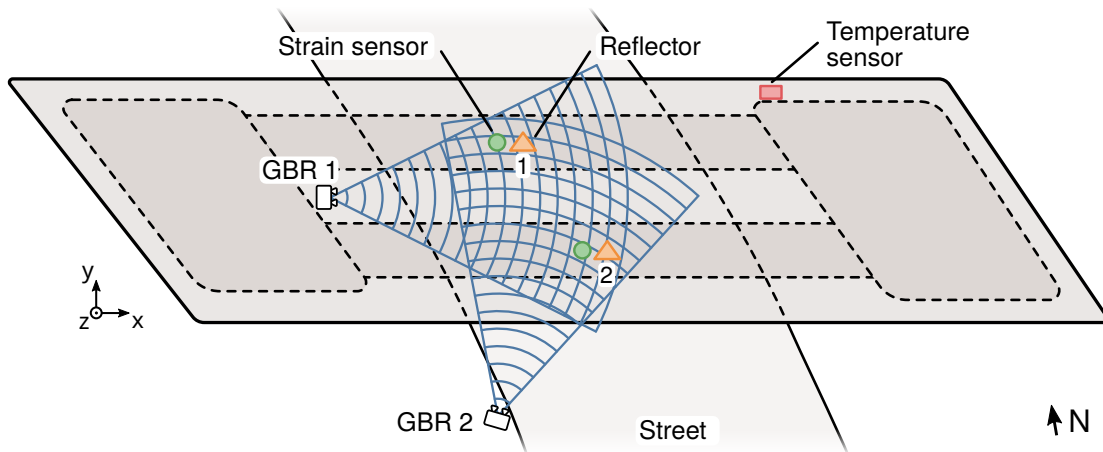


Figure 4.4: Measurement setup at the bridge in Schneckenlohe.

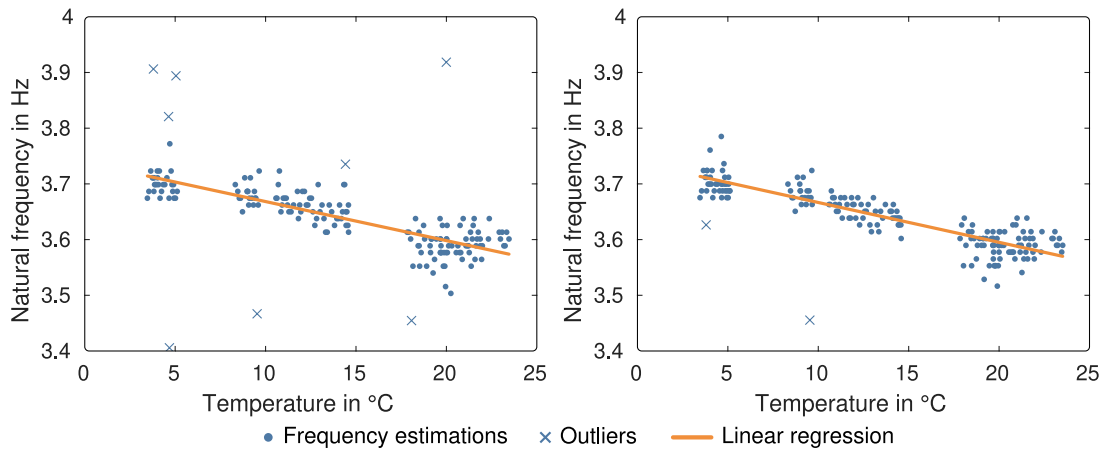
4.3.2 Analysis of the Relationship Between Temperature and Natural Frequency

Changes in temperature significantly influence natural frequencies, as has been shown by several studies [33, 92]. Performing damage detection on estimated frequencies requires a reliable determination of this influence. In the following, the natural frequencies are estimated by FDD with a time window of 5 min for the two bridges in Seßlach and Schneckenlohe. Figure 4.5 shows the results from GBR and strain data in Seßlach as a function of the temperature. For both sensors, an increase in temperature is correlated with a decrease in frequency. The relationship is assumed to be linear and can be estimated by linear regression. For comparison of the two sensors, the slope and offset parameters of the regressions are shown in Table 4.2. The frequency changes by approximately -0.07 Hz per 10 °C. After correcting the linear relationship, the frequency estimates of the GBR data have a standard deviation of 0.026 Hz, while the strain sensors' estimates have a standard deviation of 0.023 Hz. The mean frequency is approximately equal. For a successful estimation of this linear relationship, it is necessary to remove several outliers. The outliers are identified by iteratively testing if the regression's residuals fit a normal distribution. While only three outliers are removed from the strain sensors' results, the GBR data contains 24 outliers, which are marked as crosses in Figure 4.5. Outliers exceeding the plot limits are omitted.

In the case of the frequency estimations in Schneckenlohe, the relationship between frequency and temperature cannot be clearly identified. Figure 4.6 shows the results for the GBR and strain sensor data. The frequency estimates in the temperature range of 5 °C to 15 °C might exhibit a similar correlation as seen in Seßlach. However, temperatures above 20 °C show a reverse correlation: higher temperatures lead to higher frequencies. This effect is seen for both the GBR and strain sensor data. Further discussion and a possible cause are given in Section 4.4. Since the relationship between frequency and temperature is not clearly identified, the frequency estimates prevent a successful damage detection. Therefore, the following analysis only considers the results of the measurement campaign in Seßlach.

Table 4.2: Results of the linear regression for the temperature-frequency relationship estimated by FDD with a time window of 5 min in Seßlach.

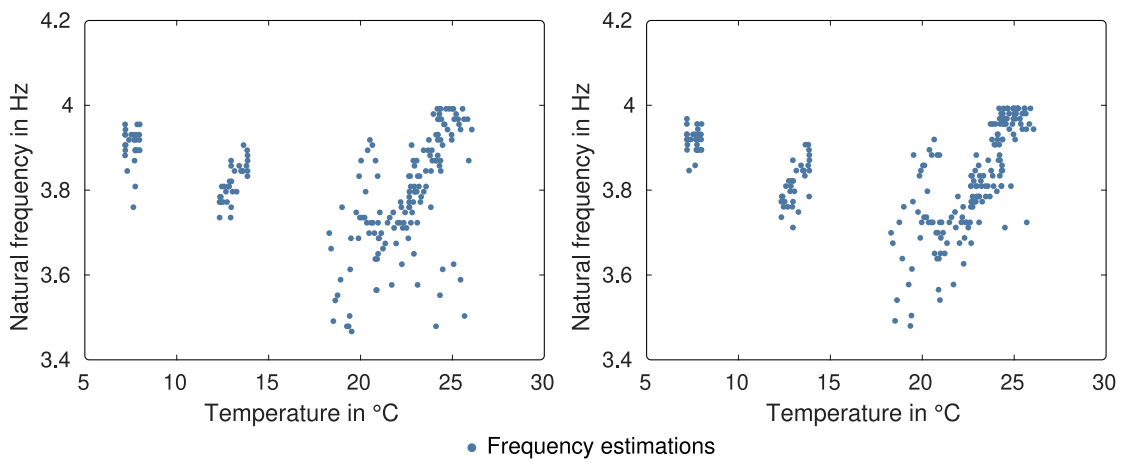
Sensor	Frequency change in Hz per 10 °C	Mean in Hz	Standard deviation in Hz	Number of estimations	Number of outliers
GBR	-0.070	3.654	0.026	193	24
Strain	-0.072	3.652	0.023	193	3



(a) Results from GBR.

(b) Results from strain sensors.

Figure 4.5: Natural frequencies as a function of temperature estimated by FDD with a time window of 5 min in Seßlach.

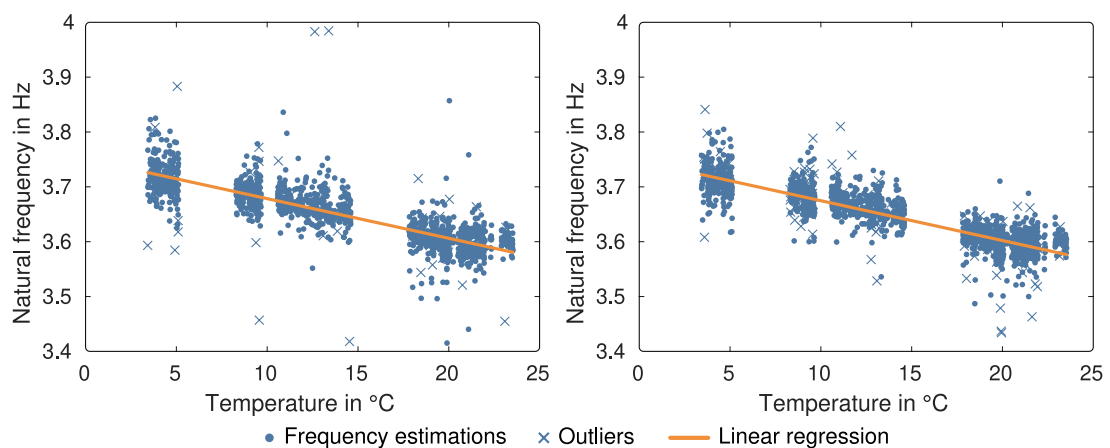


(a) Results from GBR.

(b) Results from strain sensors.

Figure 4.6: Natural frequencies as a function of temperature estimated by FDD with a time window of 5 min in Schneckenlohe.

The least squares uses different approaches to estimate frequencies from the two sensors' data. For GBR, the frequencies are estimated from the target with the highest SNR and thus the lowest measurement noise, which is subsequently referred to as the *best approach*. Additionally, two other approaches are tested for comparison. The strain sensors generally have similar measurement precision and noise content and thus benefit from averaging the measurements to increase SNR, also called the *mean approach*. Figure 4.7a shows the estimation results for GBR. Outliers are marked with crosses if the test for goodness of fit falls below a threshold of $R^2 = 50\%$. Some outliers exceed the plot limits and are omitted. For direct comparison, Figure 4.7b shows the estimation results for the strain sensors. The linear relationship between frequency and temperature is calculated by linear regression. Both datasets exhibit a similar frequency change of approximately -0.072 Hz per 10°C (see also Table 4.3). After correcting the linear relationship, the mean value is around 3.66 Hz for both datasets. The standard deviation of the GBR's frequency estimates is 0.027 Hz, while the strain sensor estimates result in a standard deviation of 0.046 Hz. The test for goodness of fit identifies 123 outliers for the GBR and 159 outliers for the strain sensors. Table 4.3 shows two additional approaches for further comparison of the GBR data. The *mean approach* results in 366 outliers and a standard deviation of 0.05 Hz after correcting the linear relationship. Every GBR target is individually evaluated in the *single approach*. About 2100 outliers are identified for this approach. After correcting for the linear relationship, the standard deviation of the frequency estimates is 0.19 Hz.



(a) Results from GBR with *best approach*.

(b) Results from strain sensors with *mean approach*.

Figure 4.7: Natural frequencies as a function of temperature estimated by least squares in Seßlach. Adapted from [61].

Table 4.3: Results of the linear regression for the temperature-frequency relationship estimated by least squares in Seßlach. Reprinted from [61].

Sensor & approach	Frequency change in Hz per 10 °C	Mean in Hz	Standard deviation in Hz	Number of estimations	Number of outliers
Strain - Mean	-0.073	3.660	0.046	1709	159
GBR - Best	-0.072	3.664	0.027	1709	123
GBR - Mean	-0.075	3.663	0.050	1709	366
GBR - Single	-0.072	3.668	0.192	7253	2103

4.3.3 Variation of the Linear Regression for Estimating the Temperature Influence

Since practical applications may require shorter measurement times or fewer campaigns, the number of frequency estimations may be reduced, thus influencing the linear regression. In the following, we analyse the reliability of the linear regression by simulating two types of data reductions. At first, the reduction is implemented by drawing uniformly distributed random samples from the least squares and FDD results, respectively. Figure 4.8 shows the variation of the linear regression's parameters calculated from one thousand samples for each sample size. The standard deviation of the slope parameter in Figure 4.8a slowly increases as the sample size is reduced. With very small sample sizes, the growth can be characterised as exponential. The standard deviation is continually smaller for the least squares result than it is for the FDD. Although this difference can be observed for both the GBR and the strain sensors, it is much more distinct for GBR. Figure 4.8b shows very similar observations for the offset parameter of the linear regression.

A second simulation excludes entire measurement days combined with uniformly distributed random samples. Figure 4.9a exemplarily shows the variation of the linear regression for a sample size of 25%. The measurement days only include the 23 and 24 October 2019, with temperatures in the range of 8 °C to 15 °C. The samples are drawn one thousand times from the GBR FDD result to visualise the standard deviation of the linear regression. Additionally, one sample and its corresponding regression are plotted to illustrate the data reduction. For direct comparison, Figure 4.9b shows the least squares result for this simulation. The standard deviation of the linear regression is much higher for the FDD than for the least squares approach, especially in the case of extrapolated values outside the reduced temperature range. A similar result can be seen in Figures 4.10a and 4.10b. The simulation uses two measurement days with a greater differential between lowest and highest temperatures than the first simulation. Temperatures are between 3 and 6 °C on 27 February 2020 and between 17 and 21 °C on

29 July 2020. As a result, the linear regression varies much less for the least squares approach and the FDD than in the previous simulation. However, the FDD still has a higher standard deviation than the least squares approach.

These results are also indicative of the performance in damage detection with a hypothesis test. The following simulation illustrates the necessary properties of such a test and compares the minimum required frequency change detectable from the FDD and least squares results. Estimating the minimum difference required between the test distribution and the reference distribution is achieved by simulating a test measurement. It is assumed that the test distribution consists of frequency estimates from 30 min of measurements with a standard deviation equal to the reference distribution. Furthermore, both distributions are normally distributed. While the significance level is highly dependent on the application and the required accuracy of the test, a significance level of 5% constitutes a reasonable value for this simulation. With these assumptions, the least squares approach with GBR measurements would result in approximately 50 frequency estimations and a minimum detectable difference of 8 mHz. The FDD with a 5 min window generates 6 frequency estimations resulting in a difference of 27 mHz. In the case of the strain sensors' measurements, the least squares approach requires a difference of 13 mHz, whereas the FDD results in a minimum difference of 24 mHz.

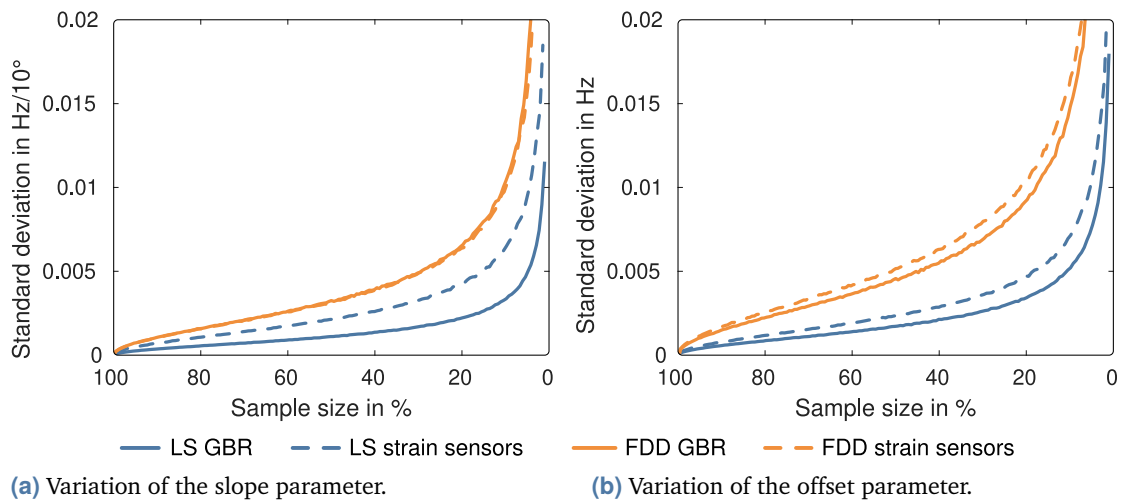
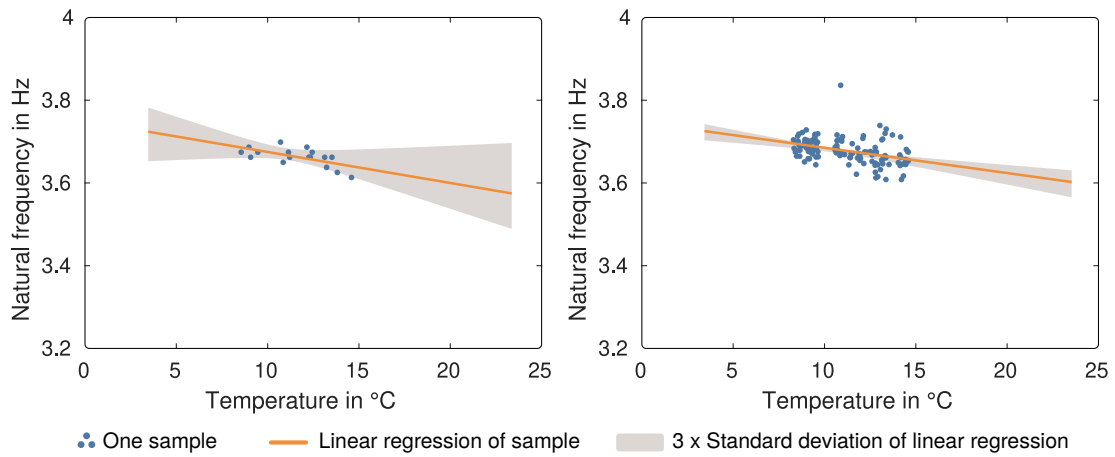


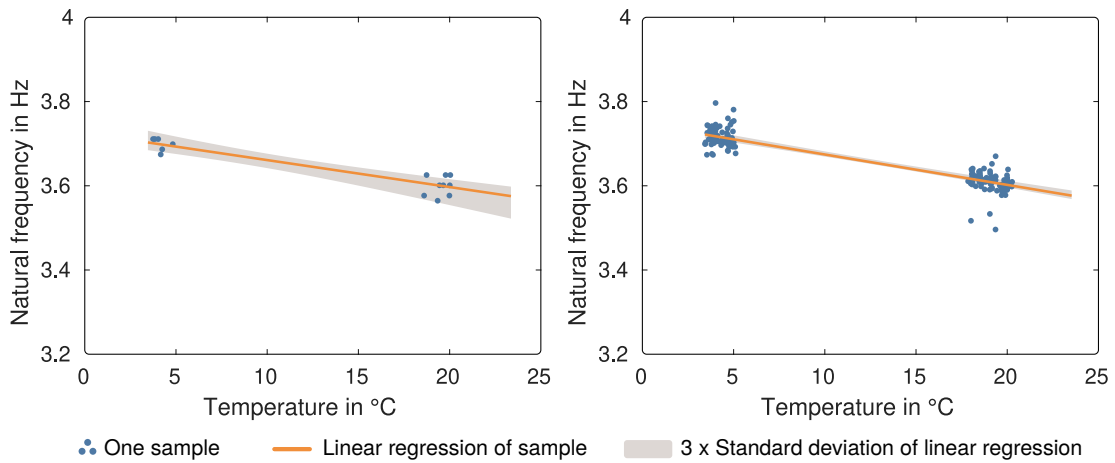
Figure 4.8: Variation of the linear regression depending on sample size in Seßlach. The least squares (LS) uses the *best approach* for GBR and the *mean approach* for the strain sensors. The FDD uses a time window of 5 min.



(a) FDD with a time window of 5 min.

(b) Least squares with *best approach*.

Figure 4.9: Variation of the linear regression for GBR measurements with a sample size of 25% and a reduction of the measurement days to 23 and 24 October 2019 in Seßlach.



(a) FDD with a time window of 5 min.

(b) Least squares with *best approach*.

Figure 4.10: Variation of the linear regression for GBR measurements with a sample size of 25% and a reduction of the measurement days to 27 February and 29 July 2020 in Seßlach.

4.3.4 Influence of Vehicle Types on Natural Frequencies

Since the least squares approach estimates frequencies from the damped vibration after a vehicle crossing, a separate analysis of different vehicle types and their influence on the first natural frequency is possible. Vehicle types can be distinguished by the peak displacement during a crossing since the displacement is approximately proportional to the vehicle's mass. In the following, we only differentiate between two major types of vehicles. Light vehicles have an absolute peak displacement of smaller than 0.5 mm and include cars, vans, and small trucks. Accordingly, heavy vehicles, such as trucks or trucks with trailers, are characterised by an absolute peak displacement higher than 0.5 mm. The threshold is certainly chosen arbitrarily and may only be a rough characterisation of the suggested vehicle types. However, Table 4.4 clearly shows an influence on natural frequency estimation. After correcting the linear relationship of frequency and temperature with linear regression, the heavy vehicles have a lower frequency mean than the light vehicles by about 0.01 Hz. The slope of the regression and the standard deviation are approximately equal. For strain measurements, a comparable distinction between light and heavy vehicles can be achieved with a threshold of $6 \mu\text{m m}^{-1}$. Table 4.4 shows a difference in the frequency mean of 0.012 Hz between the vehicle types. Furthermore, the standard deviation increases to 0.062 Hz for heavy vehicles and decreases to 0.022 Hz for light vehicles.

Table 4.4: Comparison of vehicle types with least squares in Seßlach. For the GBR, the *best approach* is used and vehicles are characterised by the absolute of the peak displacement: heavy vehicles $> 0.5 \text{ mm}$, light vehicles $< 0.5 \text{ mm}$. For the strain sensors, the *mean approach* is used and vehicles are characterised by the peak strain: heavy vehicles $> 6 \mu\text{m m}^{-1}$, light vehicles $< 6 \mu\text{m m}^{-1}$. Reprinted from [61].

Sensor	Vehicles	Frequency change in Hz per 10°C	Mean in Hz	Standard deviation in Hz	Number of estimations	Number of outliers
GBR	All	-0.072	3.664	0.027	1709	123
	Heavy	-0.070	3.659	0.028	721	26
	Light	-0.074	3.668	0.026	988	97
Strain	All	-0.073	3.660	0.046	1709	159
	Heavy	-0.075	3.654	0.062	741	19
	Light	-0.072	3.666	0.022	968	140

4.4 Discussion

The measurements in Seßlach show a typical temperature-induced change of the first natural frequency, as already shown for other bridges (e.g. [33, 92]). This linear relationship is not observed for the measurements in Schneckenlohe. Especially for higher temperatures, the relationship reverses, which leads to a frequency increase instead of a decrease. There are two possible explanations for this observation. First, an error or a systematic deviation in the measurements could obscure the actual relationship between temperature and frequency. A systematic deviation would most likely occur in the temperature measurements since only one sensor is used to model the behaviour of the entire structure. Especially on days with direct sunlight, the bridge's temperature distribution could become irregular, and the single temperature sensor would not be representative for the observed frequency change. Then again, the bridge in Seßlach also experiences high temperatures and direct sunlight, but the single temperature sensor appears to correctly model the bridge's behaviour. An error in the displacement measurements is also unlikely since the strain measurements show the same non-linear relationship between temperature and frequency. Therefore, it can be assumed that this relationship rather results from an atypical behaviour of the bridge. Cornwell et al. [18] describe two possible causes that could also apply to the bridge in Schneckenlohe. First, debris in the expansion joints could prevent the structure's thermal expansion, which would influence the natural frequencies. Second, moisture evaporation could decrease the structure's mass leading to a frequency increase. Regardless of the cause, no damage detection can be performed without a mathematical model describing the relationship between temperature and frequency. Therefore, the following discussion focuses on the results in Seßlach.

At first, the results of the least squares approach are discussed, followed by a comparison to the FDD. The approach is able to determine natural frequencies from GBR displacement measurements as well as from strain measurements. Generally, the approach benefits from measurements with high SNR resulting in a smaller variation of the frequency estimations and fewer outliers. In the case of the strain sensors, the highest SNR is achieved by averaging all measurements in the *mean approach*. Since the sensors have a similar (uncorrelated) noise level, averaging reduces the noise power. In the case of GBR, the *best approach* uses the measurement of the target with the highest SNR, which results in the lowest standard deviation and fewest outliers for the frequency estimations. Averaging multiple targets does not increase the SNR compared to the target with the best SNR. One cause for this is the significant difference in signal reflection for the GBR

targets, which leads to dissimilar SNRs. Secondly, the sensor noise as part of the overall noise level may be correlated between targets.

A comparison of the two sensors shows very similar results for the linear regression. After correcting the linear relationship, the GBR achieves a smaller standard deviation than the strain sensors. This difference can be explained by a higher SNR for the GBR, even though the noise level for the strain sensors is improved by averaging. The strain sensors' result still has some undetected outliers influencing the standard deviation. Choosing a threshold for the goodness of fit is always a compromise between the number of false positives and false negatives. A threshold of $R^2 = 50\%$ reduces the number of false negatives to improve the reliability of the linear regression. The resulting higher number of false positives is acceptable since the remaining number of frequency estimations is still very high. The threshold is equal for both sensors to achieve a direct comparison. However, the strain sensors would require a higher threshold of around $R^2 = 70\%$ to reach a standard deviation comparable to GBR. The number of outliers for both sensors generally shows the importance of the test for goodness of fit in the least squares approach.

After comparing the two sensor types, the least squares approach is evaluated against the FDD. Both methods generally result in very similar linear regressions. However, the frequency mean is slightly lower when calculated by the FDD. This difference is caused by the large time window of several minutes, which contains multiple vehicle crossings. Most importantly, the time window also includes the crossing itself with the added mass of the vehicle. For small bridges, the added mass significantly lowers the natural frequency, which is observed indirectly through the averaging effect of the FDD. Another effect of the time window is the significantly lower number of frequency estimations compared to the least squares approach. This effect causes more significant variation in the linear regression, as shown in Figures 4.8 to 4.10. The simulations demonstrate that the least squares approach allows shorter measurements and a narrower temperature band than the FDD. For example, a real-world monitoring scenario could be constructed with only one measurement during the summer and one during the winter. The resulting temperature range would be sufficient to estimate the linear relationship with the least squares approach and perform damage detection on new measurements. However, it is important to note that the simulations only provide qualitative comparisons between the two methods and cannot assess the accuracy of the linear regression itself. For example, biases caused by an unequal temperature distribution are not considered since the temperature is measured at only one location on the exterior of the structure.

The simulation of the hypothesis test for damage detection shows that minimal changes in the frequencies' mean can be detected. However, the discussed values for the minimum

difference should only be interpreted as a qualitative comparison between the sensors and methods. Biases in temperature or skewed distributions could significantly influence the test, leading to much higher required differences. Since the test mainly depends on the standard deviations of the distributions, the strain sensors' result requires a higher difference than the GBR's result. However, the test also leads to a higher difference if the number of elements in the test distribution decreases. The few elements in the FDD's test distribution result in a much higher value, indicating that longer measurement times are required for this method.

Since the least squares approach estimates the frequency for every vehicle crossing separately, it can be further distinguished between heavy and light vehicles. Even though the approach only uses the damped vibration after a vehicle has already left the bridge, a difference between the two types can still be determined. The difference in the frequency mean is likely to result from a residual influence of the lower natural frequency during the vehicle crossing. A residual influence of the excitation frequency is also possible. The difference could become relevant for damage detection if the vehicle type distribution significantly changes between consecutive measurements. For example, a (temporary) diversion of heavy vehicles to or from the monitored bridge could possibly induce a significant frequency change detectable with a hypothesis test. If the change in the vehicle type's distribution is not noticed, the frequency change could be misinterpreted as damage to the structure. The difference in the frequency mean is comparably determined from both the GBR's result and the strain sensors' result. However, the standard deviation changes significantly between vehicle types for the strain sensors, which is not observed for the GBR. The higher standard deviation for heavy vehicles results from outliers, which are not detected by the test for goodness of fit. As discussed before, with a higher threshold, the strain sensors can achieve comparable results to the GBR.

4.5 Conclusion

Natural frequencies constitute viable features for damage detection of bridge infrastructure if external influences such as temperature changes are considered. While frequencies can easily be estimated by frequency domain methods, an adapted approach in the time domain is beneficial for GBR measurements. The proposed least squares approach evaluates each vehicle crossing separately, which enables further analysis regarding the influence of vehicle mass on natural frequencies. In addition, the temperature influence can be determined more reliably compared to the FDD, which is shown by simulating a reduction of available measurements. Shorter measurement durations decrease the

number of frequency estimations, leading to increased variance of the estimated linear relationship between temperature and frequency. This variance increase is much higher for the FDD than the least squares approach.

The reliability of the least squares approach is primarily determined by the performance of the goodness of fit, which filters outliers during the frequency estimation step. A subsequent outlier test, as required by the FDD, is not necessary. However, the least squares approach ideally requires uninterrupted vibrations and is therefore mostly applicable to bridges with a lower traffic volume and a higher likelihood of singular vehicle crossings. Additionally, the evaluation only considers the estimation of the first natural frequency. Determining higher modes should still be possible with an adaptation of the bandpass filter. However, the estimation would become more challenging because the amplitudes of higher modes decrease significantly in the case of displacement or strain measurements. As an alternative, the approach could also be applied to acceleration measurements, which are much more sensitive for higher frequencies.

The analysis of the temperature-frequency relationship shows a strong linear correlation for the bridge in Seßlach, whereas the bridge in Schneckenlohe exhibits an atypical non-linear behaviour. The likely source of this behaviour are boundary conditions of the bridge expansion. A systematic deviation in the temperature measurement could also be responsible. Since the temperature is an integral part of damage detection, a singular measurement can generally not be sufficient. Multiple measurements throughout the structure could detect an irregular temperature distribution and improve the reliability of damage detection with natural frequencies.

Indirect Displacement Measurements for Mode Shape Estimation

In the conventional measurement approach, the emitted signal is reflected back to the GBR by features on the underside of the bridge. For example, beams or trusses provide sufficient signal reflection if they are orientated orthogonally to the GBR's LOS and are a few times the size of the wavelength. Many bridges, however, have flat (concrete) surfaces instead of these features, requiring the installation of corner reflectors, as exemplarily shown in Section 3.2.1. The installation can be difficult depending on the construction of the bridge or may interrupt its normal operation. As a consequence, the GBR's main advantage of minimal setup time and remote measurement compared to directly contacting sensors is diminished. Additionally, an influence of the horizontal displacement components can introduce significant systematic deviations in the conventional measurement approach. Although the application of more than one sensor in the three-dimensional projection can significantly reduce these errors, small deviations to the actual vertical displacements may still remain, as shown in Section 3.2.5. The two-dimensional projection also increases the measurement uncertainty, which reduces the evaluable area of the bridge (see Section 3.2.6).

These challenges complicate the analysis of damage-sensitive features such as mode shapes. Mode shapes are estimated from the displacement measurements of multiple points over a wide area of the bridge. Damage is then detected by analysing the changes of these mode shapes over time. Therefore, time-dependent deviations directly influence the estimated mode shapes and could be falsely identified as damage. Additionally, a high measurement uncertainty due to the three-dimensional projection could obscure real damage.

The alternative measurement approach discussed in this chapter aims to mitigate these challenges for a reliable estimation of mode shapes. It utilises the flat surface of a bridge underside to mirror the signal to the ground opposite of the GBR, as first proposed by Pieraccini et al. [78]. The signal is then reflected back on the same path, enabling the measurement of vertical displacement. In the following, the methodology and an

application at a bridge are shown. The results are additionally validated with two reference sensors, followed by a discussion of the advantages and arising challenges compared to the default operation of GBRs. A second measurement campaign shows the estimation of mode shapes with this approach.

5.1 Methodology

The approach, also referred to below as mirror mode, uses the flat underside as a mirror to generate a secondary reflection on the ground opposite of the GBR. A reflector is placed on the ground to reflect the signal back on the same path as visualised in Figure 5.1. Although the reflector is not strictly necessary, it significantly improves the SNR leading to a smaller measurement uncertainty. The measurement in LOS is projected to the vertical axis similar to the conventional approach (see Equation 2.6). With the coordinates (x_1, y_1) of the respective mirror point, the vertical displacement Δd_v results from the displacement in LOS Δd :

$$\Delta d_v = \frac{\Delta d \sqrt{x_1^2 + y_1^2}}{2 y_1} \quad (5.1)$$

The factor $1/2$ is added since the GBR measures twice the displacement in LOS compared to the conventional approach. Calculating the unknown coordinates of the mirror point depends on some assumptions about the measurement setup. Most importantly, the angle of incidence is equal to the angle of reflection. Therefore, the following relation can be defined:

$$\frac{y_1}{x_1} = \frac{y_1 - y_2}{x_2 - x_1} \quad (5.2)$$

Furthermore, the x-axis of the local coordinate system is assumed to be parallel to the underside of the bridge. Hence, the y-axis value of the mirror point is not dependent on its x-value and can be measured. Since the coordinates of the reflector are also measured, the mirror point's x-value results from

$$x_1 = \frac{x_2 y_1}{2 y_1 - y_2} \quad (5.3)$$

Since the signal path is longer in mirror mode than in the conventional approach, the displacement measurement of the mirror point is located in a different range cell. The

distance d from the GBR to the reflector results from the coordinates of the mirror point and the reflector:

$$d = \sqrt{x_1^2 + y_1^2} + \sqrt{(x_2 - x_1)^2 + (y_2 - y_1)^2} \quad (5.4)$$

The conventional approach assumes that the horizontal components of the three-dimensional displacement vector are negligible in order to successfully project the measurement in LOS to the vertical axis. This assumption is not always true, as shown in Section 3.2.5. Since the GBR always measures a combination of the components, the vertical displacement cannot be correctly identified. In mirror mode, however, the horizontal components do not influence the measurements, since the mirrored signal on the underside of the bridge only experiences a vertical displacement.

Other than the projection, the processing of the measurements in mirror mode is equal to the processing of the conventional approach. However, clutter removal can become especially important because of static reflections. With its large beam width, the GBR signal is not only reflected on the mirror path but also directly from the reflector. This static reflection is located in a different range cell than the displacement of the mirror point. Thus, it is usually only relevant if more than one reflector is used. Clutter removal can also be influenced by a rotation of the bridge underside causing amplitude changes, which is further discussed in Section 3.2.3.

The measurement in mirror mode is expected to have a lower SNR because of the signal's multiple reflections. Then again, the mirror mode has an advantage in the context of variance propagation. Since twice the displacement is measured, the variance decreases for the discussed measurement setup. Consequently, the uncertainty of the vertical displacement is in the same order of magnitude as in the conventional approach.

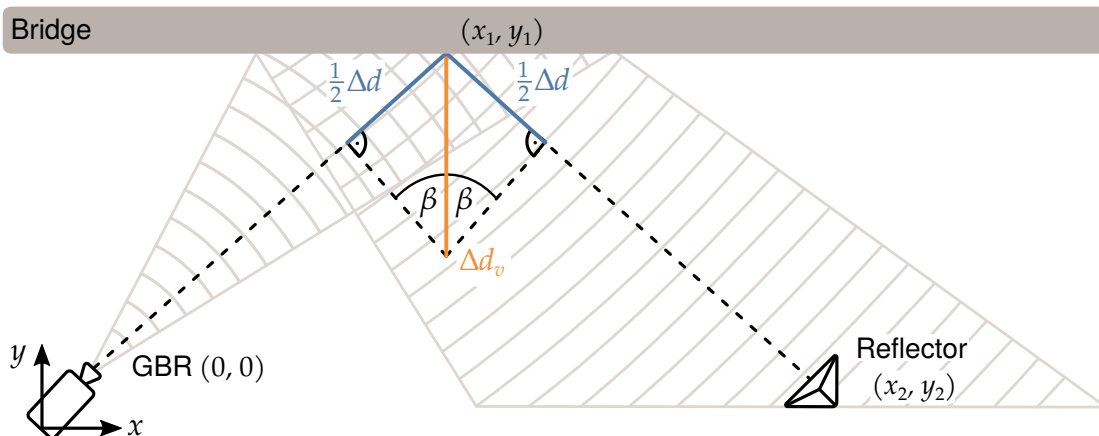


Figure 5.1: Measurement principle of the mirror mode.

5.2 Displacement Measurement and Validation With Reference Sensors

5.2.1 Measurement Setup

Measurements for validation of the mirror mode were carried out on 18 June 2019 at the Pulverhausstraße. As described in Section 2.3.4, the bridge at the Pulverhausstraße has four spans with two continuous beams. Both the underside of the bridge and the beams have a smooth concrete surface ensuring sufficient signal reflection from the GBR to the reflector and back. The measurements are performed at one of the inner spans under the eastern beam. GBR and reflector are positioned opposite of each other to measure displacements approximately at the middle of the beam, as shown in Figure 5.2. A second GBR and a TLS in profile mode provide reference measurements for validation of the proposed approach. The second GBR is placed under the centre of the beam facing the mirror point of the first GBR vertically. With a vertical orientation, the displacements in LOS do not require a projection and can be directly used as reference measurements. The TLS is operated in profile mode to produce two-dimensional point clouds with a repetition rate of up to 200 Hz. Similarly to the validation measurements at Maxau in Section 3.2.1, the TLS is positioned in line with the concrete beam to determine its vertical displacement. While the laser profile covers the entire length of the beam, only a small subset is used for comparison to the mirror mode. This subset with a length of about 0.5 m contains multiple measurements of angle and distance for each profile scan. These measurements are not reproducible over subsequent profiles and have to be averaged. Repeating the averaging for every profile scan results in the displacement time series of a representative point for the subset.

The respective sensor specifications are summarised in Table 5.1. Both GBRs typically reach a measurement precision of less than 0.1 mm and produce one displacement time series per range cell of 0.75 m. The TLS is operated at a sampling frequency of 50 Hz instead of the maximum 200 Hz to increase the point density, which improves measurement precision. At a cluster size of 0.5 m, the precision typically ranges between 0.1 mm and 0.2 mm. Directly comparing the vertical displacements requires synchronisation of the different sensor time information. Since hardware restrictions prohibit a synchronisation during the measurement campaign, the temporal offset is addressed by cross-correlating the displacement time series.

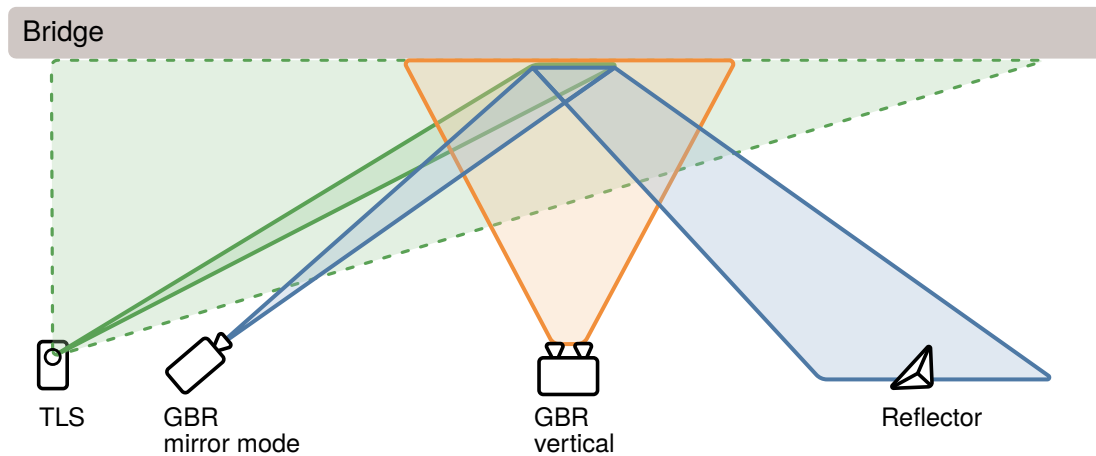


Figure 5.2: Measurement setup at the Pulverhausstraße on 18 June 2019 with an illustration of the sensors' field of view and footprint at the bridge underside.

Table 5.1: Specifications of the sensors applied at the Pulverhausstraße on 18 June 2019.

Sensor	Model	Sampling frequency	Typical precision	Size of range cell/point cluster
GBR mirror mode	IDS IBIS-FS	200 Hz	< 0.1 mm	0.75 m
GBR vertical	IDS IBIS-S	200 Hz	< 0.1 mm	0.75 m
TLS	Z+F 9012	50 Hz	0.1-0.2 mm	0.50 m

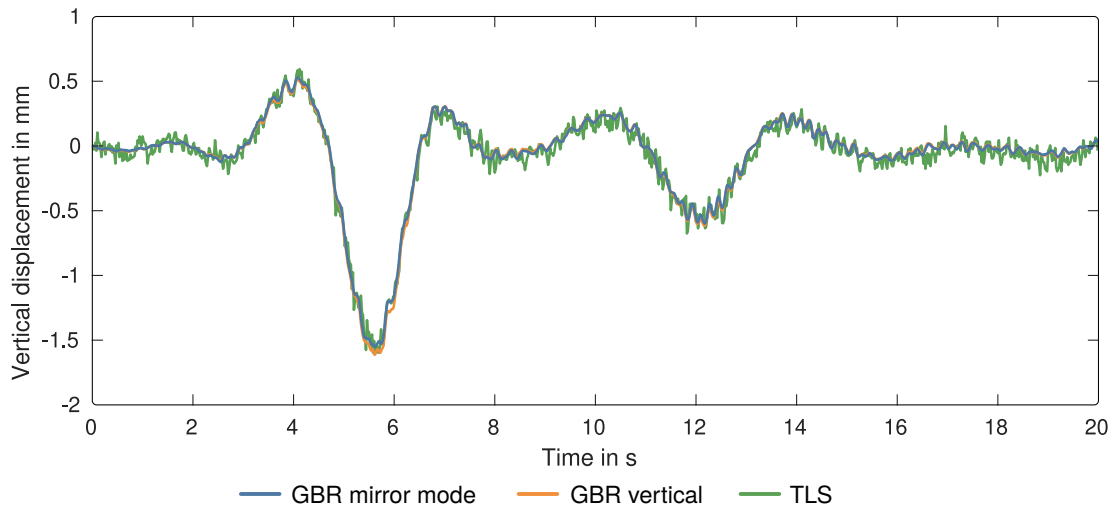


Figure 5.3: Vertical displacement during vehicle crossings measured by the two GBRs and the TLS.

5.2.2 Results and Discussion

The vertical bridge displacement at the mirror point is exemplarily shown in Figure 5.3 for all sensors. The shape of the displacement graph corresponds to crossings of a heavy vehicle followed by a lighter vehicle over a bridge with multiple fields. For the heavy vehicle, a positive displacement is measured at first, because the neighbouring bridge field is lifting the observed field. The displacement reaches its maximum negative value of -1.5 mm during the crossing of the heavy vehicle, while the light vehicle causes a displacement of -0.5 mm. All sensors show similar results, however a small deviation during the crossing of the heavy vehicle can be observed between the two GBRs. Figure 5.4a further visualises this deviation by subtracting the displacement in mirror mode from the displacement of the vertical GBR and the TLS. The maximum deviation is -0.1 mm and is approximately proportional to the absolute displacement as shown in Figure 5.4b. No systematic deviation can be observed between TLS and GBR in mirror mode, because the difference mainly contains measurement noise from the TLS with a standard deviation of 0.05 mm. The measurement precision of the GBRs can be estimated from the SNR. While the vertical GBR achieves an SNR of 60 dB, the SNR of the GBR in mirror mode is estimated at 46 dB. Since both estimates are above 35 dB, the highest measurement precision of 0.02 mm can be reached, as discussed in Section 2.1.2.

The displacements measured by the GBR in mirror mode correspond well with the displacements measured by the two reference sensors, apart from a small deviation between the two GBRs. The deviation most likely results from different measurement points on the

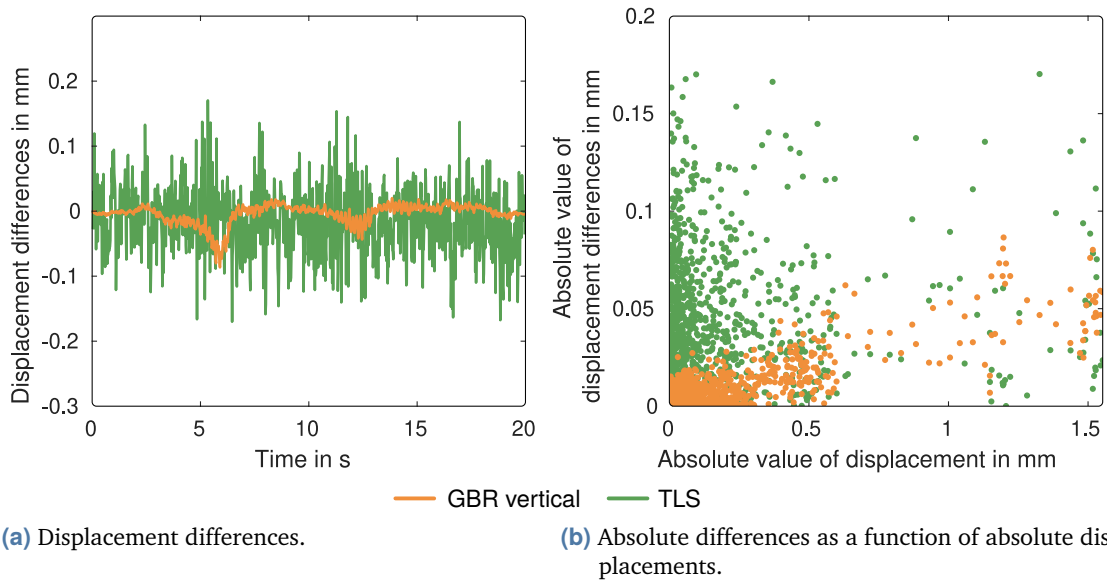


Figure 5.4: Vertical displacements of reference sensors subtracted by vertical displacements of the GBR in mirror mode.

bridge beam. In vertical orientation, the footprint of one range cell is much larger than in the default orientation or in mirror mode. The footprint increases from approximately 1 m to several metres. Generally, both GBRs were roughly positioned to measure the displacement in the middle of the beam, which is expected to have the highest displacement. A decrease in the maximum negative displacement for the vertical GBR would be expected, as it measures the (complex-valued) average of displacements from a larger area. However, this example shows an increase, which suggests that the mirror point is slightly offset from the point of the beam with the highest displacement. The footprint of the vertical GBR would still contain the point with the highest displacement resulting in the observed deviation. This assumption is supported by the proportionality of the absolute differences and the absolute displacements. Displacements of neighbouring bridge points generally have similar characteristics but are scaled differently, which can be observed with this systematic deviation. Although the TLS verifies the measurement principle, it cannot be used to further analyse the deviation between the two GBRs, since the standard deviation of its measurement noise is in the same range as the observed deviation.

Besides directly comparing the GBR in mirror mode with the reference sensors, a possible impact on measurement uncertainty has to be evaluated. While a significant drop in SNR due to the multiple reflections occurs, the measurement uncertainty is not decreased. However, for other measurement setups, a loss in precision is possible, especially if the distance between GBR and the bridge beam is higher. Likewise, additional reflectors for simultaneous measurement of multiple mirror points experience lower SNR, since

they are not placed in the centre of the signal beam and the signal attenuation increases. Lastly, there is no significant influence of the coordinate uncertainty of the targets, as has been shown for the measurements at Maxau (see Section 3.2.6). Since only one GBR is used, the possible errors in co-registration do not exist, and the reflectors' coordinates are determined with high accuracy.

5.3 Determination of Mode Shapes

The mirror mode significantly reduces the occurrence of systematic deviations since the measurements are not influenced by horizontal components, and vertical displacements directly result from measurements with one GBR. These benefits could significantly improve the determination of mode shapes. However, the evaluable area of the bridge is very limited due to the high signal attenuation at greater beam widths. A common approach in modal analysis uses multiple measurement setups to overcome limited spatial resolution and can be utilised together with the mirror mode.

Increasing spatial resolution without increasing the total number of sensors is possible by dividing the sensors into two groups. The stationary sensors perform measurements at the same positions throughout the entire measurement campaign, while the remaining sensors assume varying positions to refine the spatial resolution. Since the excitation of the bridge changes over time, the measurements of the moving sensors cannot be used directly for mode shape estimation. Instead, the results are rescaled by the stationary sensors. The scaling can be integrated into the mode shape estimation at different stages. Parloo [73], as referenced by Magalhães [52], distinguishes between three integration methods: Post Separate Estimation Re-Scaling (PoSER), Post Global Estimation Re-Scaling (PoGER), and Pre Global Estimation Re-Scaling (PreGER). PoGER and PreGER calculate spectral or correlation matrices for the different setups and aggregate them in a global matrix. The mode shapes are then estimated from the unscaled global matrix and scaled afterwards in the case of PoGER, whereas PreGER first scales the global matrix before estimating the mode shapes.

The PoSER method separately estimates the mode shape components for each setup and scales them appropriately afterwards. Assuming the i -th mode Ω is observed with the measurement setups A and B , where B is the reference setup. The mode shape

components from the moving sensors are then scaled with a factor ρ calculated from the components of the stationary sensors [52]:

$$\rho_i = \frac{(\Omega_i^A)^H \cdot \Omega_i^B}{(\Omega_i^A)^H \cdot \Omega_i^A} \quad (5.5)$$

In the following, this method is applied to displacement measurements with two GBRs operated in mirror mode.

5.3.1 Measurement Setup

Measurements for the determination of mode shapes took place on 18 August 2022 at the Pulverhausstraße (see Section 2.3.4). Similar to the validation measurements of the mirror mode, the eastern beam of an inner bridge span is investigated. One GBR is used as the stationary sensor measuring vertical displacements at the approximate midpoint of the beam. The second GBR measures vertical displacements at varying positions in four different setups. Figure 5.5a exemplarily shows setup A with the stationary sensor in orange and the moving sensor in blue. Displacements are measured at one position for each sensor. For other setups, as shown in Figure 5.5b, several reflectors could be placed opposite of the moving GBR resulting in one to three mirror points for each setup. Displacements are measured for 30 min at each setup to reliably determine mode shapes with the FDD.

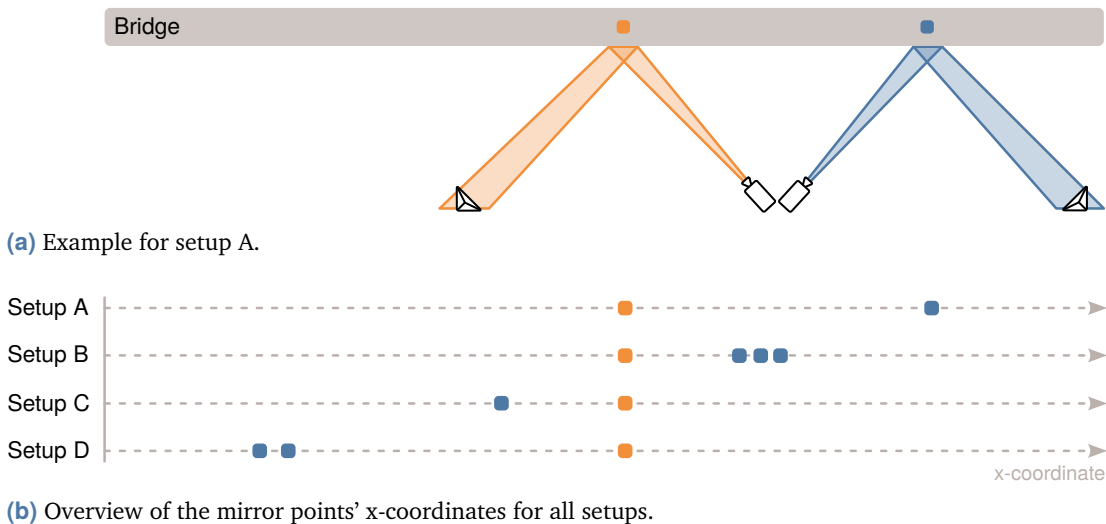


Figure 5.5: Measurement setups at the Pulverhausstraße on 18 August 2022 with the stationary GBR in orange and the moving GBR in blue.

A second measurement campaign provides a qualitative comparison of this approach with the conventional displacement measurement from a single GBR. The GBR is setup as discussed in Section 2.1.1 and measures displacements in LOS at several points on the bridge. Signal reflection is provided by corner reflectors installed at the bridge beams. The displacements are projected to the vertical axis by their distance and height to the sensor, as discussed in Equation 2.6.

5.3.2 Results and Discussion

The mode shape of the first natural frequency from the mirror mode measurements is estimated by FDD with a window size of 5 min. Figure 5.6 shows the mean and standard deviation of the six estimations. Since the component of the stationary sensor is used for scaling the components of the moving sensor, it is fixed at the arbitrary value of -1 with a standard deviation of 0. Scaling of the mode shape is defined arbitrarily because the excitation source is unknown in OMA. Generally, the result shows typical behaviour for a mode shape of the first natural frequency for this bridge type. However, one irregularity is visible in the results of setup B. The component at approximately 22 m forms a small bend together with the other two components of setup B. Though it does not have a higher standard deviation than the nearby components. The irregularity likely results from a systematic deviation introduced by the GBR processing, which can be analysed by the additionally shown standard deviation of the vertical displacements. This standard deviation is calculated as shown in Section 3.1.5 and enables an assessment of the measurement uncertainty during processing. Since it is higher than the standard deviations of the nearby components, its clutter estimation likely also has a higher uncertainty resulting in a systematic deviation. In contrast to conventional sensors such as acceleration or strain sensors, systematic deviations are more likely to occur individually for each component instead of influencing the entire mode shape. However, this analysis shows that the uncertainty information enables an additional assessment of the resulting individual components and can possibly identify these deviations. An assessment of the clutter removal's accuracy to analyse this deviation would further benefit the identification, as discussed similarly in Section 3.1.5.

As comparison to the mirror mode result, Figure 5.7 shows the mode shape estimated from displacement measurements of a single GBR. The result covers a smaller range of the bridge but has a higher spatial resolution than the mirror mode result. Additionally, the standard deviation of the mode shape itself is smaller. The smaller values are expected since the overall measurement duration is the same between both approaches and it does not have to be divided between the different setups. Consequently, the

one-dimensional approach determines mode shapes with higher precision but not with a smaller uncertainty, as can be shown by the slight asymmetry of the mode shape. This asymmetry likely results from horizontal displacement components, which influence the measurements in LOS. Assuming that the horizontal component is equal throughout the bridge, the various targets would experience different systematic deviations depending on their distance from the GBR resulting in an asymmetric mode shape. A two-dimensional measurement setup could certainly reduce these errors. However, the uncertainty would increase significantly as discussed in Section 3.2.6. Figure 5.7 shows an already comparatively high displacement uncertainty in the one-dimensional approach. With the two-dimensional projection, the spatial coverage of the bridge would further decrease due to the high uncertainty.

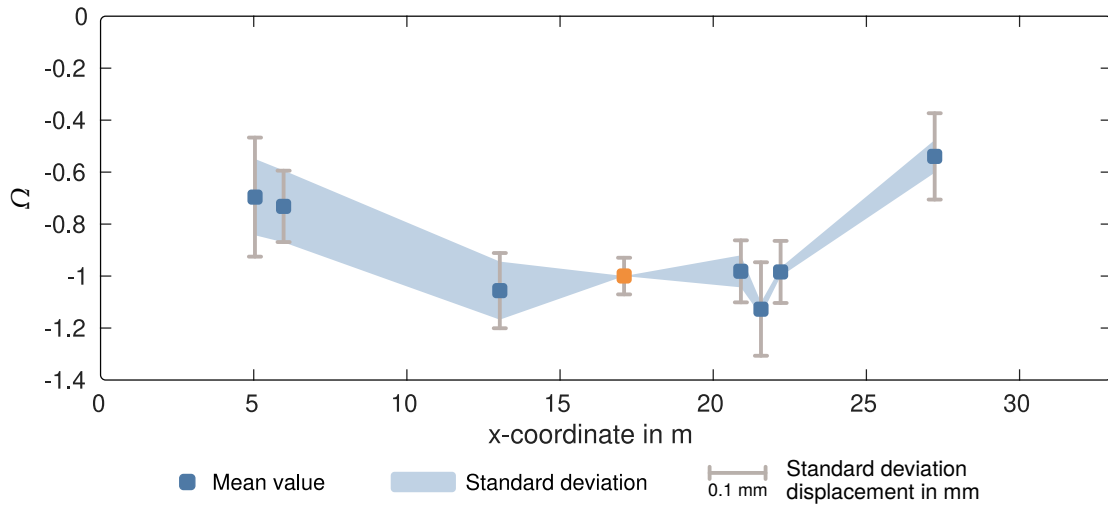


Figure 5.6: Mode shape from the mirror mode measurements with the standard deviation of the mode and the standard deviation of the displacement measurements.

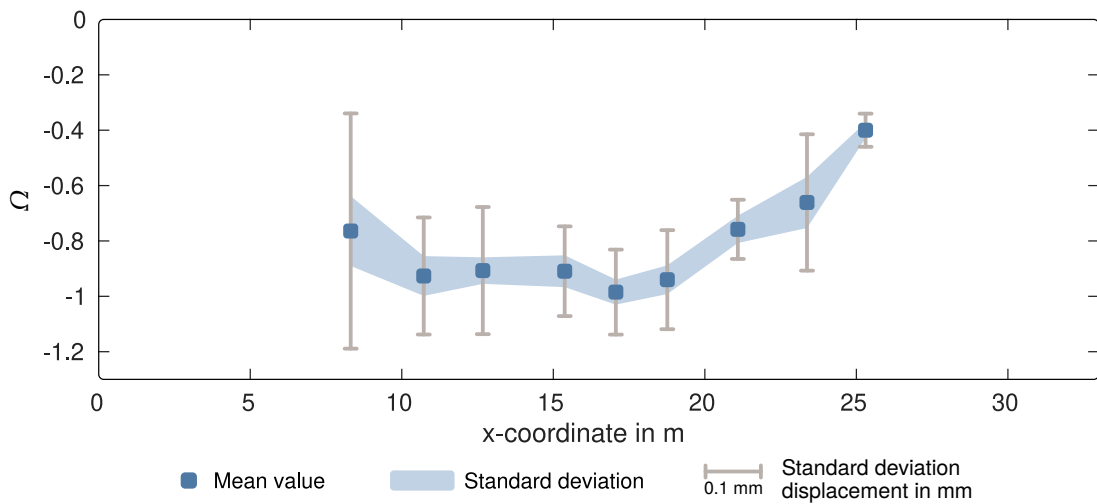


Figure 5.7: Mode shape from one-dimensional measurements with the standard deviation of the mode and the standard deviation of the displacement measurements.

5.4 Conclusion

An alternative measurement approach is proposed, which uses the flat underside of a bridge to mirror the GBR signal towards reflectors on the ground opposite of the sensor. The most important advantage of the mirror mode over the conventional approach is the reduction of systematic deviations. For example, mirroring the signal completely eliminates the influence of horizontal components on the measurement of the vertical displacement. Uncertain target coordinates constitute a second source of systematic deviations in the conventional approach, as shown by the measurements at Maxau in Section 3.2.6. For the mirror mode, this uncertainty is significantly reduced since the coordinates of the reflectors can be determined much more precisely compared to the bridge's naturally reflective features. The reflectors are a second advantage of the mirror mode since no fixed installation is necessary, and measurements are enabled at a wider range of bridges.

The principle is successfully validated with a second GBR operated in a vertical orientation and a TLS. A small deviation between the vertical GBR and the mirror mode likely results from the large footprint of the vertical GBR. Both approaches enable the determination of vertical displacements without the influence of horizontal components. However, the mirror mode's footprint is much smaller, which reduces the target's coordinate uncertainty. In addition, the possibility of measuring displacements of multiple targets is retained. The TLS as a second independent validation sensor agrees well with the mirror mode. However, further assessment of the mirror mode's accuracy beyond a simple validation of the measurement principle requires a sensor with higher accuracy and lower measurement noise than the TLS.

After validation, the mode shape of the first natural frequency is successfully determined with the mirror mode. The combination of multiple measurement setups enables the determination over a wider range along the bridge compared to one fixed setup. A systematic deviation in one of the mirror points can be explained by an inaccurate clutter estimation. As discussed in Section 3.1.5, the estimation would benefit from an additional uncertainty assessment.

Conclusion and Outlook

The objective of this thesis is to evaluate and improve the accuracy of GBR measurements. A comprehensive assessment of the GBR's capabilities also increases the significance and reliability of damage detection approaches. Three research goals are defined to achieve this objective.

Research Goal 1 The first research goal concerns the GBR's limited accuracy compared to other sensors, which is observed by several studies. Static clutter and the influence of other displacement components are identified as the main causes of systematic deviations. The estimation of static clutter is significantly improved by introducing a weight matrix, which biases the contribution of specific measurements to this estimation. Measurements during vehicle crossings are assigned a higher weight than background noise, which improves the estimation results. The measurement campaign at Maxau has shown that static clutter represents a large portion of the received signal, especially for targets with small amplitudes. Although clutter removal might introduce new uncertainties, its application is generally beneficial. Similar systematic deviations are caused by additional displacement components, which prevent the accurate reconstruction of vertical displacements. Especially the measurements at Maxau show the impact of the three-dimensional projection on the accuracy of GBR compared to TLS. As a consequence, GBR measurements should generally implement this principle unless the existence of other displacement components can be confidently ruled out in advance. The comparison with TLS still shows some remaining differences resulting from uncertainties in the clutter estimation and the target coordinates. With this example, the disadvantage of the GBR's low spatial resolution becomes apparent and should always be considered, for example, in an uncertainty assessment.

Research Goal 2 The second research goal is to achieve a reliable assessment of the measurement uncertainty, especially in the context of the proposed additional processing steps. Estimation results for two measurement campaigns show the importance of this assessment. All processing steps significantly influence the uncertainty, and the initial estimate from the amplitude's SNR insufficiently describes the actual uncertainty. While every processing step should be considered in this assessment, the most significant

influence originates from the projection. In this context, the setups of the discussed measurement campaigns are not optimal. For example, the measurements at Maxau would have smaller uncertainties if the spatial separation in height or horizontal distance between the GBRs had been maximised. However, there are several other constraints to consider such as the sensors' field of view or signal reflection from bridge features. Since the uncertainty of the projection only depends on the geometric relations, an uncertainty assessment could also be performed beforehand to determine the best possible measurement setup with these constraints taken into consideration.

Research Goal 3 The third research goal is to analyse the potential of the resulting displacement measurements concerning the estimation of damage-sensitive features. An approach to damage detection is shown, which estimates natural frequencies from the damped vibration after a vehicle crossing. With the proposed least squares approach, it is possible to evaluate each crossing while considering the individual uncertainty of separate targets. As a result, the influence of temperature changes on natural frequencies can be estimated more reliably compared to an approach using the FDD. Separate evaluation of vehicle crossings also enables the distinction between two classes of vehicle mass, revealing a residual influence of mass on natural frequencies. The approach is not applicable to all or even most bridges since an uninterrupted vibration is required after each crossing. However, it is relevant for small bridges, which constitute a large part of bridges in the German road network. Monitoring of these bridges is simplified first through the GBR's comparatively fast measurement setup, but also through the reduced measurement duration required by the least squares approach. For the determination of mode shapes, an indirect measurement setup is proposed and validated with simultaneous TLS measurements. The mirror mode's measurement of the vertical displacement is not influenced by other components and thus reduces the occurrence of systematic deviations. Consequently, the reduction of deviations increases the sensitivity of mode shapes since smaller uncertainties lead to earlier detection of damage. The proposed measurement setup with two GBRs shown at the Pulverhausstraße is certainly complex and time-consuming, but also provides more flexibility regarding the positioning of measurement points and the aforementioned smaller uncertainty compared to the conventional approach.

Generally, it has been shown that GBR can achieve a measurement uncertainty similar to that of other sensor technologies if additional processing steps and setup-specific influences are considered. However, the differences to TLS measurements also demonstrate further potential for improvements. These differences are partly caused by an inaccurate

clutter estimation, which results from varying amplitude values. If this variation is deterministic or highly correlated with displacement, the functional model could be adapted. As a first step, however, inaccurate estimation results should be detected by a test for goodness of fit similar to the frequency estimation in Section 4.2.3. Additionally, the uncertainty of clutter estimation should be quantified and included in the overall measurement uncertainty. Incorrect or uncertain target coordinates are another possible source for differences to a reference measurement and could be addressed either through better visualisation of the cause or through technological advancements. The cause could be visualised, for example, with a model of the bridge and its reflective features, which is obtained through a three-dimensional laser scan. A simulation of the range cells projected onto this model would enable an a priori assessment of the signal footprint and the targets' uncertainties. Sensor positions could be planned accordingly. Technological advancements, on the other hand, could directly decrease the coordinate uncertainty. For example, a higher signal bandwidth increases the range resolution. Systems operating in the W-band achieve a bandwidth of several gigahertz, leading to resolutions in the centimetre range. Furthermore, these systems also implement the MIMO principle with several antennas, which enables an additional angular resolution. Recent studies have shown the application of MIMO GBR in the W-band but also in the K_u -band for bridge displacement measurement [9, 59, 105].

In addition to accuracy improvements, the estimation of features from GBR measurements also provides opportunities for further improvement. Studies have shown that the measurements usually have sufficient SNR to determine multiple modes [29, 50]. Consequently, natural frequencies could be estimated for higher modes with the least squares approach and an adapted bandpass filter. Estimation of the temperature-frequency relationship could also be improved by additional sensors that determine the temperature distribution throughout the bridge. Temperature measurements, which better represent the actual behaviour of the bridge, could explain the non-linear relationship in Schneck-enlohe. The estimation of mode shapes would benefit from additional validation. While the underlying principle of the mirror mode is already successfully validated with a TLS, the proposed sequential measurement setups still entail possible error sources, as shown by the irregularity in the mode shape. A TLS could provide mode shapes with sufficient spatial resolution and accuracy to be used as a reference for GBR.

Bibliography

- [1] S. Ahn, W. Rauh and H.-J. Warnecke. “Least-squares orthogonal distances fitting of circle, sphere, ellipse, hyperbola, and parabola”. In: *Pattern Recognition* 34.12 (2001). DOI: [10.1016/s0031-3203\(00\)00152-7](https://doi.org/10.1016/s0031-3203(00)00152-7).
- [2] M. Alba et al. “Measurement of Dam Deformations by Terrestrial Interferometric Techniques”. In: *International Archives of the Photogrammetry, Remote Sensing and Spatial Information Sciences* 37 (2008), pp. 133–139.
- [3] R. E. Alva et al. “Dynamic Monitoring of a Mid-Rise Building by Real-Aperture Radar Interferometer: Advantages and Limitations”. In: *Remote Sensing* 12.6 (2020). DOI: [10.3390/rs12061025](https://doi.org/10.3390/rs12061025).
- [4] R. Amar, M. Alae-Kerahroodi and M. R. B. Shankar. “FMCW-FMCW Interference Analysis in mm-Wave Radars; An indoor case study and validation by measurements”. In: *21st International Radar Symposium (IRS)*. IEEE, June 2021. DOI: [10.23919/IRS51887.2021.9466178](https://doi.org/10.23919/IRS51887.2021.9466178).
- [5] D. Anastasopoulos, G. D. Roeck and E. P. B. Reynders. “One-year operational modal analysis of a steel bridge from high-resolution macrostrain monitoring: Influence of temperature vs. retrofitting”. In: *Mechanical Systems and Signal Processing* 161 (Dec. 2021). DOI: [10.1016/j.ymssp.2021.107951](https://doi.org/10.1016/j.ymssp.2021.107951).
- [6] M. Arnold, M. Hoyer and S. Keller. “Convolutional Neural Networks For Detecting Bridge Crossing Events With Ground-Based Interferometric Radar Data”. In: *ISPRS Annals of the Photogrammetry, Remote Sensing and Spatial Information Sciences* V-1-2021 (June 2021), pp. 31–38. DOI: [10.5194/isprs-annals-V-1-2021-31-2021](https://doi.org/10.5194/isprs-annals-V-1-2021-31-2021).
- [7] S. Artese and G. Nico. “TLS and GB-RAR Measurements of Vibration Frequencies and Oscillation Amplitudes of Tall Structures: An Application to Wind Towers”. In: *Applied Sciences* 10.7 (2020). DOI: [10.3390/app10072237](https://doi.org/10.3390/app10072237).
- [8] C. Atzeni et al. “Remote Survey of the Leaning Tower of Pisa by Interferometric Sensing”. In: *IEEE Geoscience and Remote Sensing Letters* 7.1 (Jan. 2010), pp. 185–189. DOI: [10.1109/lgrs.2009.2030903](https://doi.org/10.1109/lgrs.2009.2030903).
- [9] A. Baumann-Ouyang, J. Butt and A. Wieser. “Bridge deformations during train passage: monitoring multiple profiles using concurrently operating MIMO-SAR sensors”. In: *5th Joint International Symposium on Deformation Monitoring (JISDM)*. June 2022. DOI: [10.4995/JISDM2022.2022.13620](https://doi.org/10.4995/JISDM2022.2022.13620).
- [10] R. Brincker, L. Zhang and P. Andersen. “Modal Identification from Ambient Responses using Frequency Domain Decomposition”. In: *IMAC 18: Proceedings of the International Modal Analysis Conference (IMAC)*. San Antonio, USA, Feb. 2000, pp. 625–630.
- [11] J. M. W. Brownjohn, Y. Xu and D. Hester. “Vision-Based Bridge Deformation Monitoring”. In: *Frontiers in Built Environment* 3 (Apr. 2017). DOI: [10.3389/fbuil.2017.00023](https://doi.org/10.3389/fbuil.2017.00023).

- [12] Bundesministerium für Verkehr und digitale Infrastruktur. *Stand der Modernisierung von Brücken der Bundesfernstraßen*. Berlin, Dec. 2020.
- [13] T. Carlà et al. “Combination of GNSS, satellite InSAR, and GBInSAR remote sensing monitoring to improve the understanding of a large landslide in high alpine environment”. In: *Geomorphology* 335 (June 2019), pp. 62–75. DOI: [10.1016/j.geomorph.2019.03.014](https://doi.org/10.1016/j.geomorph.2019.03.014).
- [14] A. Castellano et al. “Structural health monitoring of a historic masonry bell tower by radar interferometric measurements”. In: *IEEE Workshop on Environmental, Energy, and Structural Monitoring Systems (EESMS)*. IEEE, June 2018. DOI: [10.1109/eesms.2018.8405824](https://doi.org/10.1109/eesms.2018.8405824).
- [15] P. Castellini, M. Martarelli and E. P. Tomasini. “Laser Doppler Vibrometry: Development of advanced solutions answering to technology’s needs”. In: *Mechanical Systems and Signal Processing* 20.6 (Aug. 2006), pp. 1265–1285. DOI: [doi:10.1016/j.ymsp.2005.11.015](https://doi.org/10.1016/j.ymsp.2005.11.015).
- [16] N. Chernov and C. Lesort. “Least Squares Fitting of Circles”. In: *Journal of Mathematical Imaging and Vision* 23.3 (2005). DOI: [10.1007/s10851-005-0482-8](https://doi.org/10.1007/s10851-005-0482-8).
- [17] F. Coppi et al. “A Software Tool for Processing the Displacement Time Series Extracted from Raw Radar Data”. In: *AIP Conference Proceedings*. AIP, 2010. DOI: [10.1063/1.3455458](https://doi.org/10.1063/1.3455458).
- [18] P. Cornwell et al. “Environmental Variability of Modal Properties”. In: *Experimental Techniques* 23.6 (Nov. 1999), pp. 45–48. DOI: [10.1111/j.1747-1567.1999.tb01320.x](https://doi.org/10.1111/j.1747-1567.1999.tb01320.x).
- [19] J. C. Dainty. *Laser Speckle and Related Phenomena*. 2nd ed. Topics in applied physics; 9. Berlin: Springer, 1984.
- [20] D. Dei, D. Mecatti and M. Pieraccini. “Static Testing of a Bridge Using an Interferometric Radar: The Case Study of “Ponte degli Alpini”, Belluno, Italy”. In: *The Scientific World Journal* (2013). DOI: [10.1155/2013/504958](https://doi.org/10.1155/2013/504958).
- [21] Y. Deng et al. “3-D Deformation Measurement Based on Three GB-MIMO Radar Systems: Experimental Verification and Accuracy Analysis”. In: *IEEE Geoscience and Remote Sensing Letters* (2020). DOI: [10.1109/LGRS.2020.3014342](https://doi.org/10.1109/LGRS.2020.3014342).
- [22] DIN 1076. *Ingenieurbauwerke im Zuge von Straßen und Wegen - Überwachung und Prüfung*. Standard. Nov. 1999.
- [23] Y. Ding and A. Li. “Temperature-induced Variations of Measured Modal Frequencies of Steel Box Girder for a Long-span Suspension Bridge”. In: *International Journal of Steel Structures* 11.2 (June 2011), pp. 145–155. DOI: [10.1007/s13296-011-2004-4](https://doi.org/10.1007/s13296-011-2004-4).
- [24] J. Erdélyi, A. Kopáčík and P. Kyrinovič. “Spatial Data Analysis for Deformation Monitoring of Bridge Structures”. In: *Applied Sciences* 10.23 (Dec. 2020), p. 8731. DOI: [10.3390/app10238731](https://doi.org/10.3390/app10238731).
- [25] W. Fan and P. Qiao. “Vibration-based Damage Identification Methods: A Review and Comparative Study”. In: *Structural Health Monitoring* 10.1 (Apr. 2010), pp. 83–111. DOI: [10.1177/1475921710365419](https://doi.org/10.1177/1475921710365419).

- [26] A. Firus et al. “Microwave Interferometry Measurements for Railway-specific Applications”. In: *Proceedings of the 6th International Conference on Computational Methods in Structural Dynamics and Earthquake Engineering (COMPDYN 2015)*. Institute of Structural Analysis and Antiseismic Research School of Civil Engineering National Technical University of Athens (NTUA) Greece, 2017. DOI: [10.7712/120117.5600.17334](https://doi.org/10.7712/120117.5600.17334).
- [27] C. Gentile. “Application of Microwave Remote Sensing to Dynamic Testing of Stay-Cables”. In: *Remote Sensing* 2.1 (Dec. 2009), pp. 36–51. DOI: [10.3390/rs2010036](https://doi.org/10.3390/rs2010036).
- [28] C. Gentile and G. Bernardini. “An interferometric radar for non-contact measurement of deflections on civil engineering structures: laboratory and full-scale tests”. In: *Structure and Infrastructure Engineering* 6.5 (June 2009), pp. 521–534. DOI: [10.1080/15732470903068557](https://doi.org/10.1080/15732470903068557).
- [29] C. Gentile and G. Bernardini. “Output-only modal identification of a reinforced concrete bridge from radar-based measurements”. In: *NDT & E International* 41.7 (Oct. 2008), pp. 544–553. DOI: [10.1016/j.ndteint.2008.04.005](https://doi.org/10.1016/j.ndteint.2008.04.005).
- [30] C. Gentile and G. Bernardini. “Radar-based measurement of deflections on bridges and large structures”. In: *European Journal of Environmental and Civil Engineering* 14.4 (Apr. 2010), pp. 495–516. DOI: [10.1080/19648189.2010.9693238](https://doi.org/10.1080/19648189.2010.9693238).
- [31] V. Gikas. “Ambient vibration monitoring of slender structures by microwave interferometer remote sensing”. In: *Journal of Applied Geodesy* 6.3-4 (Jan. 2012). DOI: [10.1515/jag-2012-0029](https://doi.org/10.1515/jag-2012-0029).
- [32] J. Guo et al. “Measuring Micrometer-Level Vibrations with mmWave Radar”. In: *IEEE Transactions on Mobile Computing* (2021). DOI: [10.1109/tmc.2021.3118349](https://doi.org/10.1109/tmc.2021.3118349).
- [33] Q. Han et al. “Structural health monitoring research under varying temperature condition: a review”. In: *Journal of Civil Structural Health Monitoring* 11.1 (Oct. 2020), pp. 149–173. DOI: [10.1007/s13349-020-00444-x](https://doi.org/10.1007/s13349-020-00444-x).
- [34] K. T. Hsu, C. C. Cheng and C. H. Chiang. “Long-Term Monitoring of Two Highway Bridges Using Microwave Interferometer-Case Studies”. In: *2016 16th International Conference on Ground Penetrating Radar (GPR)*. IEEE, June 2016. DOI: [10.1109/icgpr.2016.7572669](https://doi.org/10.1109/icgpr.2016.7572669).
- [35] J. Hu et al. “Dynamic Vibration Characteristics Monitoring of High-Rise Buildings by Interferometric Real-Aperture Radar Technique: Laboratory and Full-Scale Tests”. In: *IEEE Sensors Journal* 18.15 (Aug. 2018), pp. 6423–6431. DOI: [10.1109/jsen.2018.2825331](https://doi.org/10.1109/jsen.2018.2825331).
- [36] J. Huang et al. “Measurement method and recent progress of vision-based deflection measurement of bridges: a technical review”. In: *Optical Engineering* 61.07 (July 2022). DOI: [10.1117/1.OE.61.7.070901](https://doi.org/10.1117/1.OE.61.7.070901).
- [37] Q. Huang et al. “Ground-Based Radar Interferometry for Monitoring the Dynamic Performance of a Multitrack Steel Truss High-Speed Railway Bridge”. In: *Remote Sensing* 12.16 (Aug. 2020), p. 2594. DOI: [10.3390/rs12162594](https://doi.org/10.3390/rs12162594).
- [38] L. Iannini and A. M. Guarnieri. “Atmospheric Phase Screen in Ground-Based Radar: Statistics and Compensation”. In: *IEEE Geoscience and Remote Sensing Letters* 8.3 (2011). DOI: [10.1109/lgrs.2010.2090647](https://doi.org/10.1109/lgrs.2010.2090647).

- [39] IDS Ingegneria Dei Sistemi S.p.A. *Static and dynamic testing of bridges: use of IBIS-FS for measuring deformation and identifying modal analysis parameters*. Tech. rep. 2016.
- [40] C. Jin et al. “Structural damage detection for in-service highway bridge under operational and environmental variability”. In: *Sensors and Smart Structures Technologies for Civil, Mechanical, and Aerospace Systems*. SPIE, Mar. 2015. DOI: [10.1117/12.2084384](https://doi.org/10.1117/12.2084384).
- [41] B. Kafle et al. “Monitoring the Dynamic Behavior of The Merlynston Creek Bridge Using Interferometric Radar Sensors and Finite Element Modeling”. In: *International Journal of Applied Mechanics* 09.01 (Jan. 2017). DOI: [10.1142/s175882511750003x](https://doi.org/10.1142/s175882511750003x).
- [42] C.-Y. Kim et al. “Effect of Vehicle Mass on the Measured Dynamic Characteristics of Bridges from Traffic-Induced Vibration Test”. In: *Proceedings of SPIE The International Society of Optical Engineering*. 2001.
- [43] P. Kot et al. “Recent Advancements in Non-Destructive Testing Techniques for Structural Health Monitoring”. In: *Applied Sciences* 11.6 (Mar. 2021), p. 2750. DOI: [10.3390/app11062750](https://doi.org/10.3390/app11062750).
- [44] P. Kuras et al. “GB-SAR in the Diagnosis of Critical City Infrastructure—A Case Study of a Load Test on the Long Tram Extradosed Bridge”. In: *Remote Sensing* 12.20 (Oct. 2020), p. 3361. DOI: [10.3390/rs12203361](https://doi.org/10.3390/rs12203361).
- [45] C. Li et al. “A Noncontact FMCW Radar Sensor for Displacement Measurement in Structural Health Monitoring”. In: *Sensors* 15.4 (Mar. 2015), pp. 7412–7433. DOI: [10.3390/s150407412](https://doi.org/10.3390/s150407412).
- [46] C. Liu and J. T. DeWolf. “Effect of Temperature on Modal Variability of a Curved Concrete Bridge under Ambient Loads”. In: *Journal of Structural Engineering* 133.12 (Dec. 2007), pp. 1742–1751. DOI: [10.1061/\(ASCE\)0733-9445\(2007\)133:12\(1742\)](https://doi.org/10.1061/(ASCE)0733-9445(2007)133:12(1742)).
- [47] X. Liu et al. “Improved Data-Driven Stochastic Subspace Identification with Autocorrelation Matrix Modal Order Estimation for Bridge Modal Parameter Extraction Using GB-SAR Data”. In: *Buildings* 12.2 (Feb. 2022), p. 253. DOI: [10.3390/buildings12020253](https://doi.org/10.3390/buildings12020253).
- [48] X. Liu et al. “Measurement of Long-Term Periodic and Dynamic Deflection of the Long-Span Railway Bridge Using Microwave Interferometry”. In: *IEEE Journal of Selected Topics in Applied Earth Observations and Remote Sensing* 8.9 (Sept. 2015), pp. 4531–4538. DOI: [10.1109/jstars.2015.2464240](https://doi.org/10.1109/jstars.2015.2464240).
- [49] G. Luzi et al. “Ground-Based Radar Interferometry for Landslides Monitoring: Atmospheric and Instrumental Decorrelation Sources on Experimental Data”. In: *IEEE Transactions on Geoscience and Remote Sensing* 42.11 (Nov. 2004), pp. 2454–2466. DOI: [10.1109/tgrs.2004.836792](https://doi.org/10.1109/tgrs.2004.836792).
- [50] G. Luzi, M. Crosetto and E. Fernández. “Radar Interferometry for Monitoring the Vibration Characteristics of Buildings and Civil Structures: Recent Case Studies in Spain”. In: *Sensors* 17.4 (Mar. 2017), p. 669. DOI: [10.3390/s17040669](https://doi.org/10.3390/s17040669).
- [51] G. Luzi, O. Monserrat and M. Crosetto. “The Potential of Coherent Radar to Support the Monitoring of the Health State of Buildings”. In: *Research in Nondestructive Evaluation* 23.3 (July 2012), pp. 125–145. DOI: [10.1080/09349847.2012.660241](https://doi.org/10.1080/09349847.2012.660241).
- [52] F. M. R. L. de Magalhães. “Operational modal analysis for testing and monitoring of bridges and special structures”. PhD thesis. Universidade do Porto (Portugal), 2010.

- [53] D. Mecatti et al. “A Novel Ground Based Multi Bistatic Radar for Interferometric Measurement of Displacement Vector”. In: *IEEE International Geoscience and Remote Sensing Symposium, IGARSS 2011*. Vancouver, Canada: IEEE, July 2011.
- [54] Metasensing. *FastGBSAR User Manual*. 26th July 2019.
- [55] N. Meyer et al. “Vibration monitoring of a bridge using 2D profile laser scanning: Lessons learned from the comparison of two spatio-temporal processing strategies”. In: *5th Joint International Symposium on Deformation Monitoring (JISDM)*. Jan. 2022.
- [56] L. Miccinesi, A. Beni and M. Pieraccini. “Multi-Monostatic Interferometric Radar for Bridge Monitoring”. In: *Electronics* 10.3 (Jan. 2021). DOI: [10.3390/electronics10030247](https://doi.org/10.3390/electronics10030247).
- [57] L. Miccinesi and M. Pieraccini. “Bridge Monitoring by a Monostatic/Bistatic Interferometric Radar Able to Retrieve the Dynamic 3D Displacement Vector”. In: *IEEE Access* 8 (2020). DOI: [10.1109/access.2020.3039381](https://doi.org/10.1109/access.2020.3039381).
- [58] L. Miccinesi et al. “Multi-Monostatic Interferometric Radar with Radar Link for Bridge Monitoring”. In: *Electronics* 10.22 (Nov. 2021). DOI: [10.3390/electronics10222777](https://doi.org/10.3390/electronics10222777).
- [59] L. Miccinesi et al. “W-band MIMO GB-SAR for Bridge Testing/Monitoring”. In: *Electronics* 10.18 (Sept. 2021), p. 2261. DOI: [10.3390/electronics10182261](https://doi.org/10.3390/electronics10182261).
- [60] C. Michel and S. Keller. “Advancing Ground-Based Radar Processing for Bridge Infrastructure Monitoring”. In: *Sensors* 21.6 (Mar. 2021), p. 2172. DOI: [10.3390/s21062172](https://doi.org/10.3390/s21062172).
- [61] C. Michel and S. Keller. “Determining and Investigating the Variability of Bridges’ Natural Frequencies with Ground-Based Radar”. In: *Applied Sciences* 12.11 (May 2022), p. 5354. DOI: [10.3390/app12115354](https://doi.org/10.3390/app12115354).
- [62] A. Michelini and F. Coppi. “Deformation vector measurement by means of ground based interferometric radar system”. In: *Active and Passive Microwave Remote Sensing for Environmental Monitoring*. SPIE Remote Sensing. Warsaw, Poland: SPIE, Oct. 2017. DOI: [10.1117/12.2279147](https://doi.org/10.1117/12.2279147).
- [63] H. Naraniecki and S. Marx. “Zustandsentwicklung und -prognose von Eisenbahnbrücken”. In: *60. Forschungskolloquium des Deutschen Ausschusses für Stahlbeton*. Institutionelles Repositorium der Leibniz Universität Hannover, 2019. DOI: [10.15488/5532](https://doi.org/10.15488/5532).
- [64] H. H. Nassif, M. Gindy and J. Davis. “Comparison of laser Doppler vibrometer with contact sensors for monitoring bridge deflection and vibration”. In: *NDT & E International* 38.3 (Apr. 2005), pp. 213–218. DOI: [10.1016/j.ndteint.2004.06.012](https://doi.org/10.1016/j.ndteint.2004.06.012).
- [65] C. Negulescu et al. “Comparison of seismometer and radar measurements for the modal identification of civil engineering structures”. In: *Engineering Structures* 51 (June 2013), pp. 10–22. DOI: [10.1016/j.engstruct.2013.01.005](https://doi.org/10.1016/j.engstruct.2013.01.005).
- [66] F. Neitzel et al. “Investigation of Low-Cost Accelerometer, Terrestrial Laser Scanner and Ground-Based Radar Interferometer for Vibration Monitoring of Bridges”. In: *Proceedings of the 6th European Workshop on Structural Health Monitoring 2012*. Vol. 1. 2012, pp. 542–551.

- [67] Y. Q. Ni et al. “Correlating modal properties with temperature using long-term monitoring data and support vector machine technique”. In: *Engineering Structures* 27.12 (Oct. 2005), pp. 1762–1773. DOI: [10.1016/j.engstruct.2005.02.020](https://doi.org/10.1016/j.engstruct.2005.02.020).
- [68] G. Nico et al. “Dynamic Modal Identification of Telecommunication Towers Using Ground Based Radar Interferometry”. In: *Remote Sensing* 12.7 (2020). DOI: [doi : 10 . 3390 / rs12071211](https://doi.org/10.3390/rs12071211).
- [69] W. Niemeier. *Ausgleichsrechnung*. Vol. 2. Walter de Gruyter, Mar. 2008. DOI: [10 . 1515/9783110206784](https://doi.org/10.1515/9783110206784).
- [70] L. Noferini et al. “Permanent Scatterers Analysis for Atmospheric Correction in Ground-Based SAR Interferometry”. In: *IEEE Transactions on Geoscience and Remote Sensing* 43.7 (July 2005), pp. 1459–1471. DOI: [10.1109/tgrs.2005.848707](https://doi.org/10.1109/tgrs.2005.848707).
- [71] P. Olaszek, A. Świercz and F. Boscagli. “The Integration of Two Interferometric Radars for Measuring Dynamic Displacement of Bridges”. In: *Remote Sensing* 13.18 (Sept. 2021), p. 3668. DOI: [10.3390/rs13183668](https://doi.org/10.3390/rs13183668).
- [72] T. Owerko et al. “Investigation of displacements of road bridges under test loads using radar interferometry – Case study”. In: *Bridge Maintenance, Safety, Management, Resilience and Sustainability*. CRC Press, June 2012, pp. 181–188. DOI: [10.1201/b12352-19](https://doi.org/10.1201/b12352-19).
- [73] E. Parloo. “Application of Frequency-Domain System Identification Techniques in the Field of Operational Modal Analysis”. PhD thesis. Vrije Universiteit Brussel, 2003.
- [74] B. Peeters and G. D. Roeck. “One-year monitoring of the Z24-Bridge: environmental effects versus damage events”. In: *Earthquake Engineering & Structural Dynamics* 30.2 (2001), pp. 149–171. DOI: [10.1002/1096-9845\(200102\)30:2<149::aid-eqe1>3.0.co;2-z](https://doi.org/10.1002/1096-9845(200102)30:2<149::aid-eqe1>3.0.co;2-z).
- [75] M. Pieraccini et al. “Structural static testing by interferometric synthetic radar”. In: *NDT & E International* 33 (2000), pp. 565–570.
- [76] M. Pieraccini and L. Miccinesi. “Ground-Based Radar Interferometry: A Bibliographic Review”. In: *Remote Sensing* 11.9 (Apr. 2019), p. 1029. DOI: [10.3390/rs11091029](https://doi.org/10.3390/rs11091029).
- [77] M. Pieraccini et al. “In-service testing of wind turbine towers using a microwave sensor”. In: *Renewable Energy* 33.1 (Jan. 2008), pp. 13–21. DOI: [10.1016/j.renene.2007.02.001](https://doi.org/10.1016/j.renene.2007.02.001).
- [78] M. Pieraccini et al. “Static and dynamic testing of bridges through microwave interferometry”. In: *NDT & E International* 40.3 (Apr. 2007), pp. 208–214. DOI: [10.1016/j.ndteint.2006.10.007](https://doi.org/10.1016/j.ndteint.2006.10.007).
- [79] F. Pratesi et al. “Early Warning GBInSAR-Based Method for Monitoring Volterra (Tuscany, Italy) City Walls”. In: *IEEE Journal of Selected Topics in Applied Earth Observations and Remote Sensing* 8.4 (Apr. 2015), pp. 1753–1762. DOI: [10.1109/jstars.2015.2402290](https://doi.org/10.1109/jstars.2015.2402290).
- [80] Y. Qi et al. “Application of Microwave Imaging in Regional Deformation Monitoring Using Ground Based SAR”. In: *IEEE 5th Asia-Pacific Conference on Synthetic Aperture Radar (APSAR)*. IEEE, Sept. 2015. DOI: [10.1109/APSAR.2015.7306309](https://doi.org/10.1109/APSAR.2015.7306309).

- [81] C. Rainieri and G. Fabbrocino. *Operational Modal Analysis of Civil Engineering Structures*. Springer New York, 2014. DOI: [10.1007/978-1-4939-0767-0](https://doi.org/10.1007/978-1-4939-0767-0).
- [82] M. Rashidi et al. “A Decade of Modern Bridge Monitoring Using Terrestrial Laser Scanning: Review and Future Directions”. In: *Remote Sensing* 12.22 (Nov. 2020), p. 3796. DOI: [10.3390/rs12223796](https://doi.org/10.3390/rs12223796).
- [83] Richtlinie 804.800x. *Eisenbahnbrücken (und sonstige Ingenieurbauwerke) planen, bauen und instand halten*. Standard. DB Netz AG.
- [84] S. Rödelsperger. “Real-time Processing of Ground Based Synthetic Aperture Radar (GB-SAR) Measurements”. PhD thesis. Darmstadt: TU Darmstadt, 2011. URL: <http://tuprints.ulb.tu-darmstadt.de/2755/>.
- [85] S. Rödelsperger and A. Meta. “MetaSensing’s FastGBSAR: ground based radar for deformation monitoring”. In: *SPIE Proceedings*. SPIE Remote Sensing. Amsterdam, The Netherlands, Oct. 2014. DOI: [10.1117/12.2067243](https://doi.org/10.1117/12.2067243).
- [86] S. Rödelsperger et al. “Monitoring of displacements with ground-based microwave interferometry: IBIS-S and IBIS-L”. In: *Journal of Applied Geodesy* 4.1 (Jan. 2010). DOI: [10.1515/jag.2010.005](https://doi.org/10.1515/jag.2010.005).
- [87] F. Schill and A. Eichhorn. “Deformation Monitoring of Railway Bridges with a Profile Laser Scanner”. In: *zfv – Zeitschrift für Geodäsie, Geoinformation und Landmanagement* 144 (2019), pp. 109–118. DOI: [10.12902/zfv-0248-2018](https://doi.org/10.12902/zfv-0248-2018).
- [88] J. Schneider et al. “Identifikation dynamischer Strukturparameter von Eisenbahnbrücken mittels terrestrischer Mikrowelleninterferometrie”. In: *Schriftenreihe Konstruktiver Ingenieurbau Dresden*. Vol. 40. Technische Universität Dresden, Fakultät Bauingenieurwesen, 2015.
- [89] J. Severin et al. “Development and application of a pseudo-3D pit slope displacement map derived from ground-based radar”. In: *Engineering Geology* 181 (2014), pp. 202–211. DOI: [10.1016/j.enggeo.2014.07.016](https://doi.org/10.1016/j.enggeo.2014.07.016).
- [90] E. Smith and S. Weintraub. “The Constants in the Equation for Atmospheric Refractive Index at Radio Frequencies”. In: *Journal of Research of the National Bureau of Standards* 50.1 (Jan. 1953), p. 39. DOI: [10.6028/jres.050.006](https://doi.org/10.6028/jres.050.006).
- [91] M. Sofi et al. “Assessment of a Pedestrian Bridge Dynamics Using Interferometric Radar System IBIS-FS”. In: *Procedia Engineering* 188 (2017), pp. 33–40. DOI: [10.1016/j.proeng.2017.04.454](https://doi.org/10.1016/j.proeng.2017.04.454).
- [92] H. Sohn. “Effects of environmental and operational variability on structural health monitoring”. In: *Philosophical Transactions of the Royal Society A: Mathematical, Physical and Engineering Sciences* 365.1851 (Dec. 2006), pp. 539–560. DOI: [10.1098/rsta.2006.1935](https://doi.org/10.1098/rsta.2006.1935).
- [93] D. Su et al. “An interferometric radar for displacement measurement and its application in civil engineering structures”. In: *SPIE Proceedings*. Ed. by M. Tomizuka, C.-B. Yun and J. P. Lynch. SPIE, Apr. 2012. DOI: [10.1117/12.917292](https://doi.org/10.1117/12.917292).
- [94] M. Talich et al. “Experimental determining of horizontal movements of the water tower reservoirs by GB-RAR”. In: *IOP Conference Series: Earth and Environmental Science* 906.1 (Nov. 2021). DOI: [10.1088/1755-1315/906/1/012063](https://doi.org/10.1088/1755-1315/906/1/012063).

- [95] J. Wang et al. “Bridge Dynamic Cable-Tension Estimation with Interferometric Radar and APES-Based Time-Frequency Analysis”. In: *Electronics* 10.4 (Feb. 2021), p. 501. DOI: [10.3390/electronics10040501](https://doi.org/10.3390/electronics10040501).
- [96] S. Wang et al. “A Monostatic/Bistatic Ground-Based Synthetic Aperture Radar System for Target Imaging and 2-D Displacement Estimation”. In: *IEEE Geoscience and Remote Sensing Letters* (2020). DOI: [10.1109/LGRS.2020.2971662](https://doi.org/10.1109/LGRS.2020.2971662).
- [97] C. Werner et al. “The GPRI multi-mode Differential Interferometric Radar for Ground-based Observations”. In: *EUSAR 2012; 9th European Conference on Synthetic Aperture Radar*. 2012.
- [98] C. Xing et al. “Research on the Testing Methods for IBIS-S System”. In: *IOP Conference Series: Earth and Environmental Science* 17 (Mar. 2014). DOI: [10.1088/1755-1315/17/1/012263](https://doi.org/10.1088/1755-1315/17/1/012263).
- [99] Y. Xiong et al. “An Effective Accuracy Evaluation Method for LFM CW Radar Displacement Monitoring With Phasor Statistical Analysis”. In: *IEEE Sensors Journal* 19.24 (Dec. 2019). DOI: [10.1109/jsen.2019.2938620](https://doi.org/10.1109/jsen.2019.2938620).
- [100] D. Yunkai et al. “Constrained geometry analysis to resolve 3-D deformations from three ground-based radars”. In: *Journal of Systems Engineering and Electronics* 32.6 (Dec. 2021), pp. 1263–1269. DOI: [10.23919/jsee.2021.000107](https://doi.org/10.23919/jsee.2021.000107).
- [101] B. Zhang et al. “Dynamic displacement monitoring of long-span bridges with a microwave radar interferometer”. In: *ISPRS Journal of Photogrammetry and Remote Sensing* 138 (Apr. 2018), pp. 252–264. DOI: [10.1016/j.isprsjprs.2018.02.020](https://doi.org/10.1016/j.isprsjprs.2018.02.020).
- [102] M. Zhang et al. “Retrieving the True 3D Displacement of the Scene Based on Multiple Ground-based Microdeformation Monitoring Radars”. In: *2021 Photonics & Electromagnetics Research Symposium (PIERS)*. IEEE, Nov. 2021. DOI: [10.1109/PIERS53385.2021.9694791](https://doi.org/10.1109/PIERS53385.2021.9694791).
- [103] Q. W. Zhang, L. C. Fan and W. C. Yuan. “Traffic-induced variability in dynamic properties of cable-stayed bridge”. In: *Earthquake Engineering & Structural Dynamics* 31.11 (2002), pp. 2015–2021. DOI: [10.1002/eqe.204](https://doi.org/10.1002/eqe.204).
- [104] Z. Zhao et al. “An Improved Vibration Parameter Estimation Method Applied for GB-MIMO Radar”. In: *IEEE Geoscience and Remote Sensing Letters* 19 (2022), pp. 1–5. DOI: [10.1109/LGRS.2022.3192915](https://doi.org/10.1109/LGRS.2022.3192915).
- [105] Z. Zhao et al. “Dynamic Deformation Measurement of Bridge Structure Based on GB-MIMO Radar”. In: *IEEE Transactions on Geoscience and Remote Sensing* 60 (2022), pp. 1–14. DOI: [10.1109/tgrs.2022.3197227](https://doi.org/10.1109/tgrs.2022.3197227).
- [106] K. Zschiesche. “Image Assisted Total Stations for Structural Health Monitoring—A Review”. In: *Geomatics* 2.1 (Dec. 2021), pp. 1–16. DOI: [10.3390/geomatics2010001](https://doi.org/10.3390/geomatics2010001).

List of Figures

1.1	Structure of this thesis.	5
2.1	Linear frequency modulation of FMCW systems with transmitted and received signals.	8
2.2	Amplitude spectrum of different window functions.	9
2.3	Measurement principle of GBR for bridge monitoring.	10
2.4	Phasor plots for two consecutive sample points consisting of a dominant reflection and noise.	11
2.5	Overview of the investigated bridges.	23
3.1	GBR processing with the conventional and additional steps.	27
3.2	Simulation of the influence of static clutter. Adapted from [60].	30
3.3	Schema for the transformation of displacements in LOS to a Cartesian coordinate system. Adapted from [60].	35
3.4	Measurement setup at the road bridge in Schneckenlohe.	40
3.5	Measurement setup with the field of view for two GBR and two TLS at the railway bridge over the river Rhine at Maxau.	40
3.6	Detection of phase jumps in the raw displacements measured by GBR 1 at Target 1 in Schneckenlohe. Reprinted from [60].	42
3.7	Detection of broadband noise for a segment of the raw displacements measured by GBR 1 at Target 1 in Schneckenlohe.	42
3.8	Clutter removal in Schneckenlohe.	43
3.9	Relationship between displacement and amplitude, and their impact on clutter estimation at Maxau.	44
3.10	Ratio of the circle centre's distance to its radius at Maxau.	45
3.11	Ratio of the circle centre's distance difference between window functions to its radius at Maxau.	46
3.12	Atmospheric correction of the displacements measured by GBR 1 at Target 1 in Schneckenlohe.	47
3.13	Segment of the projected displacements for both targets in Schneckenlohe.	48
3.14	Projected displacements during the first train crossing at Maxau.	50
3.15	Difference of the displacement measured by GBR to the displacement measured by TLS during the first train crossing at Maxau.	50

3.16	Projected displacements during the second train crossing at Maxau.	51
3.17	Displacements in LOS projected with TLS measurements during the second train crossing at Maxau.	51
3.18	Simulated uncertainty for displacements as a function of the bridge's x-coordinate at Maxau.	53
4.1	Overview of the approach for natural frequency estimation.	62
4.2	Example of vehicle crossings in the time and frequency domain in Seßlach. Adapted from [61].	63
4.3	Measurement setup at the bridge in Seßlach.	68
4.4	Measurement setup at the bridge in Schneckenlohe.	68
4.5	Natural frequencies as a function of temperature estimated by FDD in Seßlach.	70
4.6	Natural frequencies as a function of temperature estimated by FDD in Schneckenlohe.	70
4.7	Natural frequencies as a function of temperature estimated by least squares in Seßlach. Adapted from [61].	71
4.8	Variation of the linear regression depending on sample size in Seßlach.	73
4.9	Variation of the linear regression for the measurement days of 23 and 24 October 2019 in Seßlach.	74
4.10	Variation of the linear regression for the measurement days of 27 February and 29 July 2020 in Seßlach.	74
5.1	Measurement principle of the mirror mode.	83
5.2	Measurement setup at the Pulverhausstraße on 18 June 2019.	85
5.3	Vertical displacement measured by two GBRs and the TLS.	86
5.4	Vertical displacements of reference sensors subtracted by vertical displacement of the GBR in mirror mode.	87
5.5	Measurement setups at the Pulverhausstraße on 18 August 2022.	89
5.6	Mode shape from mirror mode measurements.	92
5.7	Mode shape from one-dimensional measurements.	92

List of Tables

2.1	Existing research for comparison and validation of GBR with other sensor technology.	17
2.2	Existing research for feature estimation from GBR measurements.	19
2.3	Overview of the investigated bridges and their properties.	20
3.1	Accuracy of the disturbance detection in Schneckenlohe. Adapted from [60]	43
3.2	Measurement uncertainty after each processing steps in Schneckenlohe. Reprinted from [60].	53
4.1	Measurement campaigns with durations and temperature ranges.	67
4.2	Results of the linear regression for the temperature-frequency relationship estimated by FDD in Seßlach.	69
4.3	Results of the linear regression for the temperature-frequency relationship estimated by least squares in Seßlach. Reprinted from [61].	72
4.4	Comparison of vehicle types with least squares in Seßlach.	75
5.1	Specifications of the sensors applied at the Pulverhausstraße on 18 June 2019.	85

List of Symbols

A	Amplitude of the received signal
a	Amplitude of a sinusoid
α	Significance level
A_n	Noise of the received signal
B	Bandwidth of the signal modulation
c	Speed of light
Δd	Displacements in LOS
d	Distance between GBR and target
δ_d	Range resolution
Δd_v	One-dimensional displacements in the vertical axis
ε	Residuals
f	Frequency of a sinusoid
f_B	Beat frequency between transmitted and received signal
γ	Test statistic
h	Height to the bridge relative to the sensor
J	Jacobi-matrix
Λ	Decay rate of a damped sinusoid
λ	Central wavelength of the GBR signal
m_A	Mean of the amplitude
Δn	Change of the atmospheric refractive index
n	Number of observations
ν	Degree of freedom
Ω	Mode shape
$\Delta \mathbf{P}$	Three-dimensional displacement vector
\mathbf{P}	New target coordinates
\mathbf{P}^0	Initial target coordinates
φ	Central angle of a circular arc
ϕ_{atmo}	Atmospheric part of the phase measurement
ϕ_{uw}	Unwrapped phase of the received signal
ϕ_w	Wrapped phase of the received signal
R	Radius of a circular arc

r	Radii of the data points
R^2	Coefficient of determination
ρ	Factor for mode shape scaling
s	Standard deviation of a distribution
σ_A	Standard deviation of the amplitude
$\sigma_{\Delta d}$	Standard deviation of the displacements in LOS
s_{est}	Standard error of the estimate
$\Sigma_{\Delta d}$	Variance matrix of the displacements in LOS
$\Sigma_{\Delta P}$	Variance matrix of the projected displacements
σ_{coord}	Variance of the coordinates
$\hat{\sigma}_0^2$	A-posteriori variance factor
$\sigma_{\Delta\phi}$	Standard deviation of the phase
T	Sweep time
t	Time
τ	Signal delay between transmitted and received signal
θ	Phase of a sinusoid
W	Weight matrix containing the measurement uncertainties
x_m	Origin of a circular arc (x-coordinate)
y_m	Origin of a circular arc (y-coordinate)
ζ	Damping ratio of a damped sinusoid

List of Abbreviations

DFT	discrete Fourier transform
FastGBSAR	Fast Ground-Based Synthetic Aperture Radar
FDD	frequency domain decomposition
FEM	finite element method
FMCW	frequency-modulated continuous-wave
GBR	ground-based interferometric radar
GBSAR	ground-based synthetic aperture radar
GNSS	global navigation satellite system
IBIS	Image by Interferometric Survey
IDFT	inverse discrete Fourier transform
IQ	in-phase and quadrature
LOS	line of sight
LS	least squares
MIMO	multiple-input multiple-output
OMA	operational modal analysis
PoGER	Post Global Estimation Re-Scaling
PoSER	Post Separate Estimation Re-Scaling
PreGER	Pre Global Estimation Re-Scaling
PSD	power spectral density
SDOF	single degree of freedom
SFCW	stepped-frequency continuous-wave
SNR	signal-to-noise ratio
SSI	stochastic subspace identification
SVD	singular value decomposition
TLS	terrestrial laser scanner

Colophon

This thesis was typeset with \LaTeX . It uses an adaptation of the *Clean Thesis* style developed by Ricardo Langner.